

©2016 – SAHAB BABAEE
ALL RIGHTS RESERVED.

Non-linear Mechanics of Three-dimensional Architected Materials; Design of Soft and Functional Systems and Structures

ABSTRACT

In the search for materials with new properties, there have been significant advances in recent years aimed at the construction of architected materials whose behavior is governed by structure, rather than composition. Through careful design of the material's architecture, new mechanical properties have been demonstrated, including negative Poisson's ratio, high stiffness to weight ratio and mechanical cloaking. However, most of the proposed architected materials (also known as mechanical metamaterials) have a unique structure that cannot be reconfigured after fabrication, making them suitable only for a specific task.

This dissertation focuses on the design of architected materials that take advantage of the applied large deformation to enhance their functionality. Mechanical instabilities, which have been traditionally viewed as a failure mode with research focusing on how to avoid them, are exploited to achieve novel and tunable functionalities. In particular I demonstrate the design of mechanical metamaterials with tunable negative Poisson ratio, adaptive phononic band gaps, acoustic switches, and reconfigurable origami-inspired waveguides.

Remarkably, due to large deformation capability and full reversibility of soft materials, the responses of the proposed designs are reversible, repeatable, and scale-independent. The results presented here pave the way for the design of a new class of soft, active, adaptive, programmable and tunable structures and systems with unprecedented performance and improved functionalities.

Contents

1	INTRODUCTION	1
2	THREE-DIMENSIONAL SOFT METAMATERIALS WITH NEGATIVE POISSON'S RATIO	7
2.1	Overview	8
2.2	Introduction	8
2.3	Results and Discussion	10
2.4	Conclusions	21
2.5	Materials and Methods	22
3	THREE-DIMENSIONAL ADAPTIVE SOFT PHONONIC CRYSTALS	24
3.1	Overview	25
3.2	Introduction	25
3.3	3D Phononic Crystal	27
3.4	General Formulation	29
3.5	Numerical Procedure and Implementation	32
3.6	Results	40
3.7	Conclusions	48
4	HARNESSING DEFORMATION TO SWITCH ON AND OFF THE PROPAGATION OF SOUND	50
4.1	Overview	51
4.2	Introduction	51
4.3	Results and Discussion	52
4.4	Summary	63
5	RECONFIGURABLE ORIGAMI-INSPIRED ACOUSTIC WAVEGUIDES	64
5.1	Overview	65
5.2	Introduction	65

5.3	Results	66
5.4	Discussion	79
5.5	Methods	81
APPENDIX A SUPPORTING INFORMATION TO CHAPTER 2		82
A.1	Building Blocks	83
A.2	Representative Volume Elements	83
A.3	Experiments	83
A.4	Numerical Simulations of Stability Analysis for 3D Periodic Structures	85
A.5	Stability Analysis for 6-Hole Bucklicrystal	87
A.6	Stability Analysis for All Bucklicrystals	89
A.7	Porosity of Bucklicrystals	93
APPENDIX B SUPPORTING INFORMATION TO CHAPTER 5		95
B.1	Fabrication	96
B.2	Testing	97
B.3	Analytical Model for Deformation of a Helix	99
B.4	Numerical Simulations	101
B.5	Additional Results	108
APPENDIX C SUPPORTING INFORMATION TO CHAPTER 6		112
C.1	Reconfigurable Metamaterial Based on Extruded Cubes	113
C.2	Reconfigurable Metamaterial Based on Extruded Truncated Octahedra	114
C.3	Reconfigurable Metamaterial Based on Extruded Hexagonal Prisms . .	118
REFERENCES		136

List of Figures

1.1	Architected structures ranging from nanometer o kilometer scale. (a) Heat management by thermocrystal ⁸² (b) ultralight metallic microlattice ¹²¹ (c) 3D broadband omnidirectional acoustic cloak ¹⁶⁵ (d) locally resonant sonic materials ⁷⁷ (e) sound attenuation by sculpture ⁸⁹ , and (f) Buitenschot noise-canceling landscape art park ¹	3
2.1	Gallery of Bucklicrystals. a) Building blocks with 6, 12 and 24 holes. For the sake of simplicity, we always color the building blocks with 6, 12 and 24 holes with red, green and blue, respectively. Moreover, we also identify the junctions where the building blocks are attached to the surrounding units using yellow circles, black triangles, and magenta squares for <i>bcc</i> , <i>fcc</i> , and <i>sc</i> packing configurations, respectively. b) Representative volume elements (RVE) for the Bucklicrystal in the undeformed configuration. c) Buckled configurations for the RVEs under uniaxial compression. . . .	11
2.2	Experimental (micro-CT) and numerical images of the 6-hole Bucklicrystal. a) Isometric and cross-sectional views of the undeformed crystal from micro-CT X-ray imaging machine. b) Isometric and cross-sectional views of the uniaxially compressed crystal ($\epsilon_{22}^{\text{applied}} = -0.20$) from micro-CT volumetric data sets. In the cross sectional views, the inner-most RVE is highlighted by a red box. $\Delta x_i(0)$ and Δx_i , $i = 1, 2, 3$, are the edge length of the red box in the i direction for undeformed and buckled crystals, respectively. c) Magnified views of the inner-most RVE taken from micro-CT X-ray scanning at different levels of strains. d) Corresponding pictures taken from simulation. (Green scale bars: 20 mm)	14

2.3	Evolution of transverse strains and Poisson's ratios for the 6-hole Bucklicrystal. a) Evolution of the transverse engineering strain ϵ_{11} and ϵ_{33} as a function of the applied longitudinal strain ϵ_{22} . b) Evolution of the Poisson's ratios (ν_{21} and ν_{23}) of the 6-hole Bucklicrystal as a function of compressive strain ϵ_{22} . The finite element results (solid lines) are in good agreement with the experimental data (square markers).	16
2.4	Mechanical response of Bucklicrystals. a) Nominal stress-strain curves from uniaxial compression in 2-direction for all of the Bucklicrystals. The stress is normalized with respect to the elastic modulus of the bulk elastomeric material. b) Evolution of the Poisson's ratios vs. nominal strain in 2- direction for all the Bucklicrystals. c) Cross sectional views of undeformed ($\epsilon_{22} = 0$) and deformed ($\epsilon_{22} = -0.15$) configurations of 12- and 24-hole Bucklicrystals.	19
3.1	Tunable 3D phononic crystal composed of a periodic array of structured shells arranged to form a body centered cubic (<i>bcc</i>) lattice. When compressed, this structure undergoes an instability, which results in folding of all the building blocks. Each structured shell is fully characterized by two design parameters: the angle α that defines the narrowest width of the ligament, and the ratio $\tau = w_i/t$ between the inner narrowest width of the ligaments and the radial shell thickness.	26
3.2	Schematic of point lattice (green dots in (a)), reciprocal lattice (black dots in (b)), first Brillouin zone (grey cube in (b)) and irreducible Brillouin zone (red pyramid GXMR in (b)). Three different views of the reciprocal lattice are shown at the bottom.	35
3.3	First Brillouin zone (cube of side $2\pi/a$) and irreducible Brillouin zone (IBZ) with the seven high-symmetry points used in this study: corner points (G, X, M, R) and points on mid-diagonal lines (GR, XR, MG).	36
3.4	Band diagrams for a 3D phononic crystal characterized by $(\alpha, \tau) = (0.03, 0.2)$ calculated using full (direct) method (left) and the RBME method (right).	38

3.5	Effect of design parameters α and τ on the band structures. In the dispersion relation plots, the non-dimensional frequency $\bar{f} = \omega a / 2\pi c_T$ is plotted versus the wave vectors \mathbf{k} . Three different configurations are considered characterized by $(\alpha, \tau) = (0.14, 0.2)$ (center), $(0.14, 1.0)$ (left) and $(0.03, 0.2)$ (right). The shaded red region in the right plot highlights the bandgap - i.e. ranges of frequencies for which the elastic waves are not allowed to propagate along any direction.	40
3.6	Bands diagram for a phononic crystal composed of a <i>bcc</i> array of structured shells attached to the neighbors through the ligaments. The structured shells are characterized by $(\alpha, \tau) = (0.03, 0.2)$. Note that these are the same design parameters that we used to construct the phononic crystal shown in Figure 3.5-right. $\tilde{a} = 4r_o/\sqrt{2}$ is the characteristic length of the unit cell.	42
3.7	Design of an optimal 3D phononic crystal in the undeformed configuration. (a) Evolution of the bandgap as a function of τ for a 3D crystal with $\alpha = 0.03$. The structure exhibits the widest phononic bandgap for $\tau = 0.4$ and is demonstrated in (b). (c) Bands diagram for the optimal crystal characterized by $(\alpha, \tau) = (0.03, 0.4)$. The 3D structure exhibits a wide bandgap at $\bar{f} = 0.43 - 0.72$	43
3.8	Evolution of bandgap as a function of the applied compressive strain for a 3D crystal characterized by $(\alpha, \tau) = (0.03, 0.4)$. Note that buckling occurs at $\epsilon = -0.007$	44
3.9	Effect of damping on the transmission spectra for models consist of (a) 4, (b) 10, (c) 20, and (d) 40 unit cells along the x-direction and periodic boundary conditions on the lateral faces. The solid horizontal red lines represent the bandgap predictions for the corresponding undamped infinite periodic structures. The horizontal dashed red lines highlight regions with a relative -15 dB drop in transmission. Note that for $\bar{q} = 0.005$ and 0.02, the transmission decays above a cut-off frequency.	46
3.10	Effect of damping on the propagation of elastic waves in a finite size structure consists of $4 \times 4 \times 4$ structured shells. The solid horizontal lines indicate the bandgaps prediction based on calculations for the infinite undamped structure, while the dashed horizontal lines highlight regions in which a relative -15 dB drop is observed in the transmission.	48

4.1	Acoustic switch. The fabricated acoustic switch comprises a 6×6 square array of stretchable helices. In the undeformed configuration (i.e. $\epsilon = 0.0$), the helices are in a compact state and can be regarded as solid cylinders of height $H_0 = 40 \text{ mm}$. As a result, the metamaterial is characterized by a frequency range of strong wave attenuation (bandgap). As the helices are stretched, the solid volume fraction of the metamaterial drops significantly and the bandgap is suppressed.	53
4.2	Deformation of the helices. (a) Experimental (green samples) and numerical (blue models) images of a single helix at different levels of applied strain, $\epsilon = 0, 0.40, 0.65$, and 0.90 . P_0 and D_0 are the pitch length and outer diameter of the helix at $\epsilon = 0$. (b-d) Evolution of (b) pitch length, P , (c) outer diameter, D , and (d) solid volume fraction, ψ , as a function of the applied strain. Analytical predictions (red dashed line) are compared to both experimental (green markers) and numerical (blue markers) results.	56
4.3	Propagation of sound through the metamaterial at different levels of applied deformation. (a,b) Dispersion relations, and (c,d) experimentally measured transmission spectra for acoustic waves propagating along the GX direction. Results are shown for (a,c) the undeformed configuration ($\epsilon = 0$), and (b,d) the stretched configuration ($\epsilon = 0.9$).	60
4.4	Effect of arrangement of the helices and their geometry. (a) Evolution of the bandgap frequency, f , as a function of the applied strain, ϵ , for a triangular array (with lattice spacing $A_0 = 32.5 \text{ mm}$) of the helices with initial outer diameter $D_0 = 28.6 \text{ mm}$, pitch $P_0 = 13 \text{ mm}$, and rectangular cross-section of $13 \times 6.5 \text{ mm}$. (b) Evolution of the bandgap frequency, f , as a function of the applied strain, ϵ , for a square array (with lattice spacing $A_0 = 50 \text{ mm}$) of the helices with initial outer diameter $D_0 = 48 \text{ mm}$, pitch $P_0 = 24 \text{ mm}$, and rectangular cross-section of $24 \times 2 \text{ mm}$. The insets show the evolution of the solid volume fraction as function of the applied strain.	62

5.1	Reconfigurable origami-inspired acoustic waveguides. Experimental and numerical images of the the building block (the extruded cube) and the corresponding reconfigurable acoustic metamaterial deformed into three different configurations: (A) $(\alpha_1, \alpha_2, \alpha_3) = (\pi/2, \pi/2, \pi/2)$; (B) $(\alpha_1, \alpha_2, \alpha_3) = (\pi/2, \pi/2, 0)$; (C) $(\alpha_1, \alpha_2, \alpha_3) = (\pi/3, 2\pi/3, \pi/3)$. The red arrows and shaded areas indicate the excited waves, while the green arrows and shaded areas highlight the points from which the structure radiates.	68
5.2	Experimental setup. Experimental setup without the sound absorbing foams surrounding the sample.	70
5.3	Propagation of sound waves for $(\alpha_1, \alpha_2, \alpha_3) = (\pi/2, \pi/2, 0)$. (A) Numerical image of the metamaterial. (B) Top cross-sectional view of the pressure field distribution at $f = 3.5kHz$. The cutting plate is shown in (A) and the color indicates the pressure amplitude normalized by the input signal amplitude (p_0) (C) Frequency-dependent transmittance for the sample. Both experimental (red lines), numerical (blue line) and analytical (dashed black lines) results are shown.	72
5.4	Propagation of sound waves for $(\alpha_1, \alpha_2, \alpha_3) = (\pi/3, 2\pi/3, \pi/3)$. (A) and (B) Frequency-dependent transmittances for the sample calculated considering two different detection points. Both experimental (red lines) and numerical (blue line) results are shown. (A) Numerical image of the metamaterial. (B) Top cross-sectional view of the pressure field distribution at $f = 2kHz$ and $f = 4.8kHz$. The cutting plate is shown in (A) and the color indicates the pressure amplitude normalized by the input signal amplitude (p_0)	74
5.5	Propagation of sound waves for $(\alpha_1, \alpha_2, \alpha_3) = (\pi/2, \pi/2, \pi/2)$. (A) and (B) Frequency-dependent transmittances for the sample calculated considering two different detection points. Both experimental (red lines) and numerical (blue line) results are shown. (A) Numerical image of the metamaterial. (B) Top cross-sectional view of the pressure field distribution at $f = 2kHz$ and $f = 4.8kHz$. The cutting plate is shown in (A) and the color indicates the pressure amplitude normalized by the input signal amplitude (p_0)	75

5.6	Reconfigurable acoustic waveguide based on a tessellation of truncated octahedra. Experimental and numerical images of the the building block (the extruded cube) and the corresponding reconfigurable acoustic metamaterial deformed into three different configurations: (A) $\theta = \pi/4$; (B) $\theta = 0$; (C) $\theta = \pi/2$	77
5.7	Reconfigurable acoustic waveguide based on a tessellation of hexagonal prisms. Experimental and numerical images of the the building block (the extruded cube) and the corresponding reconfigurable acoustic metamaterial deformed into four different configurations: (A) $(\alpha, \gamma) = (0, 0)$; (B) $(\alpha, \gamma) = (\pi/4, -\pi/4)$; (C) $(\alpha, \gamma) = (-\pi/4, -\pi/4)$; (D) $(\alpha, \gamma) = (\pi/4, \pi/4)$	79
A.1	Different views of the building blocks with 6, 12, and 24 holes.	84
A.2	Different views of the undeformed RVEs for all the proposed Bucklicrystals.	85
A.3	Testing of the Bucklicrystal. a,b) Undeformed configuration. c,d) Deformed configuration at $\epsilon_{22}^{applied} = -0.3$. (scale bar: 60mm)	86
A.4	Left: RVE for the undeformed 6-hole <i>bcc</i> . Right: Critical mode detected by the Bloch wave analysis. Note that the deformation of the RVE is slightly different in 1 and 3 directions.	88
A.5	Critical modes for all the Bucklicrystals under uniaxial compression. Upon applying a load in the 2- direction, all the ligaments undergo the first buckling mode and all the circular holes close uniformly. Note that for <i>sc</i> configurations, buckling leads to an enlarged RVE, which is comprised of 8 building blocks (RVE size = $2 \times 2 \times 2$ in 1, 2, and 3 directions).	90
A.6	Sequence of progressively deformed configurations of the building blocks. The circular markers are used to highlight the rotation of the junctions used to build <i>bcc</i> Bucklicrystals. Yellow markers indicate a counterclockwise rotation, while black markers correspond to a clockwise rotation. In the 6-hole building block, half of the junctions rotate clockwise and half counterclockwise, as indicated by the yellow and black markers. In contrast, for the building block with 12 or 24 holes, all identical junctions rotate in the same direction.	91

A.7	Left: Enlarged RVE for the undeformed 12-hole <i>bcc</i> comprising of 35 building blocks. Right: Reconstruction of the critical mode detected for the enlarged RVE. Note that the folded building blocks have two different orientations, as indicated by the two colors (blue and green). As a result, each unit is oriented differently with respect to the surrounding connected units.	92
A.8	Left: Enlarged RVE for the undeformed 6-hole <i>bcc</i> comprising of 35 building blocks. Right: Reconstruction of the critical mode detected for the enlarged RVE. Note that all folded building blocks have exactly the same orientation.	92
B.1	Fabrication. (a) 3-D printed plastic mold, and (b) elastomeric helix manufactured using the mold and casting approach.	97
B.2	Testing. (a) Front-view image of the fabricated metamaterial at $\epsilon = 0$. (b) Position of loudspeakers in the experimental set-up. (c) Experimental set-up without the metamaterial used to measure the transmission through air.	98
B.3	Numerical images of a single helix. Front and isometric views of (a) the undeformed and (b) highly deformed (i.e., $\epsilon = 0.9$) configuration as obtained from the static analysis.	103
B.4	Bloch wave analysis. (a) Undeformed configuration ($\epsilon = 0$): oblique and top views of the unit cell as obtained from Step 1 (static analysis) and of that used for Step 2 (Bloch analysis); (b) Deformed configuration ($\epsilon = 0.9$): oblique and top views of the unit cell as obtained from Step 1 (static analysis) and of that used for Step 2 (Bloch analysis); (c) corresponding point lattice in reciprocal space showing the <i>first Brillouin zone</i> (the area inside the yellow square) and the <i>irreducible Brillouin zone</i> (red GXM triangle) for square arrangement of helices. \mathbf{b}_1 and \mathbf{b}_2 are the reciprocal lattice vectors.	105

B.5	Effect of the applied deformation on the dispersion relations for the fabricated structure. Dispersion relations calculated at different levels of applied deformation. At each level of deformation the dispersion plots on the left (in blue) are obtained from models that comprise both the elastomeric helix and the surrounding air, while the dispersion plots on the right (in grey) are obtained from simplified models in which the elastomeric helix is modeled as a cavity and perfectly-reflecting boundary conditions are assumed at the interface. The results are reported at different levels of strains (a) $\epsilon = 0$, (b) $\epsilon = 0.05$, (c) $\epsilon = 0.28$, (d) $\epsilon = 0.40$, (e) $\epsilon = 0.80$, and (f) $\epsilon = 0.92$ under uniaxial tension. The insets show the configuration of helices at the corresponding levels of applied strains. The metamaterial comprises a square array of helices with initial outer diameter $D_0 = 28.6 \text{ mm}$, pitch $P_0 = 13 \text{ mm}$, rectangular cross-section of $13 \times 6.5 \text{ mm}$, and lattice spacing $A_0 = 32.5 \text{ mm}$	108
B.6	Evolution of band gap frequency as a function of the applied deformation for the fabricated structure. The metamaterial comprises a square array of helices with initial outer diameter $D_0 = 28.6 \text{ mm}$, pitch $P_0 = 13 \text{ mm}$, rectangular cross-section of $13 \times 6.5 \text{ mm}$, and lattice spacing $A_0 = 32.5 \text{ mm}$	109
B.7	Effect of the applied deformation on the dispersion relations of a triangular array of helices. Dispersion relations calculated at different levels of applied deformation. The results are reported at different levels of strains (a) $\epsilon = 0$, (b) $\epsilon = 0.05$, (c) $\epsilon = 0.28$, (d) $\epsilon = 0.53$, (e) $\epsilon = 0.80$, and (f) $\epsilon = 1.30$ under uniaxial tension. The insets show the configuration of helices at the corresponding levels of applied strains. The metamaterial comprises a triangular array of helices with initial outer diameter $D_0 = 28.6 \text{ mm}$, pitch $P_0 = 13 \text{ mm}$, rectangular cross-section of $13 \times 6.5 \text{ mm}$, and lattice spacing $A_0 = 32.5 \text{ mm}$	110

B.8	Effect of the applied deformation on the dispersion relations of a square array of helices. Dispersion relations calculated at different levels of applied deformation. The results are reported at different levels of strains (a) $\epsilon = 0$, (b) $\epsilon = 0.05$, (c) $\epsilon = 0.25$, (d) $\epsilon = 0.45$, (e) $\epsilon = 1.1$, and (f) $\epsilon = 1.5$ under uniaxial tension. The insets show the configuration of helices at the corresponding levels of applied strains. The metamaterial comprises a square array of helices with initial outer diameter $D_0 = 48 \text{ mm}$, pitch $P_0 = 24 \text{ mm}$, rectangular cross-section of $24 \times 2 \text{ mm}$, and lattice spacing $A_0 = 50 \text{ mm}$	111
C.1	Propagation of sound waves for $(\alpha_1, \alpha_2, \alpha_3) = (\pi/2, \pi/2, 0)$. Top cross-sectional view of the pressure field distribution at $f = 3.5 \text{ kHz}$. The cutting plate is shown on the right and the color indicates the pressure amplitude normalized by the input signal amplitude (p_0). Differently from Figure 6.3B in the main text, the color bar is chosen to be $-1 < p/p_0 < 1$ so that the plane modes (i.e., high and low pressure zones) are more evident. Note that the weak radiation outside of the structure is not clearly visible for this choice of color bar.	113
C.2	Building block and central unit of the metamaterial based on extruded truncated octahedra.	115
C.3	Reconfigurable metamaterial based on a tessellation of truncated octahedra. Numerical images of the the building block and the corresponding $4 \times 4 \times 4$ reconfigurable acoustic metamaterial deformed into three different configurations: (A) $\theta = \pi/4$; (B) $\theta = 0$; (C) $\theta = \pi/2$	117
C.4	Building block and central unit of the extruded truncated octahedron metamaterial. The angels α and γ used to describe the shape of the geometry are demonstrated on the right which defined as angular deviation from vectors \mathbf{A} , \mathbf{C} (β is always assumed to be zero). In the buiding block on the left, the red arrows and shaded areas indicate the excited waves, while the green arrows and shaded areas highlight the points from which the structure radiates.	119

C.5	Reconfigurable metamaterial based on hexagonal prisms. Numerical images of the the building block and the corresponding $4 \times 4 \times 4$ reconfigurable acoustic metamaterial deformed into three different configurations:	
	(A) $(\alpha, \gamma) = (0, 0)$; (B) $(\alpha, \gamma) = (\pi/4, -\pi/4)$; (C) $(\alpha, \gamma) = (-\pi/4, -\pi/4)$;	
	(D) $(\alpha, \gamma) = (\pi/4, \pi/4)$	120

CITATIONS TO PREVIOUSLY PUBLISHED WORK

Chapters 2-5 are based on the following papers:

Chapter 2:

S. Babae, J. Shim, J. C. Weaver, N. Patel, and K. Bertoldi, 3D Soft Metamaterials with Negative Poissons Ratio, **Advanced Materials** 2013, 25 (36):5044-5049.

Chapter 3:

S. Babae, P. Wang, and K. Bertoldi, Three-dimensional Adaptive Soft Phononic Crystals, **Journal of Applied Physics** 2015, 117 (24):244903.

Chapter 4:

S. Babae, N. Viard, N. Fang, and K. Bertoldi, Harnessing Deformation to Switch On and Off the Propagation of Sound, **Advanced Materials** 2016, 28 (8):1631-1635.

Chapter 5:

S. Babae, J. B. Overveldeh, E. R. Chen, V. Tournat, and K. Bertoldi, Reconfigurable Origami-inspired Acoustic Waveguides, Submitted.

Citations to other work authored during the course of the degree, not included in this thesis:

Y. Zarate, **S. Babae**, S. H. Kang, K. Bertoldi, I. V. Shadrivov, D. N. Neshev, D. A. Powell, and Y. S. Kivshar, Elastic Metamaterials for Tuning Circular Polarization of Electromagnetic Waves, **Scientific Reports** 2016, 6 :28273.

S. Babae, A. Shahsavari, P. Wang, R. C. Picu, and K. Bertoldi, Wave Propagation in Cross-Linked Random Fiber Networks, **Applied Physics Letter** 2015, 107 (21):211904.

W. J. Duncanson, T. E. Kodger, **S. Babae**, G. Gonzalez, D. A. Weitz, and K.

Bertoldi, Microfluidic Fabrication and Micromechanics of Permeable and Impermeable Elastomeric Microbubbles, **Langmuir** 2015, 31 (11):3489-3493.

D. Mousanezhad, **S. Babaee**, R. Ghosh, E. Mahdi, K. Bertoldi, and A. Vaziri, Honeycomb Phononic Crystals with Self-Similar Hierarchy, **Physical Review B** 2015, 92 (10):104304.

D. Mousanezhad*, **S. Babaee***, H. Ebrahimi*, R. Ghosh, E. Mahdi, K. Bertoldi, and A. Vaziri, Hierarchical Honeycomb Auxetic Metamaterials, **Scientific Reports** 2015, 5:18306. * denotes co-first authorship

TO FAMILY AND FRIENDS.

Acknowledgments

I am lucky to have had the opportunity to interact with so many amazing people during my PhD. It is a great pleasure to acknowledge those who have supported my doctoral studies at Harvard University.

I would like to thank my advisor Katia Bertoldi for instructing me in the simple and straightforward approach to mechanics and constant support. Her energy and creativity will always be an inspiration as I constantly ask myself: what would Katia do? I have had the amazing opportunity to interact with many people within the Harvard community who have taught me not only about science but also about life. I have learned so much from a number of other professors: John Hutchinson, Zhigang Suo, Joost Vlassak, David Clarke, and Jim Rice. Thank you all for taking the time to educate me and for putting up with my constant questions. I am especially grateful to professors Bertoldi, Vlassak, and Clarke for taking the time to be on my thesis committee and provide enormous amounts of support.

I would like to thank all the wonderful Bertoldi group members with whom I have interacted over the years. I am particularly grateful to Pai Wang, Jongmin Shim, Elizabeth R. Chen, Johannes T. B. Overvelde, Sung H. Kang, Fionnuala Connolly, Jia Liu, Sicong Shan, Michael Taylor, Filippo Casadei, Tianxiang Su, David Henann, Jordan R. Raney, Andrej Kosmrlj, Patrick Kurzeja, Farhad Javid, Kitty Kumar, Andrew Gross, Sara Norman, Sijie Sun, Shuai Bei, Nikita Patel, and many other equally deserving people whose names just are not coming to my mind now, for exciting collaborations and interesting discussions.

I have also benefited tremendously from fantastic collaborations and discussions with the collaborators from other universities: James Weaver at Wyss Institute for manufacturing specimens and great discussion regarding experiments, N. Viard and N. Fang for awesome collaboration on acoustic material testing at MIT, A. S. Shahsavari and R. C. Picu at Rensselaer Polytechnic Institute for wonderful collaboration on fiber network project, D. Mousanezhad and A. Vaziri at Northeastern University for excellent collaboration on hierarchical cellular structures, Y. Zarate and D. Powell

at Australian National University for collaboration on tuning circular polarization of electromagnetic waves, Wynter J. Duncanson and David A. Weitz at Harvard University for collaboration on microfluid fabrication on microbubbles, and Vincent Tournat at CNRS, Universit du Maine in Paris for great discussion on tunable acoustic waveguides.

I would also like to convey appreciation to the John A. Paulson School of Engineering and Applied Science at Harvard university, Wyss Institute for Biologically Inspired Engineering, the Materials Research Science and Engineering Center (MRSEC) at Harvard, and Harvards Kavli Institute for Bionano Science and Technology for financial support. Without this support, this thesis would not be possible.

Finally, I am really grateful to all of my parents, siblings and friends for enriching my life. I would particularly like to thank my father, Satar Babae, my mother, Ashraf Moravejiasl, my sister, Samaneh Babae, my brother Samrad Babae, and wonderful friends Mehdi Abedi and Hossein Sharifazadeh for unconditional love, support, and belief in me. They have encouraged me to pursue my dreams, whatever they may be. They have shown me how to be kind, friendly, considerate, humble, appreciative, and always loving and supporting me.

Somewhere, something incredible is waiting to be known.

Carl Sagan

1

Introduction

Architected materials (also referred to as metamaterials) are rationally designed structures which gain their properties from structure rather than composition. Since it was first shown that microstructures built from non-magnetic conducting sheets can exhibit effective magnetic permeability¹⁰⁴, the metamaterial concept has been quickly extended to photonic¹³⁶, acoustic⁷⁹ and mechanical⁶⁹ systems, leading to the design of a variety of materials with properties not previously thought possible. These structures, often made of periodic microstructure, can be found in different scales ranging from nanometer to kilometer (see Figure 1.1), and offer broad range of application in light weight structures, protective systems, energy/shock absorbent and impact resistant materials, energy harvesting devices, ultra-stiff or ultra-tough materials, soft actuators and sensors, noise canceling devices, tunable membrane filters, wave guiding and cloaking devices, vibration isolators, negative refraction systems and ultrasonic super lenses, switches and rectification devices, and acoustic/thermal diodes.

The recent interest in soft structures may lead to the next paradigm in the development of adaptive and actuating systems and devices^{64,42}. The use of the large deformation capability of soft materials as building components for soft structures, expands the ability of existing structures to reversibly deform and reconfigure, opening avenues for the design of adaptive and tunable systems such as soft and reconfigurable actuators and sensors^{56,88,31,107,87,101,156}, and switchable and programmable metamaterials^{126,109,148,130,124,155}.

Mechanical instabilities have been traditionally viewed as an inconvenience, with research focusing on how to avoid them. For almost two centuries researchers were always focusing on the maximum load carrying capacity of a structure and emphasis has been placed on the conditions of the onset of bifurcation. We change this prospective and exploit instabilities to design a new class of 3D materials that sense the sur-

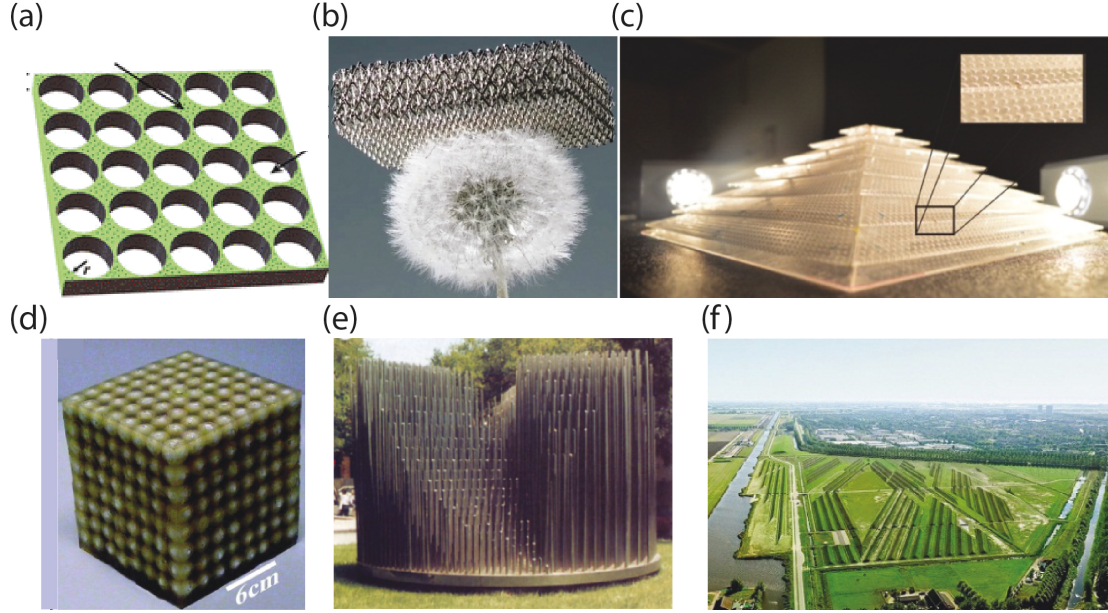


Figure 1.1: Architected structures ranging from nanometer to kilometer scale. (a) Heat management by thermocrystal⁸² (b) ultralight metallic microlattice¹²¹ (c) 3D broadband omnidirectional acoustic cloak¹⁶⁵ (d) locally resonant sonic materials⁷⁷ (e) sound attenuation by sculpture⁸⁹, and (f) Buitenschot noise-canceling landscape art park¹.

roundings and tune their shape and properties in response to external stimuli. More recently, the construction of mechanical metamaterials by harnessing elastic instabilities has attracted much attention for applications such as trapping elastic energy¹²⁵, soft actuators¹⁰¹, programming mechanical response^{40,109}, transforming wave propagation¹¹⁴, and controlling mechanical response of origami-inspired structures^{153,154}.

The ability to pattern materials in three dimensions is crucial for structural, optical, electronic, and energy applications. Using three-dimensional printing allows one to design and rapidly fabricate materials in complex shapes without the need for expensive tooling or fabrication techniques^{110,135,94,122,115}. For instance, recent advances in fabrication at micro- and macro-scales have enabled the design of metamaterials with electromagnetic properties that are not only distinct from their constituents, but

also previously not possible^{136,70,162}.

This thesis focuses on the design of soft and tunable architected materials to explore the opportunities on the connection between material's architecture and mechanics of the soft structures. Guided by theoretical, experimental and numerical analysis, I exploit large deformation capability of soft materials, mechanical instabilities, and geometric non-linearities to design novel systems and structures with tunable exceptional properties. This class of materials has found its way into the design of materials and systems, and received significant interest in recent years, not only because of their rich physics, but also for their broad range of applications. Examples include adaptive noise-canceling devices¹², reconfigurable origami-inspired waveguides⁸, auxetic metmaterials^{10,95}, protective fiber networks⁹, energy absorbent and shock resistant cellular structures^{96,7}, and acoustic switches¹¹. Remarkably, due to large deformation capability and full reversibility of soft constituent materials, the responses of the proposed designs are reversible, repeatable, and scale-independent, opening avenues for the design of a new class of soft, active, adaptive, programmable and tunable structures and systems.

This thesis is structured into four chapters:

In chapter 2, we report a new class of 3D mechanical metamaterial with negative Poisson's ratio. In particular, we exploit buckling to design three dimensional metamaterials that contract in the transverse direction under compressive loading regimes. These proposed metamaterials consist of an array of patterned elastomeric spherical shells, which due to a mechanical instability, undergo a significant isotropic volume reduction when deformed. The large geometric non-linearities introduced in the system by buckling are exploited to achieve a negative Poisson's ratio and retain this unusual property over a wide range of applied deformations. Here, we identify a li-

brary of auxetic building blocks and define procedures to guide their selection and assembly. The auxetic properties of these materials are demonstrated both through experimental and finite element simulation approaches and exhibit excellent qualitative and quantitative agreement. As a result of this unusual behavior, these proposed metamaterials could be useful for the design of protective and energy absorbing materials, efficient membrane filters with variable permeability, and acoustic dampeners¹⁰.

In chapter 3, we focus on elastic wave propagation through the Phononic crystals. In particular, we report a new class of three-dimensional adaptive phononic crystals whose dynamic response is controlled by mechanical deformation. Using finite element analysis, we demonstrate that the bandgaps of the proposed 3D structure can be fully tuned by the externally applied deformation. In fact, our numerical results indicate that the system acts as a reversible phononic switch: a moderate level of applied strain (i.e. -0.16) is sufficient to completely suppress the bandgap, and upon the release of applied strain, the deformed structure recovers its original shape, which can operate with a sizable bandgap under dynamic loading. In addition, we investigate how material damping significantly affects the propagation of elastic waves in the proposed 3D soft phononic crystal. We believe that our results pave the way for the design of a new class of soft, adaptive and re-configurable 3D phononic crystals, whose bandgaps can be easily tuned and switched on/off by controlling the applied deformation¹².

In chapter 4 and 5, we investigate the propagation of sound (acoustic waves) through the architected structures. In particular, in chapter 4, by combining numerical analyses and experiments we design a new class of architected materials to control the propagation of sound (also called acoustic metamaterials). The proposed system comprises an array of elastomeric helices in background air and is characterized by

frequency ranges of strong wave attenuation (bandgaps) in the undeformed configuration. Importantly, our results indicate that by axially stretching the helices such bandgaps can be suppressed, enabling the propagation of sound over all frequencies. The proposed concept expands the ability of existing acoustic metamaterials and paves the way for the design of a new class of materials and devices that enable better control and manipulation of sound¹¹.

In chapter 5, we combine numerical simulations and experiments to design a new class of reconfigurable waveguides based on 3D origami-inspired metamaterials. Our strategy builds on the fact that the rigid plates and hinges forming these structures define networks of tubes that can be easily reconfigured. As such, they provide an ideal platform to actively control and redirect the propagation of sound. Interestingly, we design reconfigurable systems that, depending of the externally applied deformation, can act as networks of waveguides oriented along either one or two or three preferential directions. Moreover, we demonstrate that the capability of the structure to guide and radiate acoustic energy along well predefined directions can be easily switched on and off, as the networks of tubes are reversibly formed and disrupted. The proposed designs expand the ability of existing acoustic metamaterials and exploit complex waveguiding to enhance the control of propagation and radiation of acoustic energy, opening avenues for the design of a new class of tunable acoustic functional systems⁸.

All in all, our proposed designs and investigations presented here shed new light on the rich static and dynamic responses of mechanical metamaterials, phononic crystals and acoustic metamaterials, pave the way for the design of a new class of soft, adaptive, programmable and tunable structures and systems with unprecedented performance and improved functionalities.

This chapter has already been published in:

S. Babae, J. Shim, J. C. Weaver, N. Patel, and K. Bertoldi, 3D Soft Metamaterials with Negative Poissons Ratio, *Advanced Materials* 2013, 25 (36):5044-5049.

2

Three-dimensional Soft Metamaterials with Negative Poisson's Ratio

2.1 OVERVIEW

When materials are uniaxially compressed, they typically expand in directions orthogonal to the applied load. Here, we exploit buckling to design a new class of three dimensional metamaterials with negative Poisson’s ratio that contract in the transverse direction under compressive loading regimes. These proposed metamaterials consist of an array of patterned elastomeric spherical shells, which due to a mechanical instability, undergo a significant isotropic volume reduction when deformed. The large geometric non-linearities introduced in the system by buckling are exploited to achieve a negative Poisson’s ratio and retain this unusual property over a wide range of applied deformations. Here, we identify a library of auxetic building blocks and define procedures to guide their selection and assembly. The auxetic properties of these materials are demonstrated both through experimental and finite element simulation approaches and exhibit excellent qualitative and quantitative agreement. As a result of this unusual behavior, these proposed metamaterials could be useful for the design of protective and energy absorbing materials, efficient membrane filters with variable permeability, and acoustic dampeners.

2.2 INTRODUCTION

Metamaterials are rationally designed artificial materials which gain their properties from structure rather than composition. Since it was first shown that microstructures built from non-magnetic conducting sheets can exhibit effective magnetic permeability¹⁰⁴, the metamaterial concept has been quickly extended to photonic¹³⁶, acoustic⁷⁹ and mechanical⁶⁹ systems, leading to the design of a variety of materials with properties not previously thought possible.

The Poisson’s ratio defines the ratio between the transverse and axial strain⁴⁷. Materials that are uniaxially compressed typically expand in the directions orthogonal to the applied load. Counter-intuitively, materials with a negative Poisson’s ratio (auxetic materials) contract in the transverse direction^{66,36}. The first reported example of an artificial auxetic material was a foam with re-entrant cells that unfolded when stretched⁶⁵. Since then, several periodic 2-D geometries and mechanisms have been suggested to achieve a negative Poisson’s ratio⁷⁵. While auxetic responses have been demonstrated in many crystals¹⁴, very few designs of synthetic 3-D auxetic materials have been proposed⁶⁹. Analytical studies have identified 3-D auxetic systems consisting of networks of beams⁵¹, multipods¹⁰⁵ and rigid units⁶ and only very recently, a metallic 3-D architecture based on a bow-tie functional element has been fabricated²⁵. In all of these systems, however, the auxetic behavior is exhibited only in the limit of small strains, and the design of 3-D auxetic systems capable of retaining these unusual properties at large strains still remains a challenge⁶⁹.

The design of metamaterials capable of responding reversibly to changes in their environment is of fundamental importance for the development of the next generation of actuators and sensors, tunable optics and smart responsive surfaces^{131,18}. Furthermore, a remarkable feature of responsive metamaterials is that any of their properties can be switched or fine-tuned just by applying a stimulus to alter their initial architecture.

In order to successfully design a new class of 3-D auxetic materials capable of retaining this unusual response over a wide range of applied strains, we exploited the large geometric non-linearities introduced in the system by instabilities. Through a combination of desktop-scale experiments and finite element (FE) simulations, we investigated the auxetic responses of these structures, finding excellent qualitative and

quantitative agreement. Since the 3-D auxetic behavior is induced by elastic buckling, we have named these new materials "Bucklicrystals". We believe that these Bucklicrystals open new design avenues for the construction of 3-D auxetic materials over a wide range of length scales.

2.3 RESULTS AND DISCUSSION

We began by recognizing that a structural unit capable of isotropic volume reduction represents the ideal building block to construct 3-D auxetic metamaterials whose response can be controlled by the application of a stimulus. Such responses have been recently demonstrated for patterned spherical shells¹²⁹, where a significant change in volume has been observed as a result of an elastic instability. The hole arrangement on the spherical shell has also been explored, showing that only five patterns comprising of 6, 12, 24, 30 and 60 holes are possible for such building blocks¹²⁹. Note that these five spherical structures can be classified into two symmetry groups: the shells with 6, 12 and 24 holes have octahedral symmetry, while those with 30 and 60 holes have icosahedral symmetry.

Having identified the building blocks, we then defined procedures to guide their assembly. Here, we focused on cubic crystal systems (i.e., simple cubic (*sc*), body-centered cubic (*bcc*), and face-centered cubic (*fcc*)) because of their simplicity and highest symmetry order out of the seven lattice systems. Since it was necessary that both the building blocks and the metamaterial have octahedral symmetry, only spherical shells with 6, 12 and 24 holes were considered in this study (Figure 2.1a and Figure A.1). Furthermore, for the sake of simplicity and ease of scalability, we constructed each metamaterial from a single type of building block.

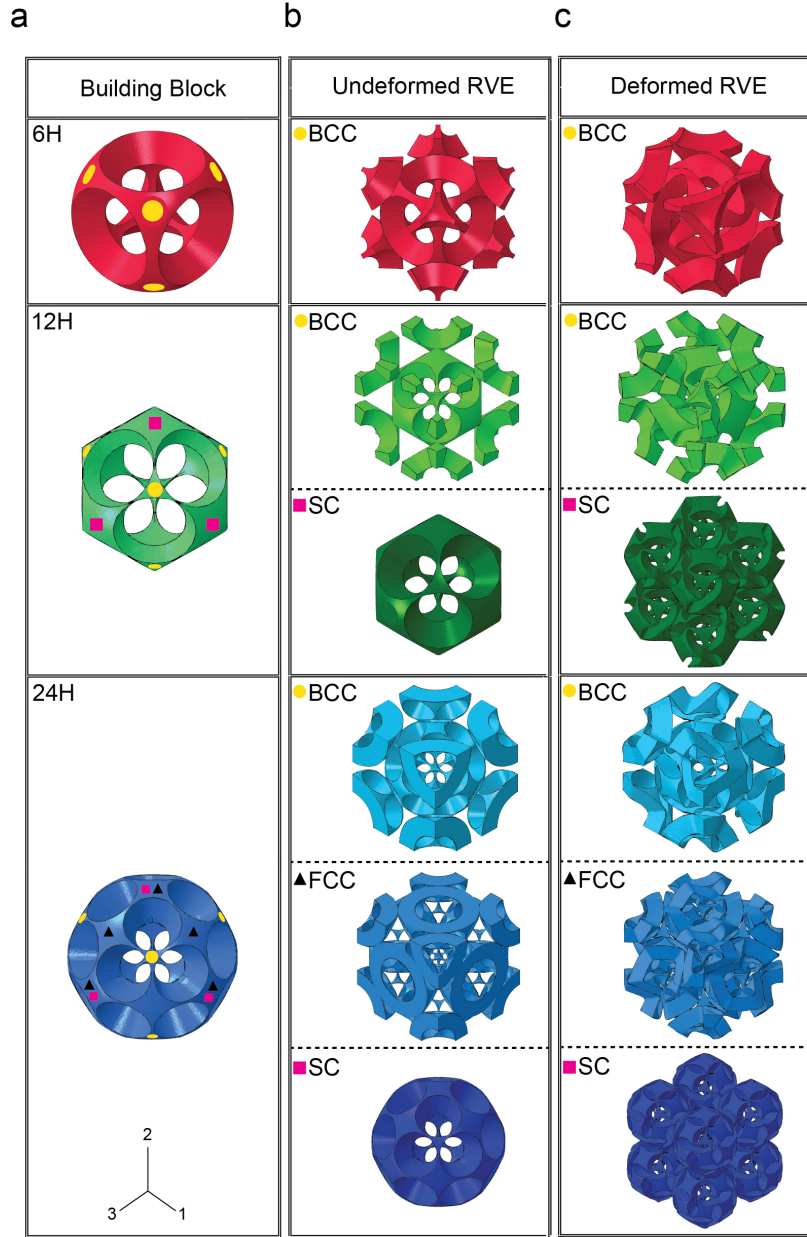


Figure 2.1: Gallery of Bucklicrystals. a) Building blocks with 6, 12 and 24 holes. For the sake of simplicity, we always color the building blocks with 6, 12 and 24 holes with red, green and blue, respectively. Moreover, we also identify the junctions where the building blocks are attached to the surrounding units using yellow circles, black triangles, and magenta squares for *bcc*, *fcc*, and *sc* packing configurations, respectively. b) Representative volume elements (RVE) for the Bucklicrystal in the undeformed configuration. c) Buckled configurations for the RVEs under uniaxial compression.

Since each building block has a limited number of sites where adjacent building blocks can be attached to each other (see markers in Figure 2.1a) and metamaterials with octahedral symmetry can be built only via connecting identical junctions (i.e., junctions identified by the same type of markers in Figure 2.1a), only six different Bucklicrystals can be built (Figure 2.1b and Figure A.2): *bcc* crystals using building blocks with 6, 12 and 24 holes, *sc* crystals using building blocks with 12 and 24 holes, and *fcc* crystal using building blocks with 24 holes. Having identified all possible configurations for the Bucklicrystals, we next investigated their response through a combination of experiments and numerical simulations.

We first fabricated and mechanically tested a Bucklicrystal consisting of a *bcc* array of building blocks with 6 holes. Using additive manufacturing for the fabrication of individual molds for each unit cell, we fabricated the building blocks from a soft silicone-based rubber (Vinyl Polysiloxane with Young’s modulus, $E = 784\text{ KPa}$). The geometry of the building block comprises a spherical shell (inner diameter $d_i = 19.8\text{ mm}$ and wall thickness $t = 7.1\text{ mm}$) that is patterned with a regular array of 6 circular voids that are slightly tapered (22 mm and 13 mm maximum and minimum diameter, respectively) (Figure 2.1 and Figure A.1). Ninety one identical building blocks were fabricated and subsequently joined to form a *bcc* crystal using the same polymer as an adhesive agent.

The Bucklicrystal was then tested under uniaxial compression and the evolution of the microstructure was monitored taking tomographic images at five different levels of the applied nominal strain (calculated as change of height of the sample divided by the original height), $\epsilon_{22}^{\text{applied}} = -0.03, -0.08, -0.15, -0.20, -0.30$, with a micro-CT X-ray scanner (HMXST225, X-Tek). Figure 2.2 shows isometric and mid-cross sectional views of the structure in the undeformed ($\epsilon_{22}^{\text{applied}} = 0$ - Figure 2.2a) and

deformed ($\epsilon_{22}^{\text{applied}} = -0.20$ - Figure 2.2b) configurations. Furthermore, a sequence of progressively deformed shapes of the inner-most building block at different levels of strain is shown in Figure 2.2c. These snapshots clearly demonstrate that structural transformations induced by instabilities occur when the Bucklicrystal is compressed. All the building blocks are found to shrink significantly in all directions and their initially circular holes on the spherical shell transform into elongated, almost closed ellipses. Moreover, Figure 2.2a,b clearly show that all of the lateral boundaries of the deformed Bucklicrystal bend inwards, a clear indication of a 3-D negative Poisson's ratio.

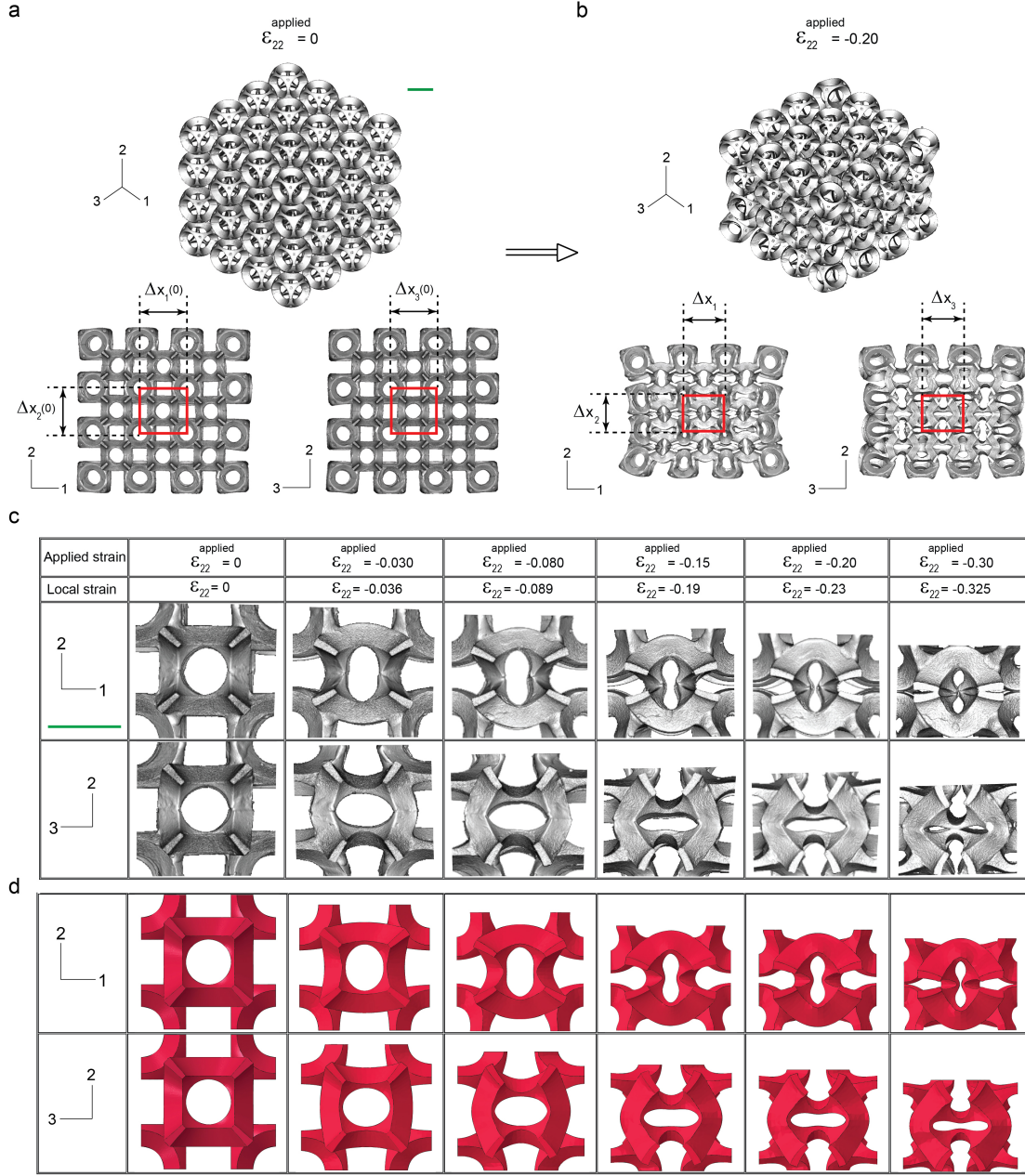


Figure 2.2: Experimental (micro-CT) and numerical images of the 6-hole Bucklicrystal. a) Iso-metric and cross-sectional views of the undeformed crystal from micro-CT X-ray imaging machine. b) Iso-metric and cross-sectional views of the uniaxially compressed crystal ($\epsilon_{22}^{\text{applied}} = -0.20$) from micro-CT volumetric data sets. In the cross sectional views, the inner-most RVE is highlighted by a red box. $\Delta x_i(0)$ and Δx_i , $i = 1, 2, 3$, are the edge length of the red box in the i direction for undeformed and buckled crystals, respectively. c) Magnified views of the inner-most RVE taken from micro-CT X-ray scanning at different levels of strains. d) Corresponding pictures taken from simulation. (Green scale bars: 20 mm)

Recognizing that the response of the specimens is necessarily influenced by boundary conditions at both the loaded and the traction-free faces, we focused on the innermost building block (which can be considered as the representative volume element (RVE) for the corresponding infinitely periodic structure) and quantitatively estimated its deformation using image post-processing. First, each tomographic image was size-calibrated using the known shell thickness ($t = 7.1 \text{ mm}$), which was only marginally affected by deformation. We then tracked the centroids of the four voids surrounding the RVE in both the 1-2 and the 2-3 planes (see vertices of the red rectangle in Figure 2.2a,b) and used them to calculate centroid-to-centroid distances along the three directions, denoted by Δx_1 , Δx_2 , and Δx_3 . Prior to compression, the value for all of these quantities was $\Delta x_i(0) \simeq 38 \text{ mm}$, $i = 1, 2, 3$. Local normal strains were then obtained as $\epsilon_{ii} = \langle \Delta x_i \rangle / \Delta x_i(0)$, where the angular bracket $\langle \cdot \rangle$ denotes ensemble average over all distances under consideration. It is worth noting that the measured local longitudinal strains, denoted by ϵ_{22} , were higher than those applied, denoted by $\epsilon_{22}^{\text{applied}}$. This was expected since the building blocks in close proximity of the two plates used to compress the structure were highly constrained by friction and were unable to fully deform.

In Figure 2.3a, we present the dependence of the transverse strains ϵ_{11} and ϵ_{33} on the longitudinal strain ϵ_{22} . The error bars on the experimental points were obtained from the standard deviation of the two values of Δx_i used in each averaging. Remarkably, the data clearly show that upon increasing the compressive strain ϵ_{22} , both transverse strains decrease, indicating that the structure contracts in both lateral directions. To quantify these lateral contractions, the Poisson's ratios were calculated from the engineering strain as $\nu_{ij} = -\epsilon_{ii}/\epsilon_{jj}$. The estimates of ν_{ij} were plotted as a function of ϵ_{22} in Figure 2.3b. The evolution of ν_{21} and ν_{23} was characterized by two

subsequent regimes: a decreasing regime followed by a plateau. Initially both Poisson's ratios monotonically decrease. They became negative at $\epsilon_{22} \simeq -0.03$, and eventually reached the value $\nu \simeq -0.4$ and plateau at $\epsilon_{22} \simeq -0.20$, demonstrating that the response of the Bucklicrystal was auxetic over a wide range of deformations. Finally we note that, since the specimens are made of an elastomeric material, the process was fully reversible and repeatable. Upon release of the applied vertical displacement, the deformed structures recovered their original configurations.

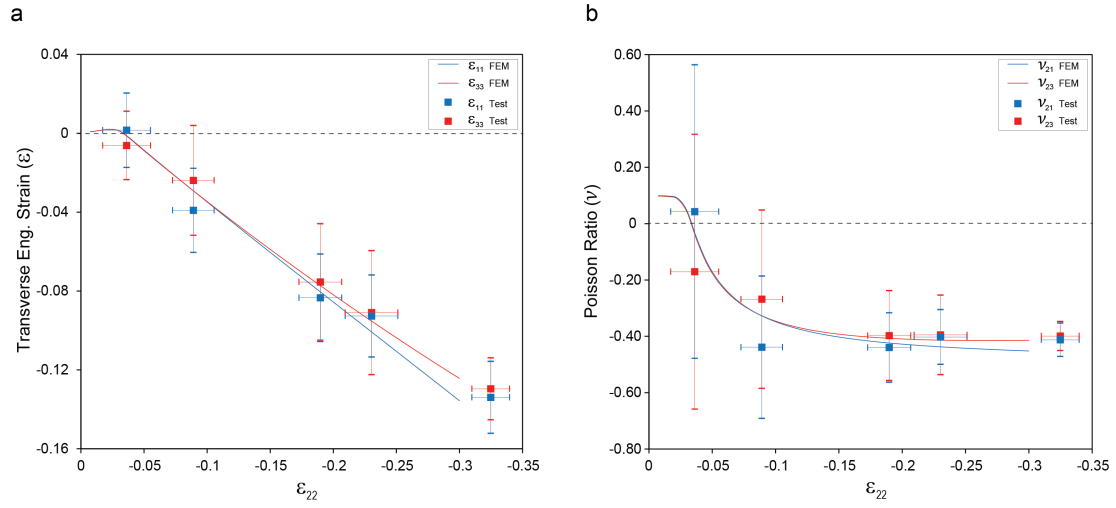


Figure 2.3: Evolution of transverse strains and Poisson's ratios for the 6-hole Bucklicrystal. a) Evolution of the transverse engineering strain ϵ_{11} and ϵ_{33} as a function of the applied longitudinal strain ϵ_{22} . b) Evolution of the Poisson's ratios (ν_{21} and ν_{23}) of the 6-hole Bucklicrystal as a function of compressive strain ϵ_{22} . The finite element results (solid lines) are in good agreement with the experimental data (square markers).

Next, we performed finite element (FE) simulations of the 6-hole Bucklicrystal. To verify that the auxetic behavior measured in the experiments was not affected by the boundary conditions, we considered the structure to be infinite and investigate the response of a representative volume element (RVE) under uniaxial compression using periodic boundary conditions. All analyses were performed on the cubic RVE

comprising a central building block connected to one-eighth of the building block at each junction (the junctions and the RVE are shown in Figure 2.1a).

We first investigated the stability of the Bucklicrystal through Bloch wave analysis^{16,43} and the analysis detects a mechanical instability at $\epsilon_{22} = -0.03$. The post-buckling response of the Bucklicrystal was then simulated by introducing a small imperfection in the initial geometry. In Figure 2.2d we present a sequence of the progressive collapse of the Bucklicrystal obtained from FE simulations, which is in remarkable qualitative agreement with the experiments for the same geometric and material parameters (Figure 2.2c). The snapshots clearly revealed that in this Bucklicrystal, mechanical instabilities act as a functional mode of actuation, inducing the spherical collapse of every building block while keeping the structure periodic. To better characterize the response of the structure, in Figure 2.3 we report the evolution of the lateral strains (ϵ_{11} , ϵ_{33}) and Poisson's ratios (ν_{21} , ν_{23}) as a function of ϵ_{22} , showing an excellent quantitative agreement with our experimental results. It is worth noting that since after buckling, the initial cubic RVE changes into a rectangular parallelepiped, for large values of longitudinal strain $\epsilon_{33} \neq \epsilon_{11}$ and $\nu_{21} \neq \nu_{23}$. This can be clearly seen in Figure 2.2d for $\epsilon_{22}^{\text{applied}} = -0.30$, where all of the ligaments in the 1-2 plane are touching, while in the 2-3 plane, they are still separated from each other.

Given the excellent qualitative and quantitative agreement found between our experiments and simulations, we proceeded by focusing primarily on the FE simulation results to further explore the buckling-induced auxetic behavior of all the Bucklicrystals identified in Figure 2.1. Each building block is fully characterized by two adimensional parameters: porosity, denoted by ψ , (defined as the ratio of the void volume to the intact spherical shell volume) and thickness over inner radius ratio, denoted by t/r_i ¹²⁹. All crystals were constructed using building blocks characterized by the same

parameters used for the 6-hole crystal investigated above, $\psi = 0.733$ and $t/r_i = 5/7$.

All analyses were performed on cubic RVEs (Figure 2.1b and Figure A.2): (i) for *bcc* configurations (12- and 24-hole), they were constructed as described for the 6-hole *bcc* case; (ii) for the *sc* configurations (12- and 24-hole), a single building block was used as RVEs; (iii) for the *fcc* configuration (24-hole), RVEs were built such that they comprise of 6 half-building blocks located in the middle of the cube faces, attaching to 8 one-eighth of the building blocks at the corners. It is worth noting that the use of building blocks characterized by the same parameters ψ and t/r_i resulted in Bucklicrystals with different initial global porosities, denoted by $\bar{\psi}$ (i.e., $\bar{\psi}_{sc} = 0.888$, $\bar{\psi}_{bcc} = 0.854$ and $\bar{\psi}_{fcc} = 0.842$). In all Bucklicrystals, instabilities of short wavelength were found to be critical, leading to spherical collapse of all the building blocks. The values of critical strain obtained from Bloch wave analysis were $\epsilon_{22}^{cr} = -0.030, -0.030, -0.041, -0.020, -0.026$, and -0.023 for 6-hole *bcc*, 12-hole *bcc* and *sc*, and 24-hole *bcc*, *sc* and *fcc*, respectively. Moreover, the deformed mode shape of the RVEs are reported in Figure 2.1c. Note that for the *sc* configurations, when the critical instability occurs, the periodicity of the crystal was altered and a new RVE comprised of 8 building blocks was found (RVE size = $2 \times 2 \times 2$ in 1, 2, and 3 directions). Furthermore, in the building blocks with 12 or 24 holes, the identical junctions (i.e., the sites where adjacent building blocks can be attached to each other) rotate all in the same direction during folding (Figure A.6). As a result, in Bucklicrystals comprising arrays of building blocks with 12 or 24 holes, the folded units have two potentially different orientations (Figure A.7). In contrast, in the 6-hole building block, half of the junctions rotate clockwise and half counterclockwise (Figure A.6). As a result, in the deformed configuration of the 6-hole *bcc* Bucklicrystal, all of the folded building blocks are oriented in exactly the same way (Figure A.8).

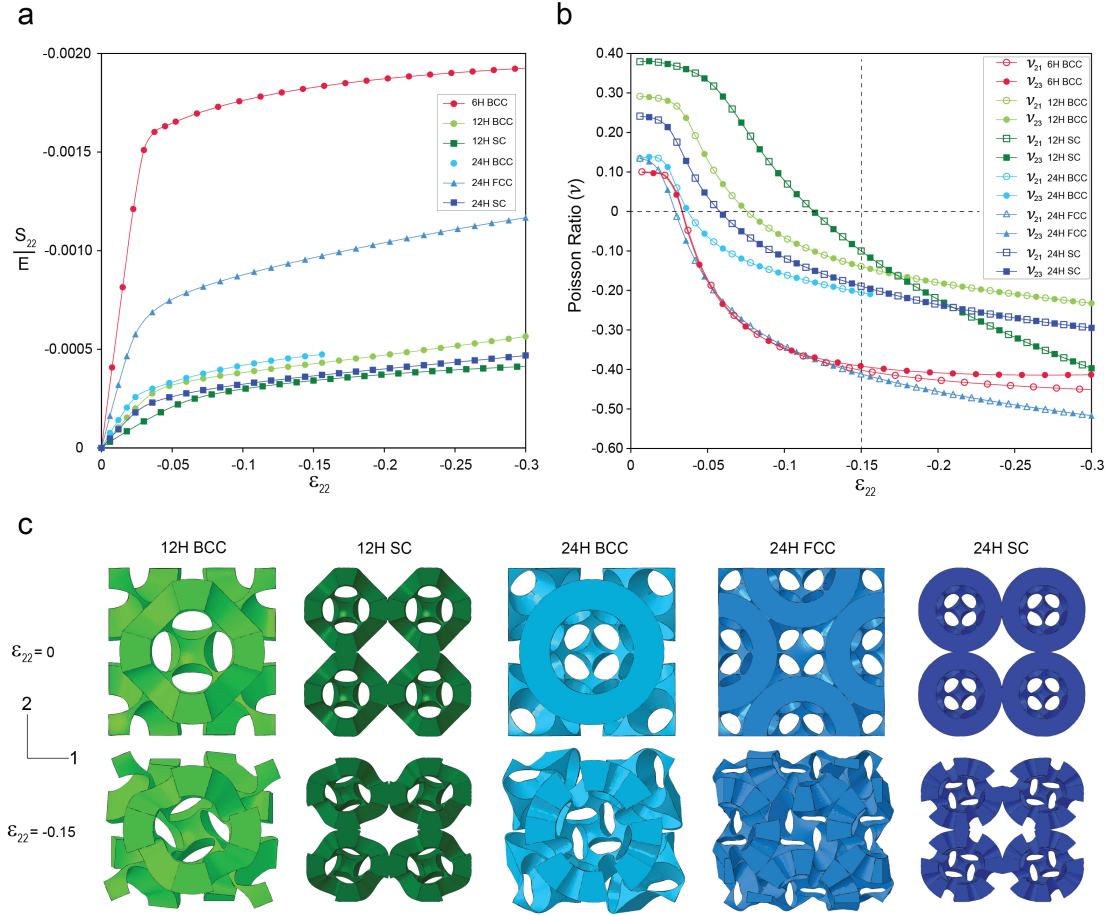


Figure 2.4: Mechanical response of Bucklicrystals. a) Nominal stress-strain curves from uniaxial compression in 2-direction for all of the Bucklicrystals. The stress is normalized with respect to the elastic modulus of the bulk elastomeric material. b) Evolution of the Poisson's ratios vs. nominal strain in 2- direction for all the Bucklicrystals. c) Cross sectional views of undeformed ($\epsilon_{22} = 0$) and deformed ($\epsilon_{22} = -0.15$) configurations of 12- and 24-hole Bucklicrystals.

A more quantitative comparison between the responses of all of the Bucklicrystals can be made by inspecting the evolution of stresses and Poisson's ratios. Figure 2.4 shows the evolution of the normalized nominal stress S_{22}/E as a function of the longitudinal strain ϵ_{22} . The response of all configurations is characterized by a linear elastic regime followed by a stress plateau. The departure from linearity is the result of

buckling and corresponds to a sudden transformation in the periodic pattern as shown in Figure 2.4c, where snapshots of undeformed and deformed ($\epsilon_{22} = -0.15$) configurations are presented. Note that all of the crystals are uniaxially compressed up to the limit when the ligaments surrounding the holes begin to contact one another. This results in a maximum longitudinal strain $\epsilon_{22} \simeq -0.30$ for all the crystals, except the *bcc* crystal comprising of an array of 24-hole building blocks in which the ligaments come into contact with each other at $\epsilon_{22} \simeq -0.15$. Finally, it is worth noting that all the structures exhibit a typical behavior for cellular solids characterized by an initial linear elastic regime and a stress plateau following thereafter. The final steep portion of the curve (i.e., densification) is not observed since the applied strain is not large enough to completely collapse the holes.

The evolution of the Poisson's ratios as a function of ϵ_{22} is also presented in Figure 2.4b. All of the Bucklicrystals are characterized by initial positive values of ν , a steeply decreasing regime initiated at the onset of instability, and a final negative plateau by further compression. Therefore, in all the Bucklicrystals, an evolution of the Poisson's ratio from positive to negative is observed; this transition occurs first in the 24-hole *fcc* Bucklicrystal (at $\epsilon_{22} \simeq -0.04$) and last in the 12-hole *sc* (at $\epsilon_{22} \simeq -0.12$). Remarkably, once the crystals become auxetic, they retain this unusual property even at large strains. At $\epsilon_{22} = -0.30$, all configurations are characterized by negative Poisson's ratio, ranging from -0.2 for the 12-hole *bcc* crystal to -0.5 for the 24-hole *fcc*. Finally, we note that all the crystals, except the 6-hole case, retain the transversely symmetric behavior (i.e., $\nu_{21} = \nu_{23}$) even at large strains.

2.4 CONCLUSIONS

Our finding of buckling-induced auxetic behavior provides a fundamentally new way for generating 3-D materials with a negative Poisson's ratio. Our results offer a unique mechanism with a range of advantages: (*i*) the proposed design rules can be applied to various length-scales; (*ii*) the reconfiguration can occur upon application of different stimuli depending on the types of materials; (*iii*) the transformation can be made fully reversible; and (*iv*) the auxetic behavior is retained over a wide range of applied strain. While the fabrication process described here is not tractable for the large scale production of these materials, it provides an effective proof of concept method to construct various models and evaluate their mechanical performance. Based on these initial observations, we are currently developing large-scale 3D-printed sacrificial molds from soluble materials which would allow the bucklicrystals to be cast in a single step process. This new approach reduces the production time of these materials by more than 90% and permits the exploration of more complex geometries. From a practical perspective, the full control over the desired outcome in combination with the wealth of different length scales, materials, stimuli, and geometrical designs provides reversibly auxetic architectures with a broad field of applications ranging from energy absorbing materials to tunable membrane filters. Finally, although mechanical instabilities have been traditionally viewed as a failure mode with research focusing on how to avoid them, here we change this perspective and exploit instabilities to design a new class of 3-D auxetic materials.

2.5 MATERIALS AND METHODS

2.5.1 MATERIALS

A silicone-based rubber (commercial name: Elite Double 32, Zhermack) was used to cast the experimental specimen. The material properties were measured through tensile testing, up to the true strain of $\epsilon = 0.60$. No hysteresis was found during loading and unloading. The constitute behavior was accurately captured by a Yeoh hyperelastic model¹⁶¹, whose strain energy is $U = \sum_{i=1}^3 C_{i0} (\bar{I}_1 - 3)^i + (J - 1)^{2i} / D_i$ where $C_{10} = 131 \text{ KPa}$, $C_{20} = 0 \text{ KPa}$, $C_{30} = 3.5 \text{ KPa}$, $D_1 = D_2 = D_3 = 154 \text{ GPa}^{-1}$. Here, $\bar{I}_1 = \text{tr} [\text{dev} (\mathbf{F}^T \mathbf{F})]$, $J = \det \mathbf{F}$, and \mathbf{F} is the deformation gradient. Two of the Yeoh model parameters are related to the conventional shear modulus, denoted by G_0 , and bulk modulus, denoted by K_0 , at zero strain: $C_{10} = G_0/2$, $D_1 = 2/K_0$.

2.5.2 FABRICATION OF THE BUILDING BLOCKS

A mold was fabricated using a 3-D printer (Objet Connex500) to cast one half of a spherical shell. After de-molding, two halves were joined using the same polymer as adhesive agent. The specimen fabricated for this study has the thickness of $t = 7.1 \text{ mm}$, the inner diameter of $d_i = 19.8 \text{ mm}$, and the outer diameter of $d_o = 34.0 \text{ mm}$.

2.5.3 TESTING OF THE BUCKLICRYSTAL

After preparing 91 spherical shells, all the shells were joined using the same polymer as adhesive agent. The dimension of the Bucklicrystal was Height \times Width \times Depth = $144.0 \times 141.0 \times 141.0 \text{ mm}$. In order to observe the evolution of the Poisson's ratio of the Bucklicrystal, we applied five different levels of vertical deformation, i.e., engineer-

ing strains of $\epsilon_{22} = -0.03, -0.08, -0.15, -0.20$, and -0.30 with respect to the height of the Bucklicrystal. At the strain level of interest, we immobilized the specimen using a fixture made of acrylic plates, nylon bolts/nuts and inch-thick closed-cell foam plates placed between the specimen and the fixture (Figure A.3). The foam plates were used as a low electron density spacer that would be nearly invisible in the acquired x-ray transmission images and thus not interfere with volume rendering of the higher electron density silicone elastomer Bucklicrystal. The specimen with the fixture was put into a micro-CT X-ray scanner (HMXST225, X-Tek) for image data collection. Once the 3-D volumes of the inside of the specimen were reconstructed, the cross-sectional views of interest were extracted.

2.5.4 NUMERICAL SIMULATIONS

The simulations were carried out using the commercial Finite Element package Abaqus (SIMULIA, Providence, RI). The Abaqus/Standard solver was employed for all the simulations, i.e., for both microscopic and macroscopic instability analyses and post-buckling analysis. Models were built using quadratic solid elements (ABAQUS element type C3D10M with a mesh sweeping seed size of 1 *mm* and the analyses were performed under uniaxial compression. We used first four eigenvalues from instability analysis as imperfection on non-linear post Buckling analysis. More details on the FE simulations are provided in Appendix A.

This chapter has already been published in:

S. Babae, P. Wang, and K. Bertoldi, Three-dimensional Adaptive Soft Phononic Crystals,
Journal of Applied Physics 2015, 117 (24):244903.

3

Three-dimensional Adaptive Soft Phononic Crystals

3.1 OVERVIEW

We report a new class of three-dimensional adaptive phononic crystals whose dynamic response is controlled by mechanical deformation. Using finite element analysis, we demonstrate that the bandgaps of the proposed 3D structure can be fully tuned by the externally applied deformation. In fact, our numerical results indicate that the system acts as a reversible phononic switch: a moderate level of applied strain (i.e. -0.16) is sufficient to completely suppress the bandgap, and upon the release of applied strain, the deformed structure recovers its original shape, which can operate with a sizable bandgap under dynamic loading. In addition, we investigate how material damping significantly affects the propagation of elastic waves in the proposed 3D soft phononic crystal. We believe that our results pave the way for the design of a new class of soft, adaptive and re-configurable 3D phononic crystals, whose bandgaps can be easily tuned and switched on/off by controlling the applied deformation.

3.2 INTRODUCTION

Three-dimensional (3D) periodic structures are attracting significant interest not only for their remarkable static properties^{44,120,164,7}, but also for their ability to control the propagation of elastic waves through bandgaps, i.e. frequency ranges of strong wave attenuation^{85,34}. Such bandgaps can be formed either by Bragg scattering^{132,61,55} or by exploiting local resonance within the medium^{77,137,108,22}. Bragg-type bandgaps are intrinsic to order and typically occur at wavelengths of the order of the unit cell size, whereas locally resonant bandgaps arise in the vicinity of the natural frequency of the resonating units and are modestly affected by the spatial periodicity of the system.

While most of the proposed 3D phononic crystals operate in fixed ranges of fre-

quencies that are impractical to tune and control after the assembly^{59,58,163,103,157,116}, it has been shown that the dynamic responses of structures could be altered by mechanically deforming them^{32,147,57}. However, a large amount of loading is typically required to significantly affect the position and width of the bandgaps.

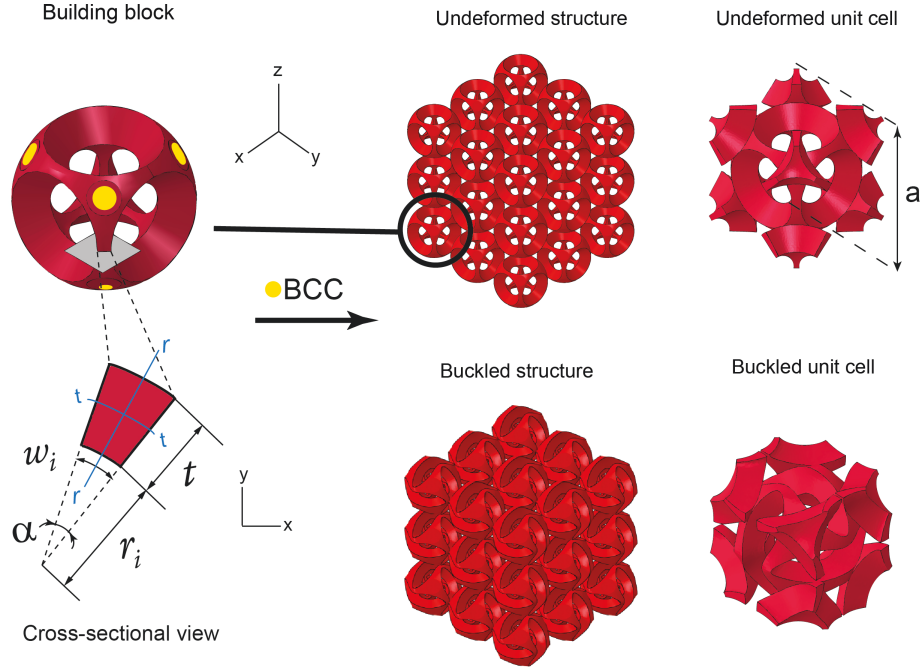


Figure 3.1: Tunable 3D phononic crystal composed of a periodic array of structured shells arranged to form a body centered cubic (*bcc*) lattice. When compressed, this structure undergoes an instability, which results in folding of all the building blocks. Each structured shell is fully characterized by two design parameters: the angle α that defines the narrowest width of the ligament, and the ratio $\tau = w_i/t$ between the inner narrowest width of the ligaments and the radial shell thickness.

It has been recently demonstrated that the tunability of 2D phononic crystals can be significantly enhanced by triggering mechanical instabilities along the loading path^{16,149,114,127}. In fact, the instabilities may induce dramatic homogeneous and reversible changes of the geometry, that can be exploited not only to alter, but also

to turn on and off the bandgaps even under moderate levels of applied deformation. However, although recent studies have shown that buckling can be an effective way to achieve better tunability of 2D phononic devices^{127,96,148}, no similar studies have been reported for 3D systems.

In this study, we focus on a 3D soft crystal consisting an array of elastomeric patterned spherical shells (see Figure 3.1). This structure has been recently shown to undergo an instability under uniaxial compression which results in folding of all the building blocks and macroscopic auxetic behavior¹⁰. Here, we investigate numerically the effect of the applied compression on the propagation of small-amplitude elastic waves, aiming to the design of a 3D reconfigurable phononic crystal with enhanced tunability. To this end, first we identify the geometric parameters leading to the widest bandgap in the undeformed configuration and then investigate the effect of the applied compression on the propagation of elastic waves. Finally, since elastomeric materials are dissipative, we study how material damping affects the dynamic response of the system.

3.3 3D PHONONIC CRYSTAL

The 3D structure investigated in this study is composed of a periodic array of structured shells arranged to form a body centered cubic (*bcc*) crystal. Each spherical shell is patterned with a regular array of six circular voids and is fully characterized by two design parameters^{10,129}: the angle α that defines the narrowest width of the ligament, and the ratio $\tau = w_i/t$ between the inner narrowest width of the ligaments and the radial shell thickness (see Figure 3.1).

The response of our 3D structure is conveniently captured using the unit cell shown

in Figure 3.1. Such unit cell is a cube with edges $a = 4r_o/\sqrt{3}$ (r_o is the outer radius of the spherical shell) and comprises two structured shells - one full shell at the center with eight one-eighths attached to it.

Finally, the porosity of the 3D structure can be calculated as

$$\bar{\psi} = 1 - \frac{2 V_{shell}}{V_{unit}}, \quad (3.1)$$

where $V_{unit} = a^3$ is the volume of the cubic unit cell, V_{shell} is the volume fraction of the structured shell and the pre-factor 2 is the number of structured shells in each unit cell. Note that V_{shell} is simply obtained by subtracting the volume of the six voids from the volume of the intact shell,

$$V_{shell} = V_{intact\ shell} - 6 V_{void}, \quad (3.2)$$

where

$$V_{intact\ shell} = \frac{4}{3}\pi(r_o^3 - r_i^3), \quad (3.3)$$

and

$$V_{void} = \frac{2}{3}\pi(r_o^3 - r_i^3) [1 - \cos(\pi/4 - \alpha/2)], \quad (3.4)$$

r_i denoting the inner radius of the spherical shell¹²⁹. Combining Eqs. (3.1) - (3.4), the porosity of the 3D crystal can be obtained as

$$\bar{\psi} = 1 - \frac{8\pi(r_o^3 - r_i^3) [-2 + 3 \cos(\pi/4 - \alpha/2)]}{3(4r_o/\sqrt{3})^3}. \quad (3.5)$$

3.4 GENERAL FORMULATION

Here, we present the governing equations and material model, which are employed in the numerical calculations.

3.4.1 GOVERNING EQUATIONS

The deformation of the 3D phononic crystal is described by the deformation gradient

$$\mathbf{F} = \frac{\partial \mathbf{x}}{\partial \mathbf{x}_0}, \quad (3.6)$$

mapping a point in the material from the reference position \mathbf{x}_0 to its current location \mathbf{x} . The material is assumed to be hyperelastic, characterized by a strain energy function $W = W(\mathbf{F})$, which is defined in the reference configuration. The first Piola-Kirchhoff stress \mathbf{S} is thus related to the deformation gradient \mathbf{F} by

$$\mathbf{S} = \frac{\partial W}{\partial \mathbf{F}}. \quad (3.7)$$

In the absence of body forces, the equation of motions in the reference configuration can be written as

$$\text{Div } \mathbf{S} = \rho_0 \frac{D^2 \mathbf{x}}{Dt^2}, \quad (3.8)$$

where Div represents the divergence operator in the undeformed/reference configuration, D/Dt is the material time derivative and ρ_0 denotes the reference mass density.

To investigate the effect of the applied deformation on the propagation of small-amplitude elastic waves, incremental deformations superimposed upon a given state of finite deformation are considered. Denoting with $\dot{\mathbf{S}}$ the increment of the first Piola-

Kirchhoff stress, the incremental forms of the governing equations is given by

$$\text{Div } \dot{\mathbf{S}} = \rho_0 \frac{D^2 \dot{\mathbf{x}}}{Dt^2}, \quad (3.9)$$

where $\dot{\mathbf{x}}$ denotes the incremental displacements. Furthermore, linearization of the constitutive equation (3.7) yields

$$\dot{\mathbf{S}} = \mathbb{L} : \dot{\mathbf{F}}, \quad \text{with } \mathbb{L}_{ijkl} = \frac{\partial^2 W}{\partial F_{ij} \partial F_{kl}}, \quad (3.10)$$

where $\dot{\mathbf{F}}$ denotes the the incremental deformation gradient.

The incremental boundary value problem is often formulated in an updated Lagrangian formulation, where the deformed state is used as the reference configuration for the calculation of the incremental quantities⁹⁸. Push-forward transformations allow the introduction of the incremental updated stress quantity Σ given by

$$\Sigma = \frac{1}{J} \dot{\mathbf{S}} \mathbf{F}^T. \quad (3.11)$$

For a non-linear elastic material, the incremental constitutive equation takes the linear form

$$\Sigma = \mathbb{C} : \text{grad } \mathbf{u}, \quad (3.12)$$

to the first order, where grad denotes the gradient operator in the deformed/current configuration, $\mathbf{u} \doteq \dot{\mathbf{x}}$ and

$$\mathbb{C}_{ijkl} = J^{-1} F_{jn} F_{lq} \frac{\partial^2 W}{\partial F_{in} \partial F_{kq}}. \quad (3.13)$$

Finally, the incremental equations of motions take the form

$$\operatorname{div} \boldsymbol{\Sigma} = \rho \frac{d^2 \mathbf{u}}{dt^2}, \quad (3.14)$$

where div represents the divergence operator in the deformed/current configuration, ρ denotes the current material density and d/dt is the spatial time derivative.

Here, we focus on the propagation of small-amplitude elastic waves defined by

$$\mathbf{u}(\mathbf{x}, t) = \tilde{\mathbf{u}}(\mathbf{x}) \exp(-i\omega t), \quad (3.15)$$

where ω is the angular frequency of the propagating wave, and $\tilde{\mathbf{u}}$ denotes the magnitude of the incremental displacement. It follows from (3.12) that

$$\boldsymbol{\Sigma}(\mathbf{x}, t) = \tilde{\boldsymbol{\Sigma}}(\mathbf{x}) \exp(-i\omega t), \quad (3.16)$$

so that equations (3.14) become

$$\operatorname{div} \tilde{\boldsymbol{\Sigma}} = \rho \omega^2 \tilde{\mathbf{u}}, \quad (3.17)$$

which represent the frequency-domain wave equations.

3.4.2 MATERIAL MODEL

The 3D phononic crystal is assumed to be made of silicon rubber. The response of such material is captured using a nearly incompressible Neo-Hookean model¹⁴³, whose

strain energy density is given by

$$W(I_1, J) = \frac{G}{2}(I_1 - 3) - G \log(J) + \frac{K}{2}(J - 1)^2, \quad (3.18)$$

where $I_1 = \text{trace}(\mathbf{F}^T \mathbf{F})$, $J = \det(\mathbf{F})$, and \mathbf{F} is the deformation gradient. Moreover, G and K are the initial shear and bulk moduli of the material, respectively.

Substituting (3.18) into (3.7) and (3.10), the nominal stress \mathbf{S} and the incremental modulus \mathbb{L} are obtained as

$$\mathbf{S} = G\mathbf{F} + [KJ(J - 1) - G]\mathbf{F}^{-T}, \quad (3.19)$$

and

$$\begin{aligned} \mathbb{L} = & G\mathbb{I} + KJ(2J - 1)\mathbf{F}^{-T} \otimes \mathbf{F}^{-T} \\ & + [KJ(J - 1) - G]\mathbb{I}^T, \end{aligned} \quad (3.20)$$

where

$$\mathbb{I}_{ijkl} = \frac{\partial F_{kl}}{\partial F_{ij}} = \delta_{ik}\delta_{jl}. \quad (3.21)$$

In this study, we assume that the 3D phononic crystal is made of silicon-based rubber (Elite Double 32:Zhermack), which is characterized by $G = 0.27$ MPa, $K = 13.41$ MPa, and density $\rho = 965 \text{ Kg m}^{-3}$ ¹⁰.

3.5 NUMERICAL PROCEDURE AND IMPLEMENTATION

In this Section, we first present the analysis performed to study the dynamic response of 3D phononic crystals of infinite size, accounting for the effect of the applied pre-

deformation. Then, we describe how we study the effect of material damping on the propagation of elastic waves.

All numerical simulations are performed using the commercial finite element package Abaqus/Standard (SIMULIA, Providence, RI). The 3D models are constructed using quadratic brick elements (element type C3D10) and the accuracy of the mesh is insured by a mesh refinement study.

3.5.1 WAVE PROPAGATION ANALYSIS IN 3D ADAPTIVE PHONONIC CRYSTALS

The analysis conducted to investigate the propagation of elastic waves in 3D deformable phononic crystals of infinite size consist of three steps: *(i)* first, the stability of the structure is investigated through a linear perturbation analysis^{43,17}; *(ii)* then, the non-linear post-buckling response of the system is simulated by using periodic boundary conditions and introducing a small imperfection on the initial geometry in the form of the critical mode¹⁷; *(iii)* finally, the propagation of small-amplitude elastic waves at a given level of deformation is investigated by solving the frequency-domain wave equation.

Focusing on step *(iii)*, we discretize the frequency-domain wave equations (3.17) using the Galerkin finite element method and obtain an algebraic eigenvalue problem in matrix form,

$$[\mathbf{K}_{(n \times n)} - \omega^2 \mathbf{M}_{(n \times n)}] \mathbf{U}_{(n \times 1)} = 0, \quad (3.22)$$

where \mathbf{K} and \mathbf{M} are the global mass and stiffness matrices, \mathbf{U} is the nodal displacement vector, and n is the total number of degrees of freedom (i.e number of nodes multiply by degrees of freedom per node).

By virtue of Bloch's theorem¹⁹, the following relationship between the displace-

ments of two nodes, A and B , periodically located on the outer faces of the unit cell is obtained

$$\mathbf{u}_A = \mathbf{u}_B \exp(i\mathbf{k} \cdot \mathbf{r}_{AB}), \quad (3.23)$$

where \mathbf{u}_A and \mathbf{u}_B denote the displacement of nodes A and B respectively, and \mathbf{r}_{AB} is the distance between the nodes A and B in the deformed configuration. Moreover, \mathbf{k} is the wave vector that can be expressed in terms of the reciprocal lattice vectors \mathbf{b}_i

$$\begin{aligned} \mathbf{b}_1 &= 2\pi \frac{\mathbf{a}_2 \times \mathbf{a}_3}{\|\mathbf{z}\|^2}, \\ \mathbf{b}_2 &= 2\pi \frac{\mathbf{a}_3 \times \mathbf{a}_1}{\|\mathbf{z}\|^2}, \\ \mathbf{b}_3 &= 2\pi \frac{\mathbf{a}_1 \times \mathbf{a}_2}{\|\mathbf{z}\|^2}, \end{aligned} \quad (3.24)$$

where \mathbf{a}_1 , \mathbf{a}_2 and \mathbf{a}_3 are the lattice vectors spanning the unit cell (see Figure 3.2) and $\mathbf{z} = \mathbf{a}_1 \cdot (\mathbf{a}_2 \times \mathbf{a}_3)$. Note that when the Bloch-type boundary conditions (3.23) are incorporated into Eq. (3.22), the stiffness matrix becomes a function of \mathbf{k} (i.e. $\mathbf{K} = \mathbf{K}(\mathbf{k})$). Therefore, to obtain the dispersion relations $\omega = \omega(\mathbf{k})$ the eigenvalue problem specified by Eq. (3.22) needs to be solved for a number of wave vectors \mathbf{k} .

Since the reciprocal lattice is also periodic, we can restrict the wave vectors \mathbf{k} to a certain region of the reciprocal space called the *first Brillouin zone* (dark grey cube in Figure 3.2(b))²³. In addition, we may further reduce the domain taking advantage of its reflectional and rotational symmetries. The reduced domain is referred to the *irreducible Brillouin zone* (IBZ) (red pyramid GXMR in Figure 3.2(b))⁸⁴.

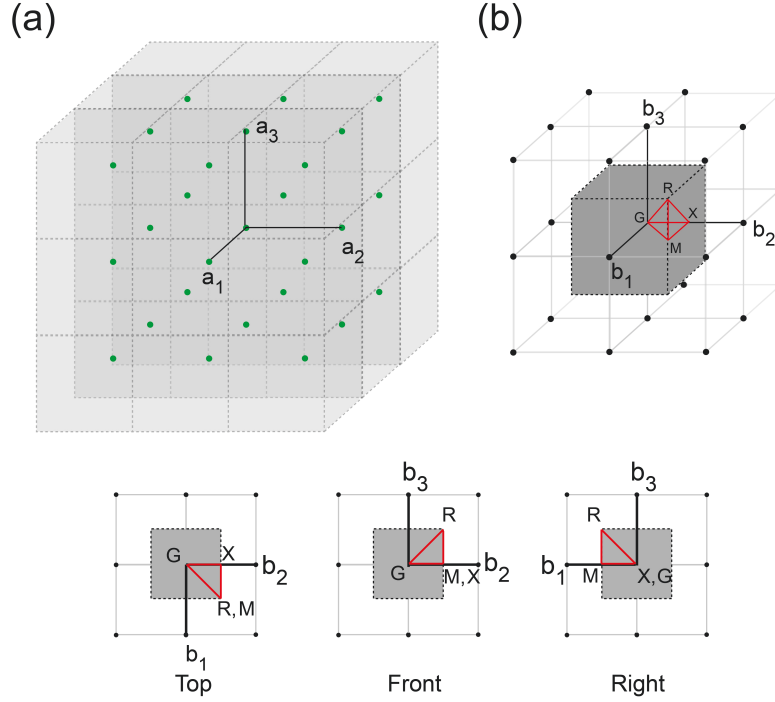


Figure 3.2: Schematic of point lattice (green dots in (a)), reciprocal lattice (black dots in (b)), first Brillouin zone (grey cube in (b)) and irreducible Brillouin zone (red pyramid GXMR in (b)). Three different views of the reciprocal lattice are shown at the bottom.

Next, we show that Eq. (3.22) can be solved using either the full direct method or the Reduced Bloch Mode Expansion (RBME) method⁵² to significantly reduce the computational cost.

FULL (DIRECT) METHOD

Here, we solve Eq. (3.22) for a large number of \mathbf{k} vectors on the perimeter of IBZ (i.e. G-X-M-G-R-M-X-R path in Figure 3.3) to obtain the dispersion relations $\omega = \omega(\mathbf{k})$. In particular, we use ten uniformly spaced \mathbf{k} -points on each edge of the IBZ shown in Figure 3.3. Given the large sizes of the mass and stiffness matrices involved in the calculations (i.e. $n \simeq 200000$ for our unit cells), this method is computationally very

expensive.

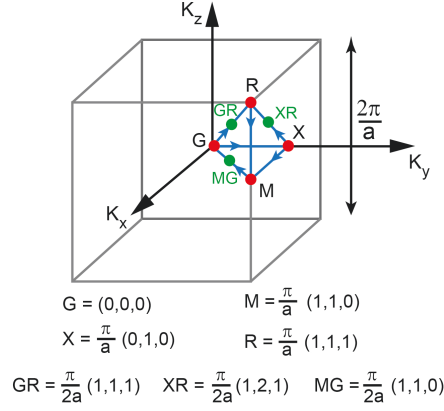


Figure 3.3: First Brillouin zone (cube of side $2\pi/a$) and irreducible Brillouin zone (IBZ) with the seven high-symmetry points used in this study: corner points (G, X, M, R) and points on mid-diagonal lines (GR, XR, MG).

REDUCED BLOCH MODE EXPANSION (RBME) METHOD

To reduce the size of the problem and consequently the computational cost, we employ a reduced basis composed of a selected set of Bloch eigenvectors⁵². To this end, we use a linear transformation given by

$$\mathbf{U}_{(n \times 1)} = \phi_{(n \times m)} \mathbf{V}_{(m \times 1)}, \quad (3.25)$$

where $\mathbf{U}_{(n \times 1)}$ is the nodal Bloch displacement vector, $\mathbf{V}_{(m \times 1)}$ is the reduced Bloch displacement vector, $\phi_{(n \times m)}$ is the transformation matrix, n is the total number of degrees of freedom, and m ($m \ll n$) is the total number of Bloch modes in the reduced basis. Combining (3.25) and (3.22), and pre-multiplying by the complex conjugate transpose $\phi_{(m \times n)}^*$, yields the eigenvalue problem in the reduced basis

$$\left[\phi_{(m \times n)}^* \mathbf{K}(\mathbf{k})_{(n \times n)} \phi_{(n \times m)} - \omega^2 \phi_{(m \times n)}^* \mathbf{M}_{(n \times n)} \phi_{(n \times m)} \right] \mathbf{V}_{(m \times 1)} = 0, \quad (3.26)$$

which can be re-express as

$$[\bar{\mathbf{K}}(\mathbf{k})_{(m \times m)} - \omega^2 \bar{\mathbf{M}}_{(m \times m)}] \mathbf{V}_{(m \times 1)} = 0, \quad m \ll n \quad (3.27)$$

where $\bar{\mathbf{K}}$ and $\bar{\mathbf{M}}$ are the reduced stiffness and mass matrices,

$$\begin{aligned} \bar{\mathbf{K}} &= \phi_{(m \times n)}^* \mathbf{K}(\mathbf{k})_{(n \times n)} \phi_{(n \times m)}, \\ \bar{\mathbf{M}} &= \phi_{(m \times n)}^* \mathbf{M}_{(n \times n)} \phi_{(n \times m)}. \end{aligned} \quad (3.28)$$

The reduced basis used in this study is composed of Bloch eigenvectors evaluated at seven high-symmetry points: points G, X, M, and R (corners of the IBZ) and GR, XR, and MG shown in Figure 3.3. The choice of these points is motivated by both the crystal structure and group theory⁵². To construct the transformation matrix $\phi_{(n \times m)}$, we solve (3.22) only at the selected seven high-symmetry points and assemble the corresponding eigenvectors in column-wise form as

$$\phi_{(n \times m)} = [\phi_G \phi_X \phi_M \phi_R \phi_{MG} \phi_{GR} \phi_{XR}]. \quad (3.29)$$

Furthermore, since in this study we are interested in computing the first 160 dispersion branches, we find that 800 eigenmodes calculated at each of the seven high-symmetry points are sufficient for the band structure calculations to be accurate up to range of interest. The accuracy of the band structure calculated by employing the RBME method with seven high-symmetry points were assured by reproducing the

same band diagrams calculated via the full (direct) method, as shown in Figure 3.4 for a 3D phononic crystal characterized by $(\alpha, \tau) = (0.03, 0.2)$. Note that, when using the RBME method, the size of the mass and stiffness matrices is reduced from $n \simeq 200000$ to $m = 5600$, significantly reducing the computational cost.

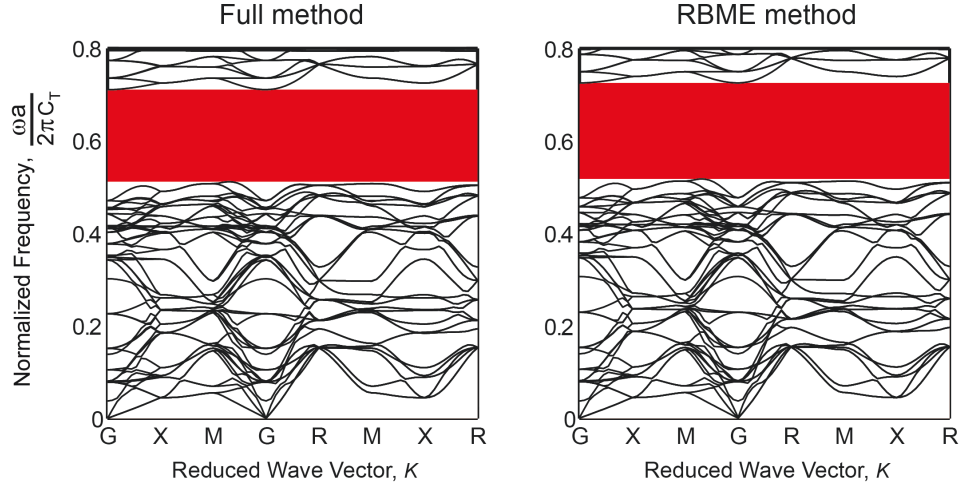


Figure 3.4: Band diagrams for a 3D phononic crystal characterized by $(\alpha, \tau) = (0.03, 0.2)$ calculated using full (direct) method (left) and the RBME method (right).

3.5.2 WAVE PROPAGATION ANALYSIS IN 3D DAMPED PHONONIC CRYSTALS

To study the effect of material dissipation on the propagation of elastic waves, we employ Rayleigh (proportional) damping model^{27,111} and define a damping matrix \mathbf{C} linearly proportional to the mass and stiffness matrices \mathbf{M} and $\mathbf{K}(\mathbf{k})$,

$$\mathbf{C}(\mathbf{k}) = p\mathbf{M} + q\mathbf{K}(\mathbf{k}), \quad (3.30)$$

where p and q are the mass and stiffness proportional damping coefficients ($p, q \geq 0$). The discretized finite element frequency-domain wave equations of the damped

phononic crystal are then given by

$$[\mathbf{K}(\mathbf{k}) + i\omega \mathbf{C}(\mathbf{k}) - \omega^2 \mathbf{M}] \mathbf{U} = 0, \quad (3.31)$$

and the wave-vector-dependent damping ratio $\xi_i(\mathbf{k})$ for the i -th branch of the damped band structure is obtained as¹⁴²

$$\xi_i(\mathbf{k}) = \frac{p + q\omega_i^2(\mathbf{k})}{2\omega_i(\mathbf{k})}, \quad (3.32)$$

where $\omega_i(\mathbf{k})$ denotes the i -th frequency obtained in the absence of damping. Since for underdamped conditions (i.e. $\xi_i < 1$), the effect of the damping parameter p in Eq. (3.30) is negligible^{54,53}, we consider a stiffness-proportional Raleigh damping matrix (i.e. $p = 0$ and $q \neq 0$) in all the calculations and report all results in terms of the dimensionless damping coefficient $\bar{q} = q c_T / a$. We also note that for elastomers $\xi_i = q\omega_i/2 = \pi\bar{q}\bar{f} \sim 0.05$ ^{60,4,37}, so that if we focus on the upper limit of the bandgap (i.e. $\bar{f}_{upper} \sim 0.75$) we obtain $\bar{q} \sim 0.02$ for elastomeric materials.

To investigate the propagation of elastic waves in a dissipative medium, we construct 3D models of finite size comprising different numbers of unit cells and calculate their steady-state dynamic linearized response to harmonic excitations for different levels of material damping. In this set of analyses we account for energy dissipation by directly introducing Raleigh damping in the simulations (i.e. the *DAMPING keyword is used to specify Raleigh damping parameters as material properties in Abaqus/Standard²). Moreover, we excite the structure by applying an harmonic displacement ($A_{in} \cos(\omega t)$) to the central node of one of its faces at one end and calculate the displacement of the corresponding node on the opposite face at the other

end ($A_{out} \cos(\omega t)$) over the frequency ranges of interest. The transmission spectrum (dB) is then computed as $10 \log (A_{out}(\omega)/A_{in}(\omega))^2$.

3.6 RESULTS

3.6.1 ELASTIC WAVES PROPAGATION IN THE UNDEFORMED PHONONIC CRYSTAL

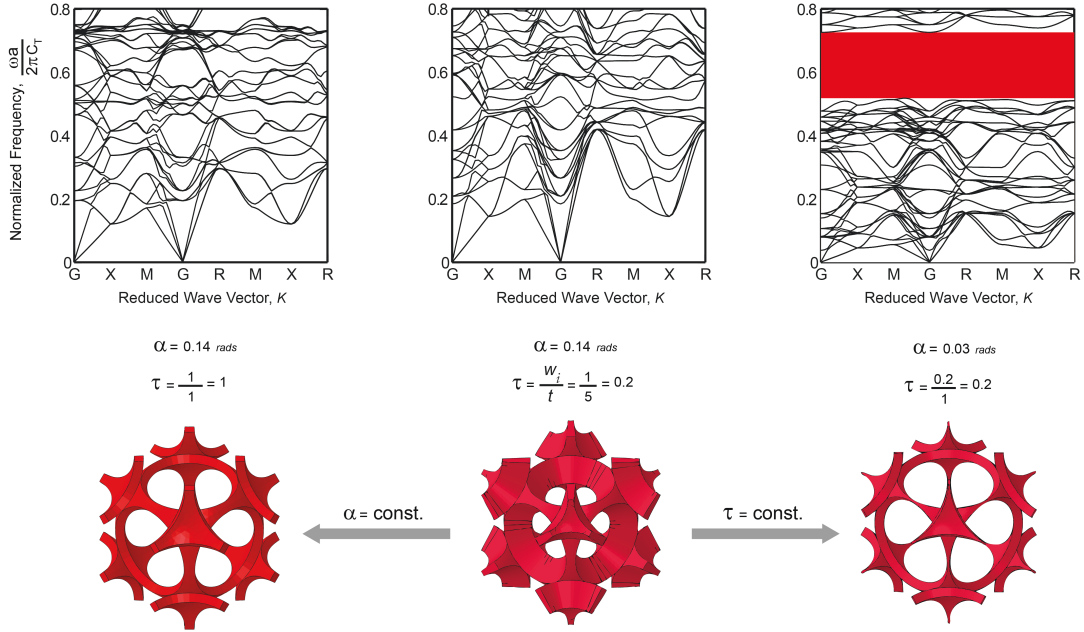


Figure 3.5: Effect of design parameters α and τ on the band structures. In the dispersion relation plots, the non-dimensional frequency $\bar{f} = \omega a / 2\pi c_T$ is plotted versus the wave vectors \mathbf{k} . Three different configurations are considered characterized by $(\alpha, \tau) = (0.14, 0.2)$ (center), $(0.14, 1.0)$ (left) and $(0.03, 0.2)$ (right). The shaded red region in the right plot highlights the bandgap - i.e. ranges of frequencies for which the elastic waves are not allowed to propagate along any direction.

We start by investigating the propagation of elastic waves in undeformed phononic crystals of infinite size. In Figure 3.5 we report the band diagram for crystals characterized by $(\alpha, \tau) = (0.14, 0.2)$, $(0.14, 1.0)$ and $(0.03, 0.2)$. In all these diagrams the non-dimensional frequency $\bar{f} = \omega a / (2\pi c_T)$ is plotted versus a set of wave vectors \mathbf{k} spanning the perimeter of the IBZ shown in Figure 3.3. Here, $c_T = \sqrt{G/\rho}$ is the speed of transverse elastic waves propagating within the homogeneous bulk material and a is the characteristic size of the unit cell in the undeformed configuration (see Figure 3.1). As expected, we find that the microstructural design parameters α and τ strongly affect the existence and width of the bandgap. In fact, while the 3D phononic crystals with $(\alpha, \tau) = (0.14, 0.2)$ and $(0.14, 1.0)$ have no frequency ranges of strong wave attenuation, the structure with $(\alpha, \tau) = (0.03, 0.2)$ has a bandgap for $\bar{f} = 0.52 - 0.72$. It is important to note that this is a Bragg-type bandgap, since it is very sensitive to the periodicity and geometry of the crystal. To demonstrate this, in Figure 3.6 we report the band structure for a phononic crystal characterized exactly by the same design parameters (i.e. $(\alpha, \tau) = (0.03, 0.2)$), but with the structured shells arranged differently and attached to each other through the thin ligaments rather than through the corners (see Figure 3.6). For this periodic structure no bandgap is found.

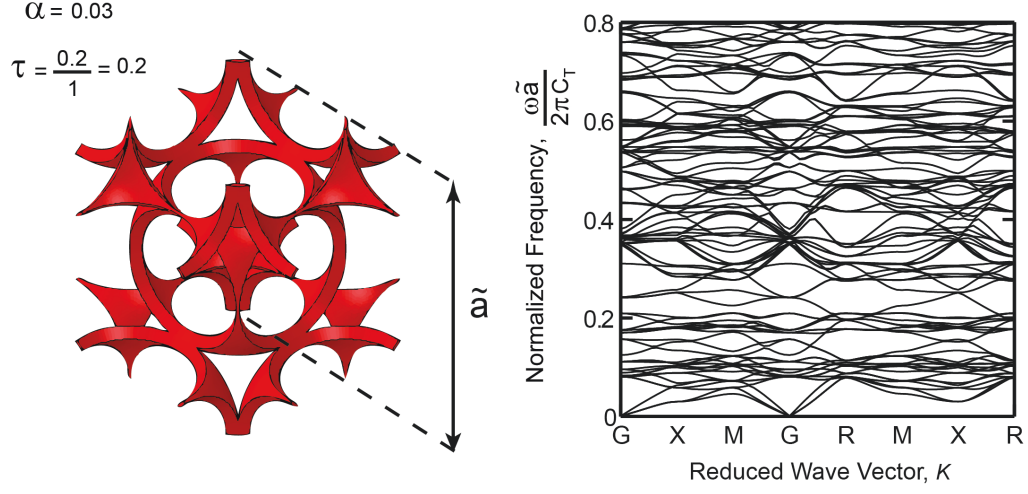


Figure 3.6: Bands diagram for a phononic crystal composed of a *bcc* array of structured shells attached to the neighbors through the ligaments. The structured shells are characterized by $(\alpha, \tau) = (0.03, 0.2)$. Note that these are the same design parameters that we used to construct the phononic crystal shown in Figure 3.5-right. $\tilde{a} = 4r_o/\sqrt{2}$ is the characteristic length of the unit cell.

Next, we systematically study the effect of the design parameters α and τ on the propagation of elastic waves. Since the phononic bandgaps are strongly influenced by the smallest geometric features in the system⁷⁶, a bandgap opens when α is decreased below a critical threshold. The effect of τ on the bandgap is instead more unpredictable, since a smaller values of τ results in a structure characterized by thinner ligaments width w_i , but larger thickness t . Therefore, to identify the 3D crystal with the widest phononic bad gap in the undeformed configuration, we choose $\alpha = 0.03$ and conduct a parametric study to explore the influence of τ . In Figure 3.7(a) we show the evolution of the bandgap as a function of τ . The results clearly indicate that the the width of the bandgap does not monotonically increase as a function of τ and the largest bandgap is achieved for $\tau = 0.4$ (see Figure 3.7(b,c)).

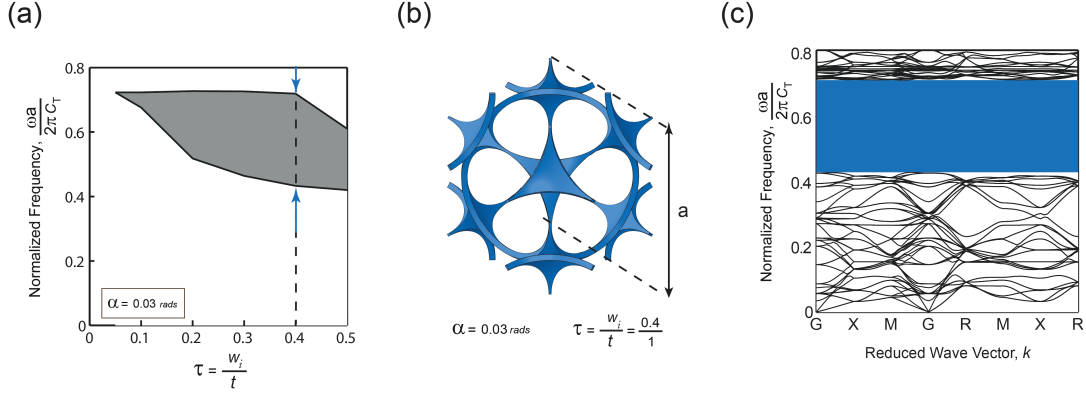


Figure 3.7: Design of an optimal 3D phononic crystal in the undeformed configuration. (a) Evolution of the bandgap as a function of τ for a 3D crystal with $\alpha = 0.03$. The structure exhibits the widest phononic bandgap for $\tau = 0.4$ and is demonstrated in (b). (c) Bands diagram for the optimal crystal characterized by $(\alpha, \tau) = (0.03, 0.4)$. The 3D structure exhibits a wide bandgap at $\bar{f} = 0.43 - 0.72$.

3.6.2 EFFECT OF DEFORMATION ON WAVE PROPAGATION

Having identified the optimal configuration in the undeformed configuration, we now proceed to explore the propagation of small-amplitude elastic waves in such 3D crystal at different levels of applied deformation. Here, to preserve the symmetry of the structure and facilitate the calculation of the band diagram, we compress the 3D crystal triaxially. First, we perform a linear stability analysis and find that for $\tau = 0.4$ buckling induces the spherical collapse of every building block while keeping the structure periodic (see Figure 3.1). Then, we simulate the post-buckling response of the structure by introducing a small imperfection in the initial geometry and monitor the propagation of small amplitude elastic waves as a function of the applied deformation. In Figure 3.8 we report the evolution of bandgap as a function of the applied compressive strain, ϵ . The results clearly indicate that the applied compression significantly alters the bandgaps, by progressively reducing its width. In fact,

while in the undeformed configuration the structure is characterized by a bandgap for $\bar{f} = 0.43 - 0.72$, for $\epsilon = -0.10$ its width is reduced to $\bar{f} = 0.41 - 0.46$. Finally, for $\epsilon = -0.16$, the bandgap completely disappears, so that elastic waves of all frequencies are able to propagate within the structure. Therefore, our results clearly demonstrate that the proposed 3D structure acts as a reversible phononic switch, since a moderate level of strain (i.e. $\epsilon = -0.16$) can be used to switch off the bandgap.

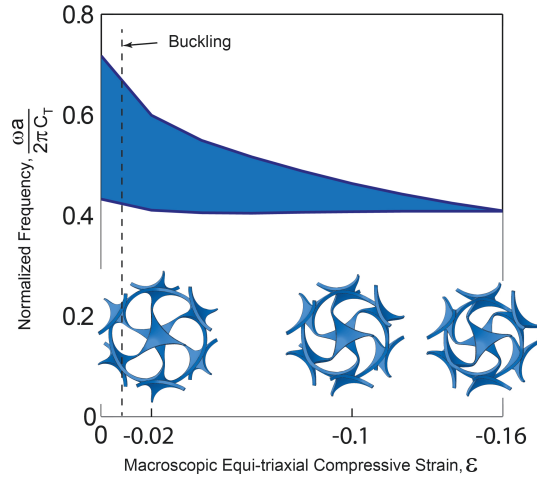


Figure 3.8: Evolution of bandgap as a function of the applied compressive strain for a 3D crystal characterized by $(\alpha, \tau) = (0.03, 0.4)$. Note that buckling occurs at $\epsilon = -0.007$.

3.6.3 DAMPED PHONONIC CRYSTAL

Our results indicate that mechanical instabilities and large deformation can be effectively utilized to reversibly tune and control the phononic bandgaps of 3D periodic structures. However, in order for the structure to sustain the large deformation induced by buckling while remaining in the fully elastic regime, elastomeric materials such as silicon rubber are typically used for fabrication. These materials are known

to be dissipative and so we now investigate the effect of material damping on the dynamic response of 3D crystals.

To investigate the effect of material damping on the propagation of small-amplitude elastic waves, we start by constructing phononic crystals with 4, 10, 20 and 40 unit cells along the x-direction (indicated in Figure 3.1) and periodic boundary conditions on the lateral faces. In Figure 3.9, we report the transmission spectra for such structures characterized by $(\alpha, \tau) = (0.03, 0.4)$ and consider three different stiffness-proportional damping coefficients ($\bar{q} = 0, 0.005, 0.02$).

Focusing on the undamped crystals ($\bar{q} = 0$ - red lines), we find a good agreement between the drop in transmission observed in the four models (dashed horizontal red line) and the bandgap-size predicted by the Bloch wave analysis for the corresponding infinite structure (solid horizontal red line). Moreover, as expected, we find that the agreement is improved and the amount of drop in transmission is more pronounced for larger structures (i.e. ~ -15 dB for the model with 4 unit cells in Figure 3.9(a) and ~ -25 dB for the model with 40 unit cells in Figure 3.9(d)).

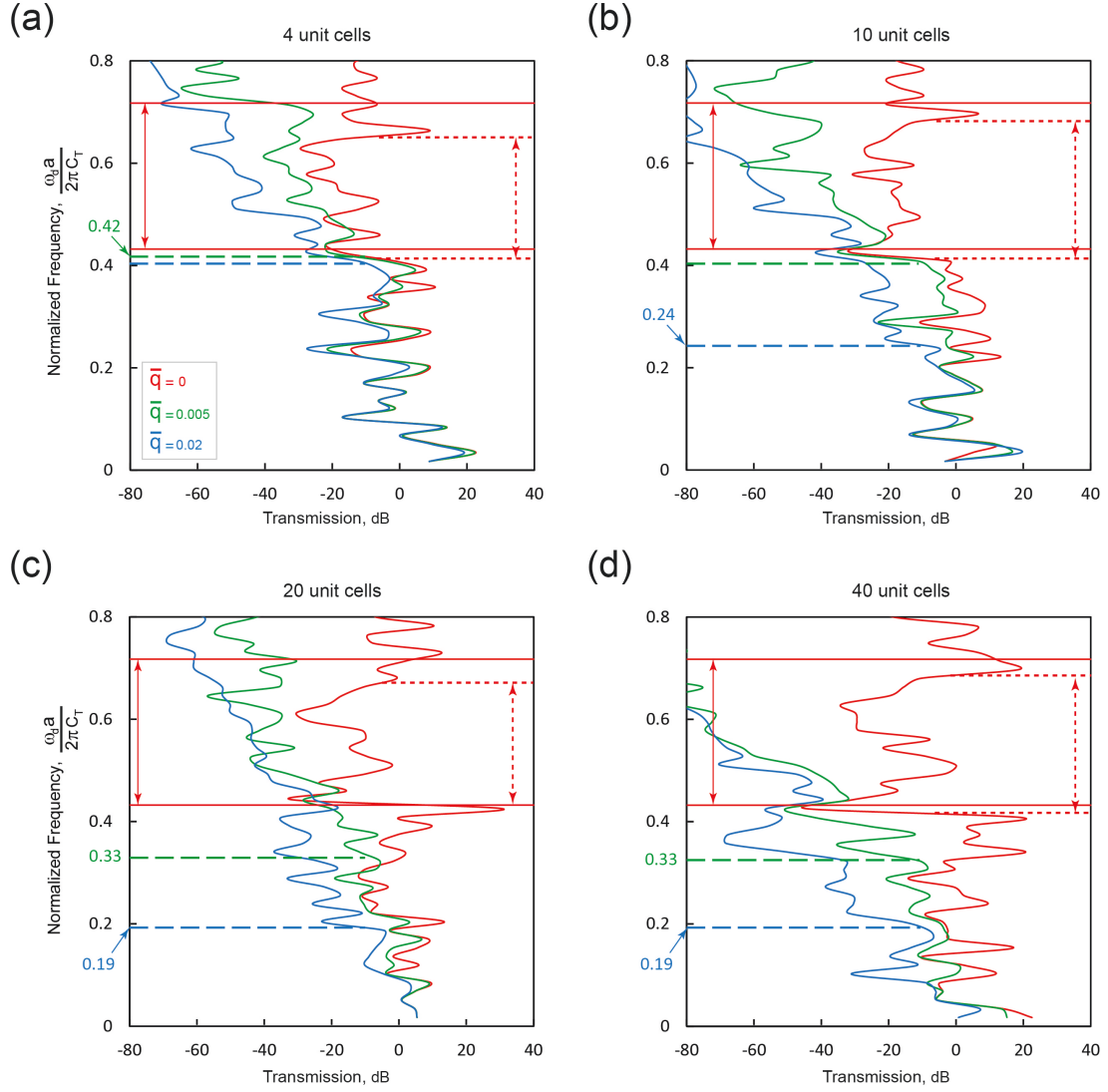


Figure 3.9: Effect of damping on the transmission spectra for models consist of (a) 4, (b) 10, (c) 20, and (d) 40 unit cells along the x-direction and periodic boundary conditions on the lateral faces. The solid horizontal red lines represent the bandgap predictions for the corresponding undamped infinite periodic structures. The horizontal dashed red lines highlight regions with a relative -15 dB drop in transmission. Note that for $\bar{q} = 0.005$ and 0.02, the transmission decays above a cut-off frequency.

Furthermore, our results reveal that material damping has a significant effect on the transmission spectrum and that all waves with frequencies above a cutoff value

are damped. To quantify this effect, the cutoff frequency, denoted by \bar{f}_{cutoff} , is defined as the critical frequency above which all waves are attenuated by at least 10 dB. Such cutoff frequencies are indicated by the green and blue horizontal dashed lines in Figure 3.9. The transmission response continues to decay for frequencies higher than \bar{f}_{cutoff} . Interestingly, we see that by increasing the size of the structure, the cutoff frequencies are progressively lowered. In fact, in a larger structure the wave travels through a longer medium, so that the effect of dissipative medium on transmission spectrum is more pronounced for the same level of damping. However, we note that the cutoff frequencies are the same for the model with 20 and 40 unit cells along the x-direction ($\bar{f}_{cutoff} \sim 0.33$ for $\bar{q} = 0.005$ and $\bar{f}_{cutoff} \sim 0.19$ for $\bar{q} = 0.02$), indicating that these structures are large enough so that the dynamic response is not anymore affected by the size of the system.

Finally, in Figure 3.10 we report results for a finite size structure with $4 \times 4 \times 4$ unit cells. We find that the bandgap for the undamped case (i.e. $\bar{q} = 0$ - red curve) is relatively smaller than that of the corresponding infinite crystal, indicating that the finite size of the structure significantly affect its dynamic response. Moreover, we note that as we increase \bar{q} , material dissipation has still a significant effect, but not as pronounced as for the systems investigated in Figure 3.9. In fact, we find that for $\bar{q} = 0.005$ the structure is still characterized by a bandgap, highlighted by the drop in transmission at $\bar{f} = 0.51 - 0.63$. However, for $\bar{q} = 0.02$ the response is characterized by cutoff frequency and the propagation of waves with $\bar{f} > 0.5$ is prevented by the dissipative medium. Therefore, these results highlight the important role played by the size of the system in the case of a damped phononic crystal.

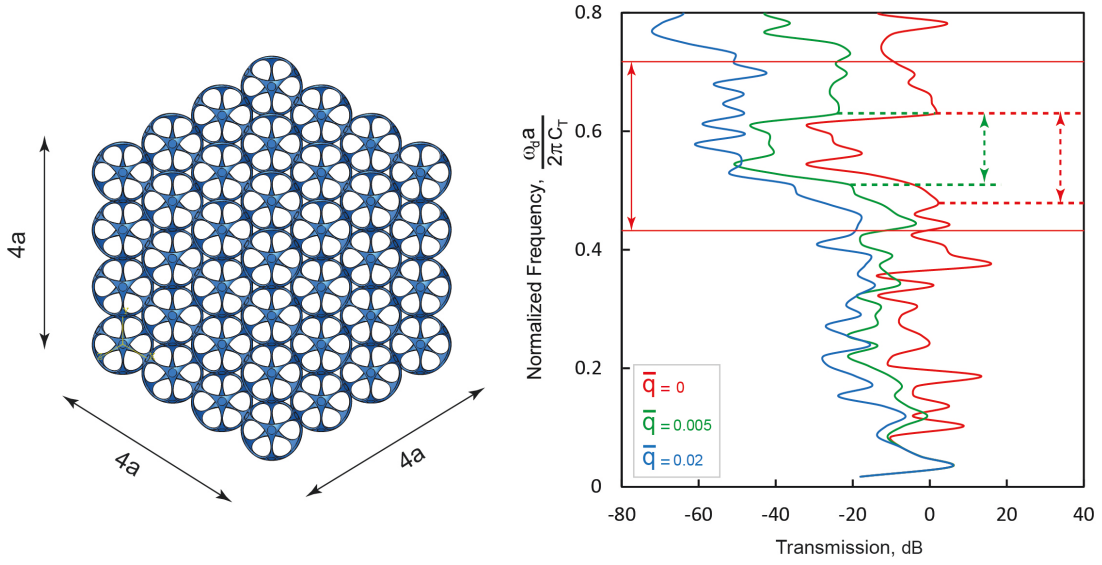


Figure 3.10: Effect of damping on the propagation of elastic waves in a finite size structure consists of $4 \times 4 \times 4$ structured shells. The solid horizontal lines indicate the bandgaps prediction based on calculations for the infinite undamped structure, while the dashed horizontal lines highlight regions in which a relative -15 dB drop is observed in the transmission.

3.7 CONCLUSIONS

In conclusion, our study outlines a general strategy in which a judicious choice of building blocks provides a foundation for the design of 3D phononic crystals whose response can be effectively tuned by the applied deformation, opening the door to the design of 3D phononic switches. In particular, we show that the tunability of bandgaps can be significantly increased by exploiting the geometric nonlinearity triggered by instabilities. Moreover, we investigate the effects of energy dissipation induced by elastomeric materials on the dynamic response of 3D phononic crystals. Our results indicate that the propagation of waves in structures made of dissipative media is affected by both the amount of damping and the size of the system, providing a complete set of guidelines for the design of 3D adaptive phononic crystals.

Finally, since the buckling phenomenon is scale-independent and the elastic deformation process is fully reversible, we expect our results will serve as a blueprint for the design of a new class of tunable phononic devices in a wide range of applications.

This chapter has already been published in:

S. Babae, N. Viard, N. Fang, and K. Bertoldi, Harnessing Deformation to Switch On and Off the Propagation of Sound, *Advanced Materials* 2016, 28 (8):1631-1635.

4

Harnessing Deformation to Switch On and Off the Propagation of Sound

4.1 OVERVIEW

By combining numerical analyses and experiments we design a new class of architected materials to control the propagation of sound (also called acoustic metamaterials). The proposed system comprises an array of elastomeric helices in background air and is characterized by frequency ranges of strong wave attenuation (bandgaps) in the undeformed configuration. Importantly, our results indicate that by axially stretching the helices such bandgaps can be suppressed, enabling the propagation of sound over all frequencies. The proposed concept expands the ability of existing acoustic metamaterials and paves the way for the design of a new class of materials and devices that enable better control and manipulation of sound.

4.2 INTRODUCTION

Architected materials engineered to manipulate and control the propagation of sound have recently enabled the design of a range of novel acoustic devices^{165,72,83,38,80,128,30,29,119}. In particular, the design of noise cancelling systems that take advantage of bandgaps induced by both Bragg scattering^{79,140,117} and local resonance^{81,91,73,13,158} has been aggressively pursued. However, almost all of the proposed designs operate in fixed ranges of frequencies and their response cannot be tuned after their fabrication⁹⁰. In an effort to design the next generation of acoustic tunable devices, it has been shown that the frequency range of the bandgap can be modulated through applied mechanical deformation⁵⁰, thermal radiation¹⁴⁶, and rotation of the scatters^{45,113,152,71,74}. However, differently from the case of metamaterials designed to control the propagation of elastic^{5,15,41,20,114,150,12,148} and electromagnetic^{68,86,78} waves for which several strategies have been used to switch on and off the bandgaps, the ability to turn on

and off the propagation of sound over a specific ranges of frequencies has not been extensively explored, and it has only been demonstrated through the rotation of the scatters^{45,152}.

Here, we report a new class of acoustic metamaterials in which the applied deformation is exploited to switch on and off the propagation of sound over specific ranges of frequencies. The proposed structure comprises an array of elastomeric helices that can be easily stretched in axial direction (see Figure 4.1). In the undeformed configuration the helices are in a compact state (see Figure 4.1a) and the system is equivalent to a square array of solid cylinders in air, which is known to be characterized by a complete bandgap induced by Bragg scattering¹¹⁸. However, as the metamaterial is deformed, the pitch of the helices increases (see Figure 4.1b) and the air originally inside their internal cavity connects to the surrounding fluid, significantly reducing the solid volume fraction of the system. Importantly, we demonstrate that this change in volume fraction induced by the applied deformation is sufficient to suppress the initial bandgap, giving us the opportunity to design a new class of acoustic switches.

4.3 RESULTS AND DISCUSSION

We start by investigating the deformation of a single elastomeric helix. The helix is fabricated out of a silicone-based rubber¹⁰ (Vinyl Polysiloxane with initial Young's modulus $E_0 = 784 \text{ kPa}$, Poisson's ratio $\nu_0 = 0.499$, and density $\rho = 965 \text{ kg/m}^3$) via a molding approach (see Supporting Information for details). In the undeformed configuration it has diameter $D_0 = 28.6 \text{ mm}$, pitch $P_0 = 13 \text{ mm}$, and a rectangular cross-section of $13 \text{ mm} \times 6.5 \text{ mm}$. In Figure 4.2a we report experimental snapshots of a single helix at different levels of applied engineering strain, $\epsilon = (H - H_0)/H_0 =$

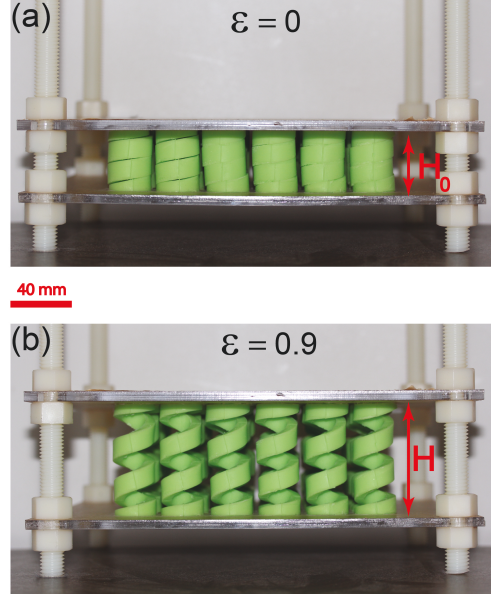


Figure 4.1: Acoustic switch. The fabricated acoustic switch comprises a 6×6 square array of stretchable helices. In the undeformed configuration (i.e. $\epsilon = 0.0$), the helices are in a compact state and can be regarded as solid cylinders of height $H_0 = 40 \text{ mm}$. As a result, the metamaterial is characterized by a frequency range of strong wave attenuation (bandgap). As the helices are stretched, the solid volume fraction of the metamaterial drops significantly and the bandgap is suppressed.

0, 0.40, 0.65, and 0.90, where H_0 and H denote the undeformed and deformed height of the helix, respectively. The experimental images are compared to the numerical snapshots obtained from non-linear Finite Element (FE) simulations (see Supporting Information for details) and clearly show that the pitch of the helix monotonically increases with the applied strain (note that the pitch varies along the the length of the helix because of gravity), while its diameter remains almost unchanged. This can be explained by inspecting the parametric equations that describe the deformed helix,

$$\mathbf{r}(\theta) = \left(\frac{D}{2} \cos \theta, \frac{D}{2} \sin \theta, \frac{P}{2\pi} \theta \right), \quad (4.1)$$

where the deformed pitch, P , and diameter, D , are given by (see Supporting Information for more details)

$$P = P_0(1 + \epsilon), \quad D = \sqrt{D_0^2 - \frac{P_0^2}{\pi^2} \epsilon(2 + \epsilon)}. \quad (4.2)$$

In Figures 4.2b and 4.2c we report the evolution of P and D as a function of the applied strain ϵ , as predicted by Eq. (4.2) (red dashed lines). The analytical results indicate that, while the change in diameter is limited to 3% for $\epsilon = 0.9$, the pitch length almost doubles (i.e., $P/P_0 = 1.9$ at $\epsilon = 0.9$). Finally, we note that in Figures 4.2b and 4.2c the analytical predictions are also compared to the experimental (green markers) and FE (blue markers) results, showing an excellent agreement and therefore validating our simple geometric model.

Focusing on a metamaterial comprising a square array of helices with center-to-center distance $A_0 = 32.5$ mm, it is easy to see that the large change in pitch induced by the applied strain, significantly alters the solid volume fraction of the system. In fact, since here we focus on acoustic waves propagating in the air surrounding the helices, in the undeformed configuration each helix can be considered as a solid cylinder and the solid volume fraction of the metamaterial can be calculated as $\psi_0 = \pi D_0^2 / (4A_0^2) = 0.61$. However, as the metamaterial is stretched, the cylinders transform into helices and the air originally inside their internal cavity connects to the surrounding fluid, reducing the solid volume fraction. In particular, for $\epsilon > 0$ the solid volume fraction can be simply obtained as (see Supporting Information for details)

$$\psi = \frac{\pi(D_0^2 - D_{0,in}^2)}{4A_0^2(\epsilon + 1)}, \quad (4.3)$$

where $D_{0,in} = 15.6$ mm denotes the inner diameter of the helices and we have made

use of the fact that the volume of the elastomeric helices is preserved during deformation. In Figure 4.2d we report the evolution of ψ as a function of ϵ . The results indicate that at first, as the helices are slightly stretched, ψ immediately reduces from 0.61 to 0.41 and then gradually decreases to reach 0.22 as ϵ rises to 0.9. Importantly, we expect this change in ψ to have a profound impact on the propagation of sound, as it is well known that the size of the acoustic bandgap for an acoustic metamaterial significantly depends on the solid volume fraction⁸⁵.

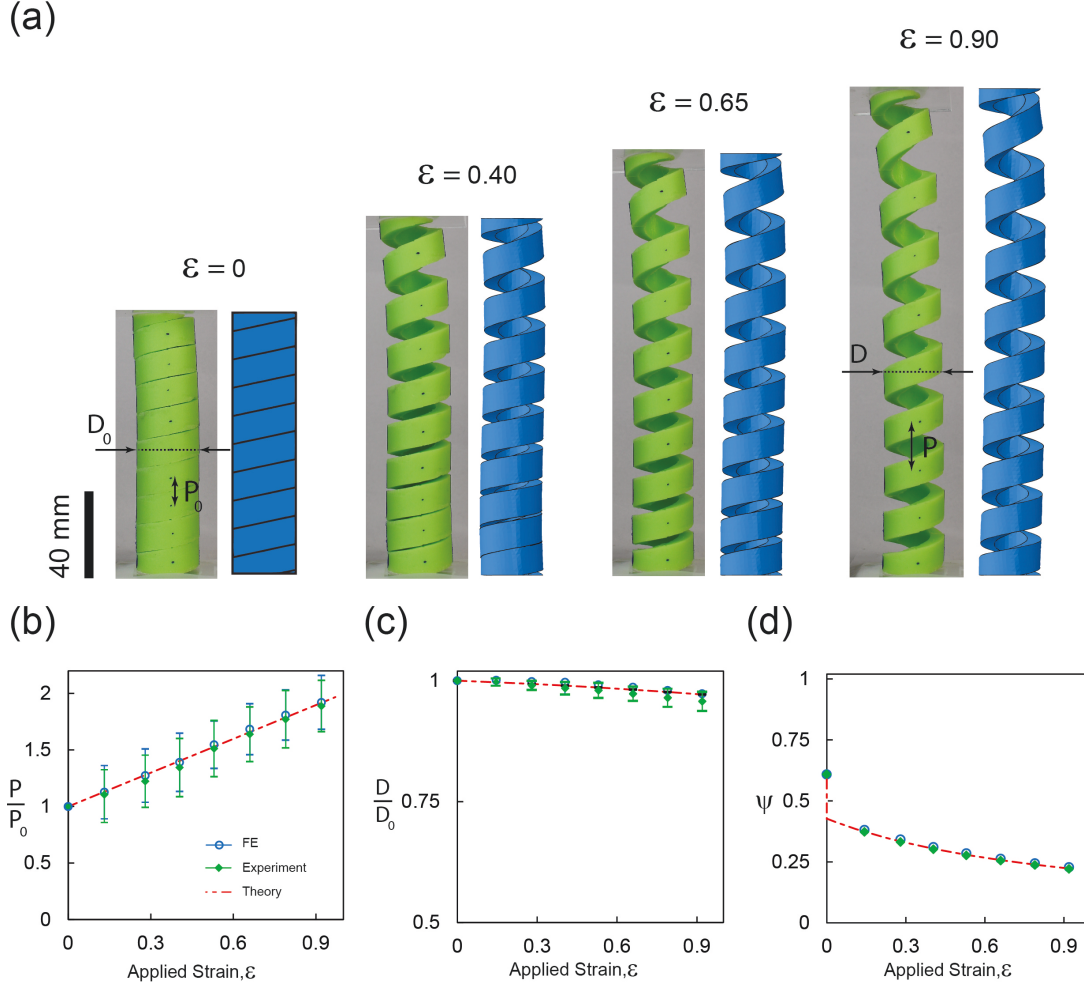


Figure 4.2: Deformation of the helices. (a) Experimental (green samples) and numerical (blue models) images of a single helix at different levels of applied strain, $\epsilon = 0, 0.40, 0.65$, and 0.90 . P_0 and D_0 are the pitch length and outer diameter of the helix at $\epsilon = 0$. (b-d) Evolution of (b) pitch length, P , (c) outer diameter, D , and (d) solid volume fraction, ψ , as a function of the applied strain. Analytical predictions (red dashed line) are compared to both experimental (green markers) and numerical (blue markers) results.

Next, we investigate numerically the propagation of sound waves through the acoustic metamaterial at different levels of applied deformation. For this set of simulations we assume the metamaterial to be infinite and use a prismatic unit cell of size $A_0 \times A_0 \times P_0$ in the undeformed configuration. The analysis consists of two steps:

(i) we first build a 3D model of the helix (comprising only one loop), mesh it using solid element (Abaqus element type C3D10M with seed size of 1 mm), apply periodic boundary conditions along the axial direction and deform it by applying a strain ϵ ;

(ii) we then change the elements of the deformed helix into acoustic elements (Abaqus element type AC3D10M), mesh also the surrounding air in the unit cell using the same type of elements (for the air we assume density $\rho_{air} = 1.2 \text{ kg/m}^3$ and speed of sound $c_{air} = 343 \text{ m/s}$) and finally calculate the dispersion relation by using frequency domain analyses (see Supporting Information for more details). Note that, since in this study we only focus on waves propagating in the plane perpendicular to the axis of the helices, the dispersion diagrams are constructed considering wave vectors lying in that plane.

In Figures 4.3a and 3b we show the dispersion relations calculated for the undeformed ($\epsilon = 0$, Figure 4.3a) and highly deformed ($\epsilon = 0.9$, Figure 4.3b) metamaterial. At $\epsilon = 0$, a wide complete bandgap is found at $f = 4.64 - 7.28 \text{ kHz}$ (highlighted by the blue area in Figure 4.3a), so that we expect sound waves within this frequency range not to propagate through the system. However, as the deformation is progressively increased, this band gap is found to monotonically reduce its width (see Figures ?? and ??), and at $\epsilon = 0.9$ it is fully closed (Figure 4.3b).

To confirm the numerical predictions, we experimentally test the dynamic response in GX direction of an acoustic metamaterial consisting of 36 stretchable helices arranged in a 6×6 square lattice with center-to-center distance $A_0 = 32.5 \text{ mm}$. In order to stretch all the helices simultaneously and to immobilize them at the strain level of interest, we use a fixture made of acrylic plates and nylon bolts/nuts (see Figure 4.1). Moreover, a 2 inch-thick closed-cell foams is placed all around the sample to acoustically insulate from the spurious reflections and create homogeneous boundaries

all around the sample (see Figure B.2). Acoustic waves through air are then excited by an array of five identical loudspeakers (Vifa OT19NC00-04, 3/4 inch diameter) placed along one of the faces of the sample and the amplitude of the scattered pressure waves is recorded by a PCB microphone and pre-amplifier (model 378B02, PCB) mounted on the opposite face. Note that the propagation of sound in air through the acrylic plates surrounded by foams without the helices is also recorded and that, to reduce the effect of boundaries, the normalized transmission spectrum is computed as $20 \log_{10} \|\hat{\phi}(f)/\hat{\phi}_{air}(f)\|$, where $\hat{\phi}(f)$ and $\hat{\phi}_{air}(f)$ are the Fourier transforms of the transmission through the sample and air, respectively (see Supporting Information for details). Finally, it is important to point out that, in order to minimize the effect of sound waves propagating along the axial direction of the helices and to better approximate the conditions considered in our numerical simulations (where we only take into account waves propagating in the plane perpendicular to the axis of the helices), the initial height of the metamaterial ($H_0 = 40 \text{ mm}$) is chosen to be approximately equal to the minimum wavelength of excitation during the experiment (38 mm at 9 kHz).

The transmission spectra of sound waves through the sample, measured at $\epsilon = 0$ and 0.9 are reported as green lines in Figures 4.3c and 4.3d, respectively. In the undeformed configuration, we find that the transmission is characterized by a drop of $\sim 30 \text{ dB}$ for $f = 2.75 - 7.40 \text{ kHz}$ (Figure 4.3c), in close agreement with the numerical results for the corresponding infinite structure. In fact, the dispersion relation for the undeformed system reported in Figure 4.3a not only indicate the presence of a complete (i.e. for all directions) bandgap for $f = 4.64 - 7.28 \text{ kHz}$, but also show that in GX direction the frequency range of strong wave attenuation is significantly wider ($f = 2.90 - 7.28 \text{ kHz}$). Differently, for $\epsilon = 0.9$ the acoustic waves with frequency in the range $f = 2.75 - 7.40 \text{ kHz}$ are found to propagate through the material (i.e. the

transmission fluctuate around 0 for this range of frequency - see Figure 4.3d), confirming that the proposed metamaterial can be utilized as an acoustic switch whose response is controlled by the applied deformation. Finally, we also note that in the highly stretched structure ($\epsilon = 0.9$) a drop of ~ 20 dB in transmission is found at $f = 8 - 9$ KHz (Figure 4.3d), in correspondence of the bandgap in GX direction at $f = 7.55 - 9.00$ kHz observed in the corresponding dispersion relation (see Figure 4.3b).

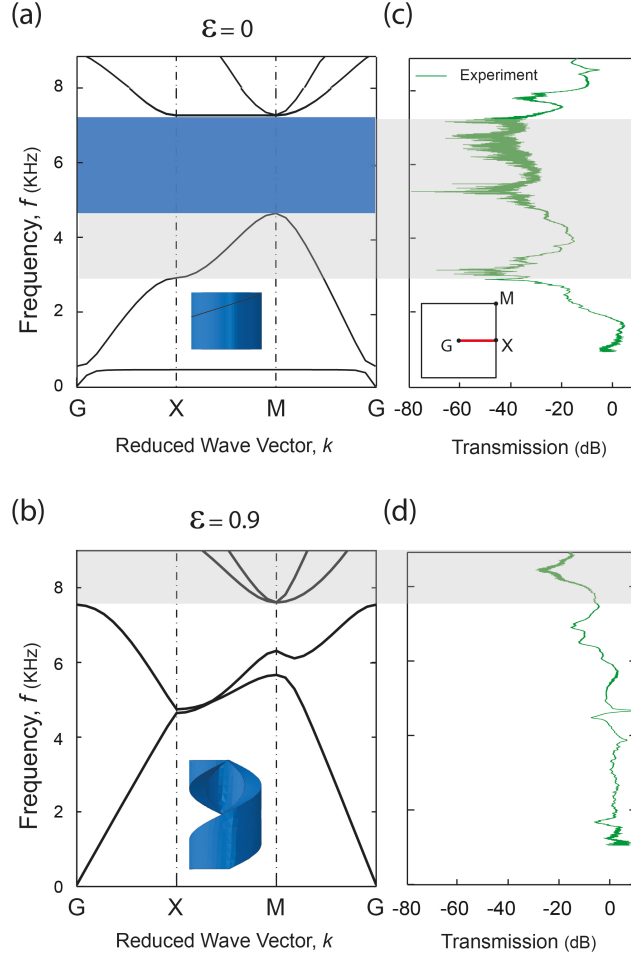


Figure 4.3: Propagation of sound through the metamaterial at different levels of applied deformation. (a,b) Dispersion relations, and (c,d) experimentally measured transmission spectra for acoustic waves propagating along the GX direction. Results are shown for (a,c) the undeformed configuration ($\epsilon = 0$), and (b,d) the stretched configuration ($\epsilon = 0.9$).

Having demonstrated that the applied deformation can be exploited to design acoustic switches, we now show that the response of the system is robust. To this end, we investigate numerically the effect of both arrangement of the helices and their geometry on propagation of sound. In Figure 4.4a we report the evolution of the bandgap frequencies as a function of the applied strain for a triangular arrangement of the

helices with the same geometry as those shown in Figure 4.1 (i.e., $D_0 = 28.6\text{ mm}$, $P_0 = 13\text{ mm}$ and rectangular cross-section of $13\text{ mm} \times 6.5\text{ mm}$). For a triangular array with center-to-center distance $A_0 = 32.5\text{ mm}$, we find a complete band gap at $f = 9.0 - 10.5\text{ kHz}$ in the undeformed configuration ($\epsilon = 0.0$). Importantly, this gap can be completely suppressed by stretching the system by $\epsilon = 1.3$ (see Figure B.5 for details). We also note that the discontinuity of the bandgap frequency found at small values of applied strain (i.e. $\epsilon \rightarrow 0$) is due to the sudden drop in solid volume fraction (from 0.70 to 0.49) that takes place when the metamaterial is slightly stretched. Furthermore, in Figure 4.4b we report the evolution of the bandgap as a function of the applied strain for a metamaterial comprising helices arranged on a square lattice (with lattice spacing $A_0 = 50\text{ mm}$), but characterized by a different set of geometric parameters ($D_0 = 48\text{ mm}$, $P_0 = 24\text{ mm}$ and a rectangular cross-section of $24\text{ mm} \times 2\text{ mm}$). In this case, multiple gaps are found in the undeformed configuration and all of them are sequentially suppressed by stretching the structure up to $\epsilon = 0.45, 1.1$, and 1.5 (see Figure B.6 for details). Therefore, these results demonstrate that we have identified an efficient and robust strategy to switch on and off the propagation of sound.

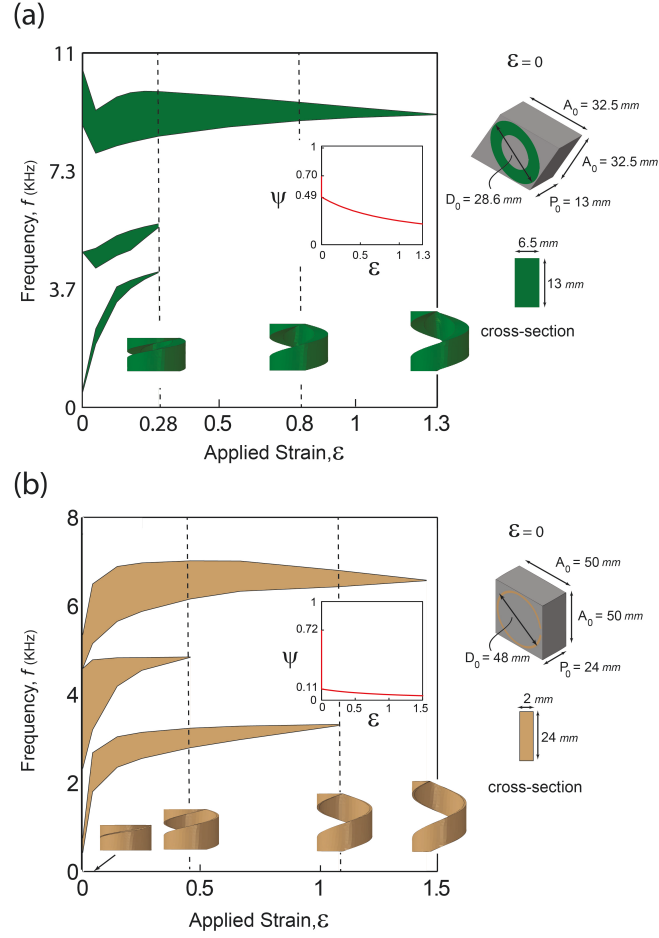


Figure 4.4: Effect of arrangement of the helices and their geometry. (a) Evolution of the bandgap frequency, f , as a function of the applied strain, ϵ , for a triangular array (with lattice spacing $A_0 = 32.5$ mm) of the helices with initial outer diameter $D_0 = 28.6$ mm, pitch $P_0 = 13$ mm, and rectangular cross-section of 13×6.5 mm. (b) Evolution of the bandgap frequency, f , as a function of the applied strain, ϵ , for a square array (with lattice spacing $A_0 = 50$ mm) of the helices with initial outer diameter $D_0 = 48$ mm, pitch $P_0 = 24$ mm, and rectangular cross-section of 24×2 mm. The insets show the evolution of the solid volume fraction as function of the applied strain.

4.4 SUMMARY

In summary, we demonstrated both numerically and experimentally that deformation in periodic arrays of helices can be intentionally exploited to switch on and off the propagation of the sound. Our results indicate that externally applied tension provides a simple mechanism to alter significantly the solid volume fraction of the system and consequently, achieve a wide range of tunability for the bandgap. Importantly, the transformation of the bandgaps is fully reversible and the range of frequencies affected by the applied deformation can be tuned by varying the geometry of the helices. Moreover, although in this study we only demonstrated the concept at the centimeter-scale, the proposed design can be applied to various length-scales, enabling the design of materials and devices to control the propagation of ultrasound (in the case of microscale systems) and infrasound (in the case of macroscale systems). From a practical perspective, the full active control over the propagation of sound in combination with the wealth of different length scales and geometrical designs provides a new class of architected materials with a broad field of applications ranging from switchable wave guides to tunable imaging devices.

This chapter has already been published in:

S. Babae, J. B. Overveldeh, E. R. Chen, V. Tournat, and K. Bertoldi, Reconfigurable Origami-inspired Acoustic Waveguides, Submitted.

5

Reconfigurable Origami-inspired Acoustic Waveguides

5.1 OVERVIEW

We combine numerical simulations and experiments to design a new class of reconfigurable waveguides based on 3D origami-inspired metamaterials. Our strategy builds on the fact that the rigid plates and hinges forming these structures define networks of tubes that can be easily reconfigured. As such, they provide an ideal platform to actively control and redirect the propagation of sound. Interestingly, we design reconfigurable systems that, depending of the externally applied deformation, can act as networks of waveguides oriented along either one or two or three preferential directions. Moreover, we demonstrate that the capability of the structure to guide and radiate acoustic energy along well predefined directions can be easily switched on and off, as the networks of tubes are reversibly formed and disrupted. The proposed designs expand the ability of existing acoustic metamaterials and exploit complex waveguiding to enhance the control of propagation and radiation of acoustic energy, opening avenues for the design of a new class of tunable acoustic functional systems.

5.2 INTRODUCTION

Acoustic waveguides designed to direct sound are ubiquitous and can be found in cars, buildings, jet engines, medical devices and musical instruments, just to name a few. While most of the proposed acoustic waveguides consist of a single duct, it is well known that tubes carefully connected together can result in significant transmitted noise reduction^{123,106}. Moreover, it has also been shown that the propagation of acoustic waves in tubes arranged to form a square lattice can be successfully described with tools from solid state physics and provides opportunities for control of sound through dispersion and band gaps³³. Finally, three-dimensional networks of

waveguides have been used to study sound propagation in regular urban areas⁹². Although these examples illustrate the potential of acoustic waveguides with more complex geometry, they only cover a small region of the available design space and a natural question to ask is how the geometry of the three-dimensional networks of tubes affects the propagation of sound.

Origami⁶⁷ - the ancient art of paper folding - not only results in intricate and aesthetically pleasant designs, but also provides an ideal platform for the design of transformable mechanical metamaterials. In particular, two-dimensional sheets folded along pre-defined creases have enabled the design of multistable structures^{134,159,49,145}, materials with negative Poisson's ratio^{35,151,160} and tunable stiffness¹³³ and topological metamaterials²⁸. While most of the proposed origami-like metamaterials are based on two-dimensional folding patterns, snapology^{46,138} - a modular origami technique - has recently inspired the design of highly reconfigurable three-dimensional metamaterials assembled from extruded polyhedra^{99,100}. Importantly, these designs also result in interconnected and reconfigurable networks of tubes defined by the assembly of rigid plates and elastic hinges. In this article we combine experiments and simulations to demonstrate that such three-dimensional networks of tubes can be exploited to design reconfigurable acoustic waveguides capable of efficiently controlling and redirecting the propagation of sound.

5.3 RESULTS

5.3.1 RECONFIGURABLE ACOUSTIC WAVEGUIDES BASED ON EXTRUDED CUBES

We start by considering a three-dimensional mechanical metamaterial consisting of a cubic array of connected extruded cubes (see Figure 5.1). If we assume that all the

faces are rigid and the structure can only fold along the edges, this periodic structure will have three degrees of freedom identified by the angles α_1 , α_2 , and α_3 ⁹⁹. Importantly, changing these three angles not only deforms the assembly of plates into numerous specific shapes, but also significantly alters the network of channels defined by them (see Figure 5.1), providing an ideal platform for the design of reconfigurable acoustic waveguides.

More specifically, for $(\alpha_1, \alpha_2, \alpha_3) = (\pi/2, \pi/2, \pi/2)$ the system is fully expanded and comprises a three-dimensional network of interconnected channels oriented in three perpendicular directions (Figure 5.1A). As for this configuration the tubes are acoustically coupled, we expect the radiation by the structure to take place in all three directions, covering the entire surrounding space without a specific directivity. Differently, for $(\alpha_1, \alpha_2, \alpha_3) = (\pi/2, \pi/2, 0)$ and $(\pi/3, 2\pi/3, \pi/3)$ the channels are all parallel to each other (Figure 5.1, B and C), so that sound waves can only propagate in one direction. However, for $(\alpha_1, \alpha_2, \alpha_3) = (\pi/2, \pi/2, 0)$ the channels are disjointed, while for $(\alpha_1, \alpha_2, \alpha_3) = (\pi/3, 2\pi/3, \pi/3)$ they are all connected. Therefore, for $(\alpha_1, \alpha_2, \alpha_3) = (\pi/2, \pi/2, 0)$ we expect the system to behave as a classical single-tube waveguide, while for $(\alpha_1, \alpha_2, \alpha_3) = (\pi/3, 2\pi/3, \pi/3)$ we expect the additional wave interferences in the structure to result in a more complex frequency response and a variety of radiation patterns.

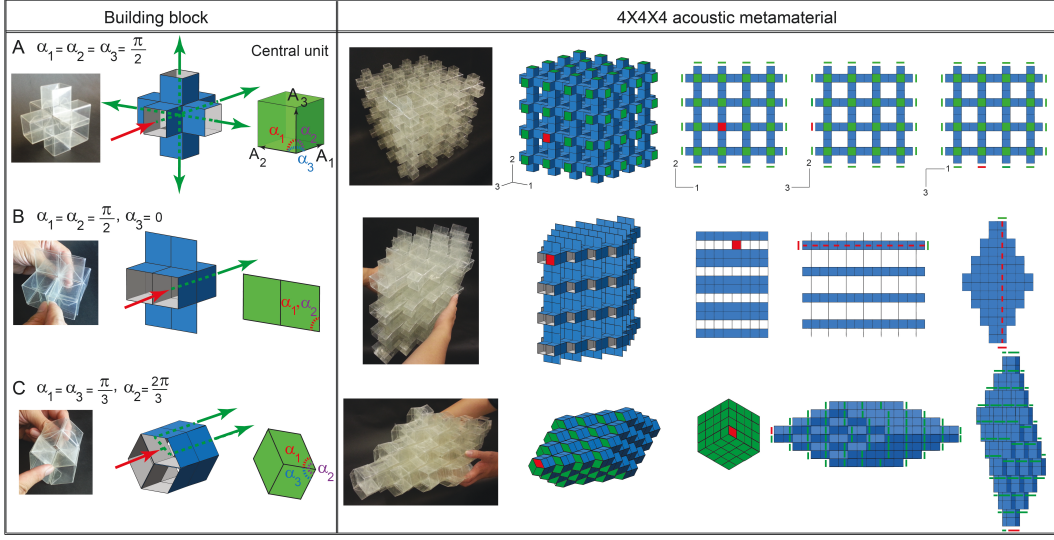


Figure 5.1: Reconfigurable origami-inspired acoustic waveguides. Experimental and numerical images of the the building block (the extruded cube) and the corresponding reconfigurable acoustic metamaterial deformed into three different configurations: (A) $(\alpha_1, \alpha_2, \alpha_3) = (\pi/2, \pi/2, \pi/2)$; (B) $(\alpha_1, \alpha_2, \alpha_3) = (\pi/2, \pi/2, 0)$; (C) $(\alpha_1, \alpha_2, \alpha_3) = (\pi/3, 2\pi/3, \pi/3)$. The red arrows and shaded areas indicate the excited waves, while the green arrows and shaded areas highlight the points from which the structure radiates.

To demonstrate our ideas, we investigated both numerically and experimentally the propagation of sound waves through the proposed reconfigurable metamaterial. In the simulations we constructed three-dimensional models of the metamaterial comprising a $4 \times 4 \times 4$ cubic array of extruded cubes and deformed them into the three different configurations shown in Figure 5.1. The plates forming the structure were considered as reflective rigid boundaries and the air inside and around the resulting tubes was meshed using acoustic elements (Abaqus element type AC3D10M). Moreover, non-reflecting boundary conditions were imposed on the outer boundaries of the acoustic medium to avoid the reflection of energy back into it. Finally, acoustic waves were excited by applying a harmonically varying pressure to one of the openings (highlighted in red in Figure 5.1) and the steady-state dynamic linearized response of the system

was calculated for a wide range of frequencies using the commercial Finite Element package Abaqus.

Furthermore, we fabricated a centimeter-scale prototype of the metamaterial from polymeric sheets (PET) and double-sided tape, using a stepwise layering and laser-cutting technique^{39,99} (see Methods for more details). To measure the transmission response of the three-dimensional waveguide, acoustic waves were excited through air inside the tubes using a loudspeaker placed at one end of one of the tubes (labeled as S in red in Figure 5.2). Then the amplitude of the both excited and scattered pressure waves were recorded using two microphones (model 378B02, PCB Piezotronics) mounted near the input loudspeaker (point S) and outlets (point A). Finally, the transmittance was computed in dB as the ratio between the output and input amplitude signals (i.e., $20 \log_{10} \| A_A(f)/A_S(f) \|$). Note that during the tests the sample was surrounded by sound absorbing foams to lower the influence of spurious reflections outside of the structure and mimic free field conditions. These foam layers were removed before taking the pictures shown in Figure 5.2 for the purpose of better visualization.

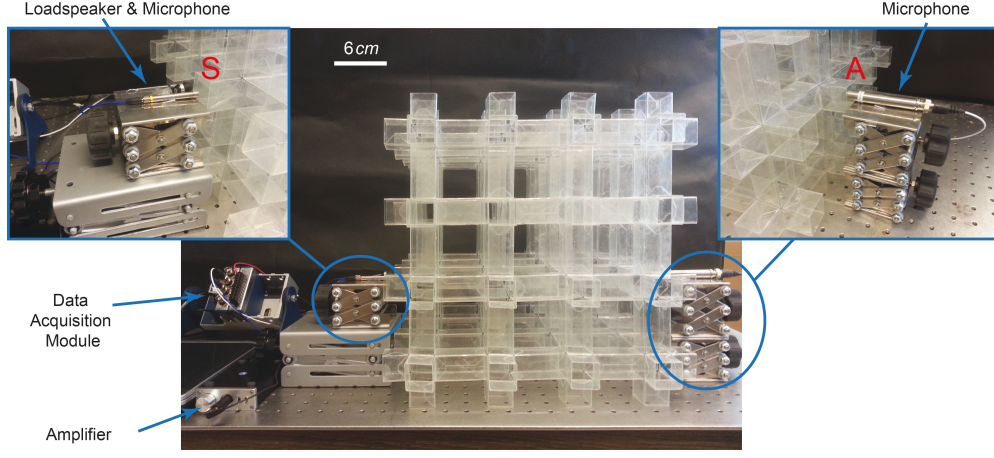


Figure 5.2: Experimental setup. Experimental setup without the sound absorbing foams surrounding the sample.

In Figure 5.3 we focus on the configuration defined by $(\alpha_1, \alpha_2, \alpha_3) = (\pi/2, \pi/2, 0)$ and present our combined numerical and experimental results for the propagation and radiation of acoustic waves generated by a source located at one of the openings (highlighted in red in Figure 5.3A). Since in this configuration the tubes are all parallel and disconnected from each other, the system behaves as a single-tube waveguide. As such, the acoustic energy remains mostly confined in the excited tube with weak radiation out of the structure (Figures 5.3B and C.1) and its frequency response is characterized by regularly spaced resonances (corresponding to the peaks of the transmittance curve reported in Figure 5.3C)⁹³. It is well known that such resonance frequencies can be predicted analytically by solving the Helmholtz equation for the pressure field⁶³. In particular, for an individual channel of length L with a square cross section of edge a , rigid side-walls and zero-pressure condition at the two ends, the resonance frequencies are given by

$$f_{lmn} = \frac{c_0}{2\pi} \sqrt{\left(\frac{l\pi}{a}\right)^2 + \left(\frac{m\pi}{a}\right)^2 + \left(\frac{n\pi}{L}\right)^2}, \quad (5.1)$$

where $c_0 = 343.2 \text{ m/s}$ is the speed of sound in air and l , m and n are three integers characterizing the waveguide modes. Since in our system $L = 14a$, its lowest modes are characterized by $l = m = 0$ and correspond to standing plane waves along the tube. In fact, for $a = 3 \text{ cm}$ as in our prototype, non-planar mode across the waveguide section can propagate only for $f > f_{100} = f_{010} = c_0/(2a) = 5.7 \text{ kHz}$. We also note that, while Eq. (5.1) provides a good qualitative estimation of the resonances of the tube, it is insufficient for quantitative comparison with experiments²⁴. In fact, the wave radiation at the tube open-ends results in a deviation from the zero pressure condition considered in deriving Eq. (5.1). Classically, this effect can be accounted for by adding a correction length 2δ to the physical length L of the tube, which depends on the details of the tube geometry. Here, by comparing analytical and numerical results, we find a good agreement for $\delta = 0.3a$, so that the resonance frequencies of the planar modes are given by $f_{00n} = nc_0/[2(L + 0.6a)]$. Finally, we note a very good agreement between our analytical, numerical and experimental results (see Figure 5.3C), with only a few dB level discrepancy between simulated and experimental curves.

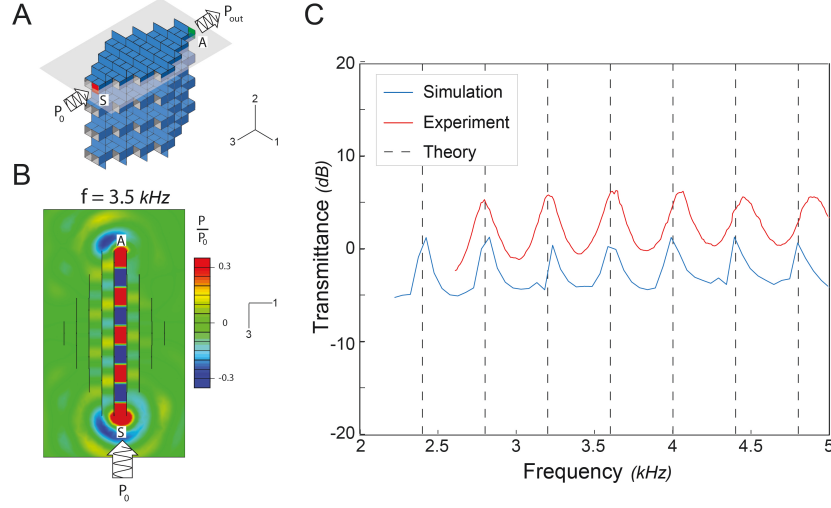


Figure 5.3: Propagation of sound waves for $(\alpha_1, \alpha_2, \alpha_3) = (\pi/2, \pi/2, 0)$. (A) Numerical image of the metamaterial. (B) Top cross-sectional view of the pressure field distribution at $f = 3.5 \text{ kHz}$. The cutting plate is shown in (A) and the color indicates the pressure amplitude normalized by the input signal amplitude (p_0) (C) Frequency-dependent transmittance for the sample. Both experimental (red lines), numerical (blue line) and analytical (dashed black lines) results are shown.

Next, in Figure 5.4 we present results for the configuration defined by $(\alpha_1, \alpha_2, \alpha_3) = (\pi/3, 2\pi/3, \pi/3)$. Although in this case the channels are also all oriented along the same direction, they have a rhombic cross section and are interconnected inside the structure. Consequently, when deformed into this state the metamaterial is characterized by a totally different acoustic response. This is clearly demonstrated in Figure 5.4, A and B, where we show the transmittance calculated using two different detection points (denoted as A and B in Figure 5.4C). Both curves exhibit a strong and complex frequency dependence, originating from the interferences that occur inside the system as the waves can follow a myriad of different paths when traveling from the source to the receiver due to the multiple interconnections. We also find that the connectivity of the tubes reduces the average level of the transmittance over the studied frequency range to around -20 dB, significantly lower than that measured for the

configuration of Figure 5.3. Moreover, it should be noted that for this case quantitative agreement between simulated and experimental transmittances is not reached. This is because here geometric imperfections play a much bigger role than in the case of a single tube waveguide, as they significantly alter the path followed by the traveling waves and, consequently, the wave interferences. Finally, we find that not only the transmittance, but also the radiation patterns are strongly frequency dependent. For example, at 2 kHz the wave radiation by the structure gives rise to frontward quasi-plane waves, while at 4.8 kHz the wave fronts are more curved and show complex spatial patterns (Figure 5.4C). Interestingly, we find that at 4.8 kHz the modes propagating in the tubes are also non-planar, although $f < 5.7\text{ kHz}$. This is due to the interconnections between air channels that increase the effective width of the waveguide structure. Consequently, we expect a multi-modal propagation in the structure to start at lower frequencies (typically $\sim 2\text{ kHz}$) than those calculated in the case of the independent single tubes (i.e., for $(\alpha_1, \alpha_2, \alpha_3) = (\pi/2, \pi/2, 0)$).

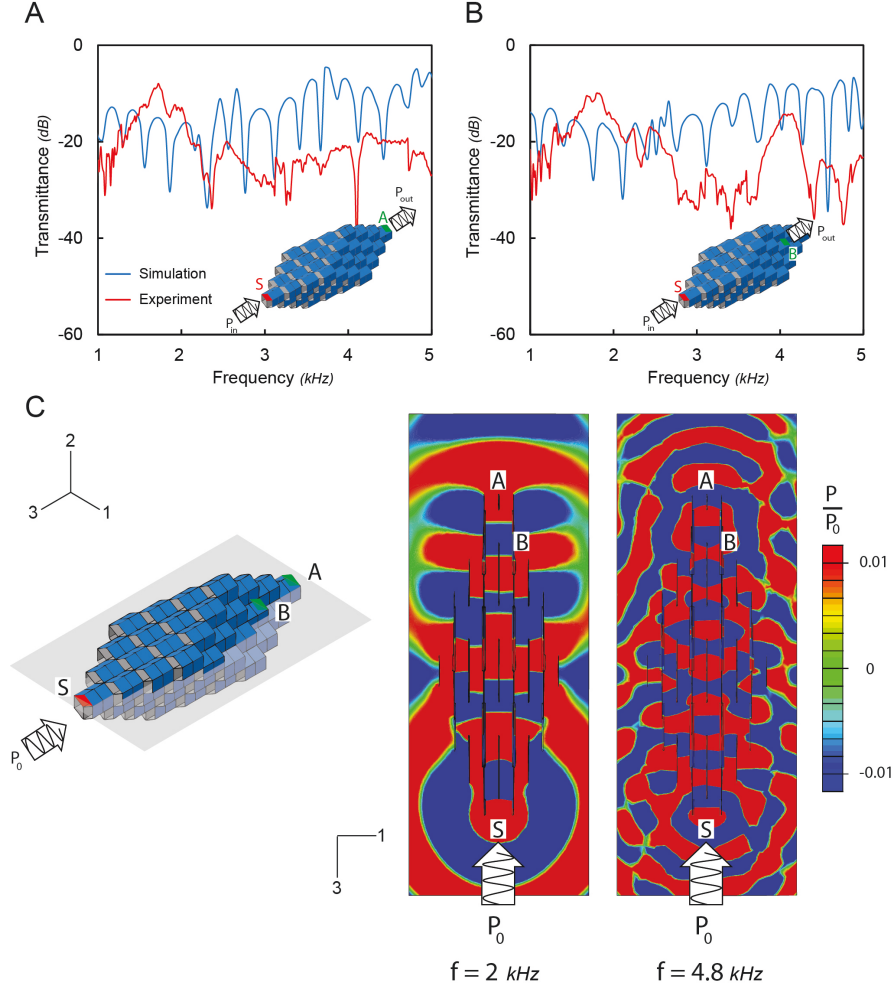


Figure 5.4: Propagation of sound waves for $(\alpha_1, \alpha_2, \alpha_3) = (\pi/3, 2\pi/3, \pi/3)$. (A) and (B) Frequency-dependent transmittances for the sample calculated considering two different detection points. Both experimental (red lines) and numerical (blue line) results are shown. (A) Numerical image of the metamaterial. (B) Top cross-sectional view of the pressure field distribution at $f = 2 \text{ kHz}$ and $f = 4.8 \text{ kHz}$. The cutting plate is shown in (A) and the color indicates the pressure amplitude normalized by the input signal amplitude (p_0)

Finally, in Figure 5.5 we focus on the expanded state of the system defined by $(\alpha_1, \alpha_2, \alpha_3) = (\pi/2, \pi/2, \pi/2)$, for which the waveguides are interconnected and oriented in three orthogonal directions. Similar to the case of Figure 5.4, A and B, the transmittance curves reported in Figure 5.5, A and B have an average value of ~ -20

dB and show a complex frequency dependence. Due to the waveguide interconnections, numerous interferences from the possible paths come into play even in the case of detection at point A which is aligned with the source. Moreover, as the waveguides are oriented in three different directions, the wave radiation by the structure covers the entire surrounding space (Figure 5.4, C and D) and we observe a much smaller radiated amplitude behind the structure (oppositely to the source) than for the previous configurations of aligned waveguides.

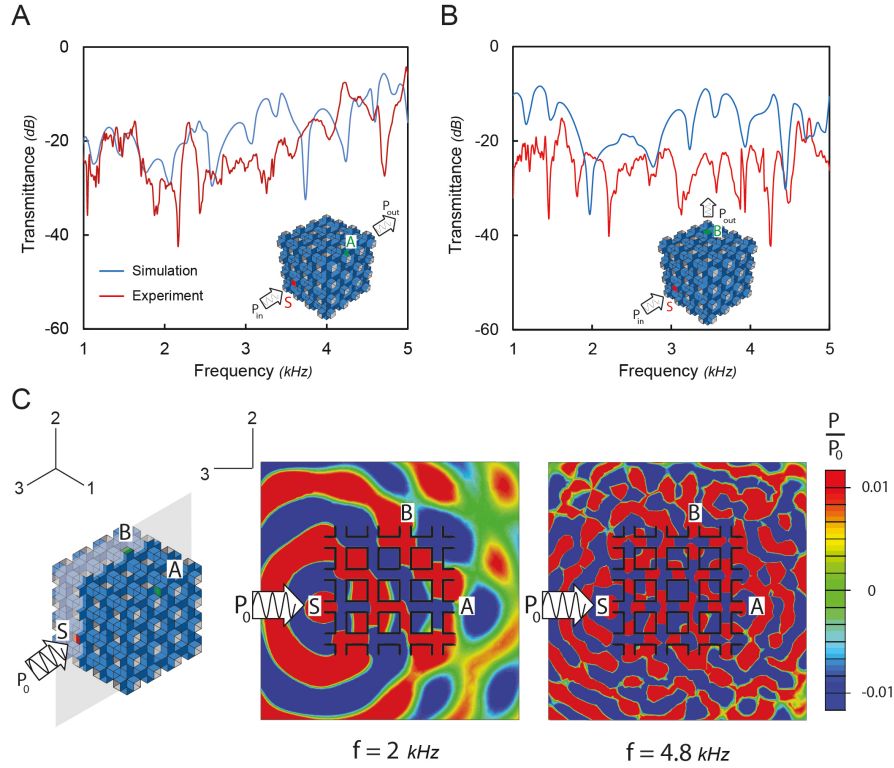


Figure 5.5: Propagation of sound waves for $(\alpha_1, \alpha_2, \alpha_3) = (\pi/2, \pi/2, \pi/2)$. (A) and (B) Frequency-dependent transmittances for the sample calculated considering two different detection points. Both experimental (red lines) and numerical (blue line) results are shown. (A) Numerical image of the metamaterial. (B) Top cross-sectional view of the pressure field distribution at $f = 2 \text{ kHz}$ and $f = 4.8 \text{ kHz}$. The cutting plate is shown in (A) and the color indicates the pressure amplitude normalized by the input signal amplitude (p_0)

5.3.2 RECONFIGURABLE ACOUSTIC WAVEGUIDES BASED ON DIFFERENT EXTRUDED POLYHEDRA

While so far we have focused on a metamaterial comprising a cubic array of extruded cubes, the proposed strategy to design reconfigurable acoustic waveguides is not restricted to this specific geometry. In fact, a wealth of three-dimensional reconfigurable networks of tubes capable of qualitatively different deformation can be realized by taking space-filling tessellations of convex polyhedra as templates, and extruding arbitrary combinations of their polygonal faces¹⁰⁰.

As an example, in Figure 5.6, A, B and C we consider a metamaterial based on a tessellation of truncated octahedra. While the resulting structure is rigid if all the faces of the truncated octahedra are extruded¹⁰⁰, here we construct a metamaterial with a single degree of freedom (denoted by θ in Figure 5.6A) by extruding the 8 green hexagonal faces (highlighted in green in Figure 5.6A), removing 4 of the square faces (highlighted in yellow in Figure 5.6A) and making the two remaining ones rigid (highlighted in blue in Figure 5.6A). As for the case of the metamaterial based on the extruded cubes, by changing θ between 0 and $\pi/2$ the architecture of the system can be transformed (see Figure 5.6, A, B and C, and Figure D.3). However, in this case for $0 < \theta < \pi/2$ the metamaterial does not act as an acoustic waveguide, since it does not comprise a network of interconnected tubes (Figure 5.6A). Only for $\theta = 0$ and $\theta = \pi/2$ the plates defining the structures form interconnected channels that can be used to guide acoustic waves. More specifically, for $\theta = 0$ all tubes are parallel and disconnected (Figure 5.6B), so that that the system behaves as a single-tube waveguide and has identical response as the extruded cube waveguide for

$(\alpha_1, \alpha_2, \alpha_3) = (\pi/2, \pi/2, 0)$ (see Figure 5.3). Differently, for $\theta = \pi/2$ the folded structure functions as a two-dimensional waveguide (see the red arrows in Figure 5.6C). Importantly, this example highlights another interesting feature of our design platform: the ability of switching on and off the guiding of acoustic energy, as for certain configurations the networks of tubes can be reversibly formed and disrupted.

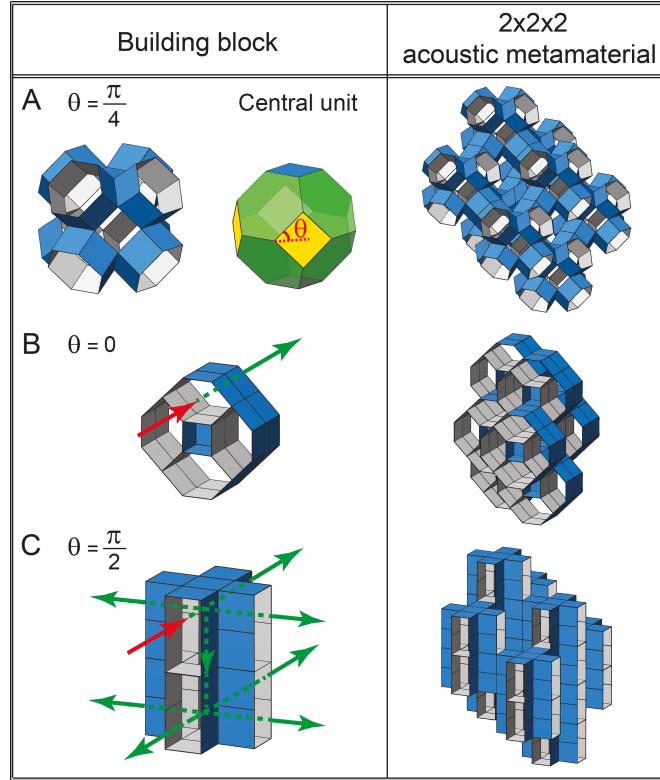


Figure 5.6: Reconfigurable acoustic waveguide based on a tessellation of truncated octahedra. Experimental and numerical images of the the building block (the extruded cube) and the corresponding reconfigurable acoustic metamaterial deformed into three different configurations: (A) $\theta = \pi/4$; (B) $\theta = 0$; (C) $\theta = \pi/2$.

Finally, we use extruded hexagonal prisms to construct a system that can act either as a one-dimensional or a two-dimensional or a three-dimensional waveguide (Figure 5.7, A, B, C and D). More specifically, the building block of this structure is

an hexagonal prism with all its faces extruded except for two square faces that are kept rigid (highlighted in blue in Figure 5.7A). The metamaterial formed by connecting these extruded unit cells is highly deformable and characterized by two degrees of freedom, denoted by α and γ in Figure 5.7A. Differently from the structures considered in Figure 5.6, here for any admissible combination of (α, γ) the assembly of plates and hinges forms a network of tubes that can be exploited as an acoustic waveguide. In the expanded configuration defined by $(\alpha, \gamma) = (0, 0)$ the structure acts as a three-dimensional waveguide as the excited waves (red arrow in Figure 5.7A) can propagate along three different directions (green arrow in Figure 5.7A). However, by applying an external force we can transform the metamaterial into either a two-dimensional (for $(\alpha, \gamma) = (-\pi/4, -\pi/4)$ - Figure 5.7C) or a one-dimensional (for $(\alpha, \gamma) = (\pi/4, \pi/4)$ - Figure 5.7D) or a three-dimensional with mutually perpendicular channels (for $(\alpha, \gamma) = (\pi/4, -\pi/4)$ - Figure 5.7B) waveguide (see Figure D.5).

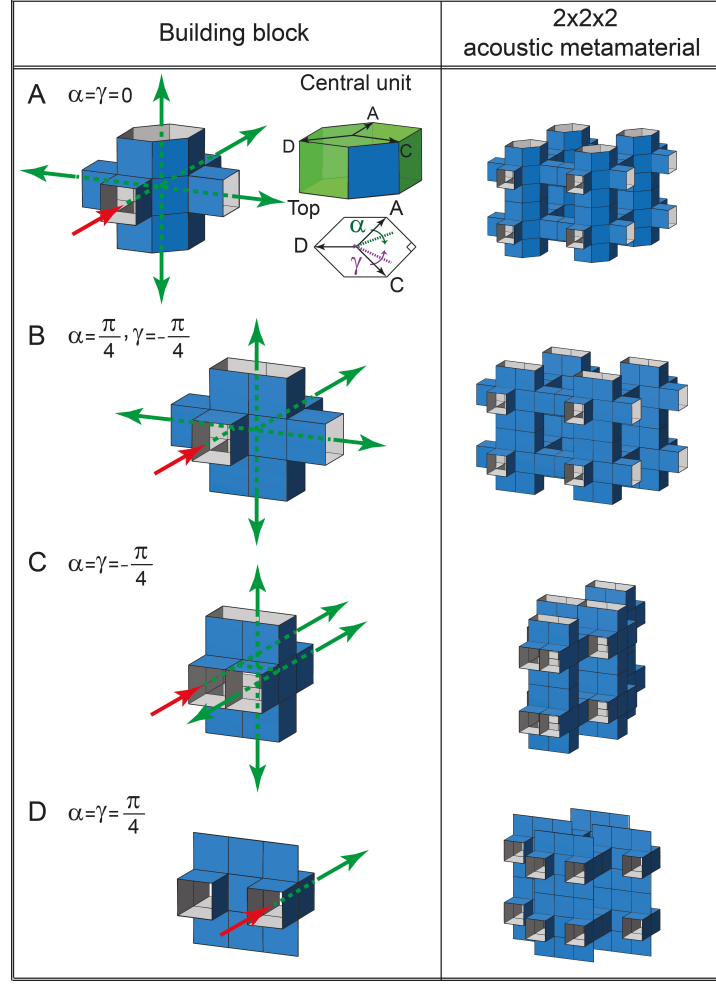


Figure 5.7: Reconfigurable acoustic waveguide based on a tessellation of hexagonal prisms. Experimental and numerical images of the the building block (the extruded cube) and the corresponding reconfigurable acoustic metamaterial deformed into four different configurations: (A) $(\alpha, \gamma) = (0, 0)$; (B) $(\alpha, \gamma) = (\pi/4, -\pi/4)$; (C) $(\alpha, \gamma) = (-\pi/4, -\pi/4)$; (D) $(\alpha, \gamma) = (\pi/4, \pi/4)$.

5.4 DISCUSSION

In summary, we propose a new type of reconfigurable acoustic waveguides based on origami principles. Our results indicate that the reconfigurability of the networks of waveguides defined by the origami structures can be exploited to achieve very differ-

ent acoustic responses and wave radiation patterns. Remarkably, the involved acoustic mechanisms are broadband, show a rich behavior in frequency and can be easily reproduced at different scales, from millimeter to meter large structures.

It should be noted that our strategy to control wave propagation and radiation is based on networks of tubes supporting acoustic waves. Interestingly, these simple systems have not been widely studied yet in this context, as in recent years the control of sound wave propagation has been mostly achieved by structuring waveguides with periodic scatterers^{21,62,97} or resonators^{139,112,48}. While in the most of the reported metamaterials the functionality is locked into place once they are fabricated, tunability has also been demonstrated by rotation of the scatterers^{45,113,152,74}, thermal radiation¹⁴⁶, adjustable resonating components^{26,141} and applied mechanical deformation¹¹. However, in all these systems the tunability is limited to a relatively narrow frequency range. In contrast, the dramatic reconfiguration of the waveguides proposed here for audible acoustics is broadband and represents a new way of tuning and even switching the propagation of sound. All together, the large number of origami waveguide structures that can be designed, the richness of their deformation modes, as well as the possibility of use both single unit cells and complex ensembles leave many opportunities to guide and control the propagation of waves, with possible applications going well beyond the first demonstration of wave guiding and radiation reported here.

5.5 METHODS

5.5.1 FABRICATION

The metamaterial comprising an array of extruded cubes is fabricated from thin polymeric sheets using an efficient stepwise layering and laser-cutting technique. To fabricate each of the six extruded rhombi that together form a building block (an extruded cube), we use a nearly inextensible polyethylene terephthalate sheet with thickness of $t = 0.25\text{ mm}$, covered with a double-sided tape layer (3M VHB Adhesive Transfer Tapes F9460PC) with a thickness of $t = 0.05\text{ mm}$ and bonded to a second, thinner polyethylene terephthalate layer ($t = 0.05\text{ mm}$). Cutting slits are introduced into using a CO2 laser system (VLS 2.3, Universal Laser Systems) and the extruded rhombi could then be formed by removing the parts from the layered sheet, and bonding their ends together.



Supporting Information to Chapter 2

A.1 BUILDING BLOCKS

The building blocks for all the proposed metamaterials are patterned spherical shells¹²⁹, in which a significant change in volume is observed as a result of elastic instabilities. Since here we focus on cubic crystal systems and require both the building blocks and the metamaterial to have octahedral symmetry, only patterned spherical shells with 6, 12 and 24 holes are considered. Different views of the three building blocks discussed in this study are shown in Figure A.1.

A.2 REPRESENTATIVE VOLUME ELEMENTS

Since each building block has a limited number of sites where adjacent building blocks can be attached to each other and metamaterials with octahedral symmetry can only be built through connecting identical junctions, only six different Bucklicrystals can be built: *bcc* crystals using building blocks with 6, 12 or 24 holes, *sc* crystals using building blocks with 12 or 24 holes and *fcc* crystal using building blocks with 24 holes. Different views of the representative volume elements (RVEs) for each metamaterial in the undeformed configuration are shown in Figure A.2.

A.3 EXPERIMENTS

To monitor the evolution of the Poisson's ratio of the fabricated Bucklicrystal, we tested the structure under uniaxial compression. At the strain level of interest, we immobilized the specimen using a fixture made of acrylic plates, nylon bolts/nuts and inch-thick closed-cell foam plates placed between the specimen and the fixture (see Figure A.3). The foam plates were used as a low electron density spacer that would

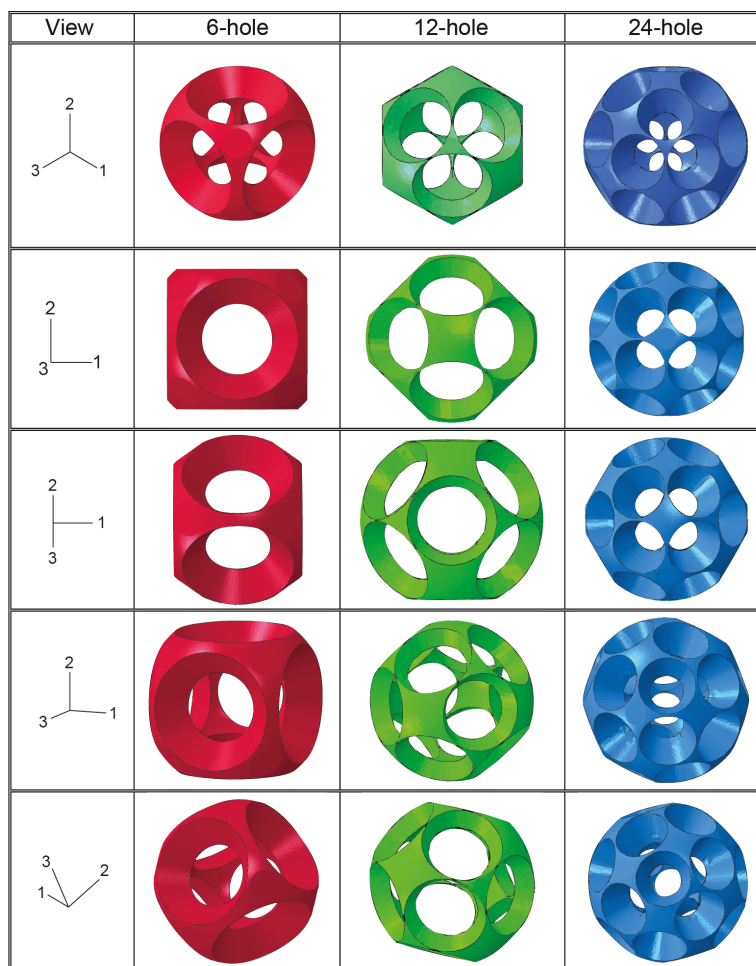


Figure A.1: Different views of the building blocks with 6, 12, and 24 holes.

be nearly invisible in the acquired x-ray transmission images and thus not interfere with volume rendering of the higher electron density silicone elastomer Bucklicrystal.

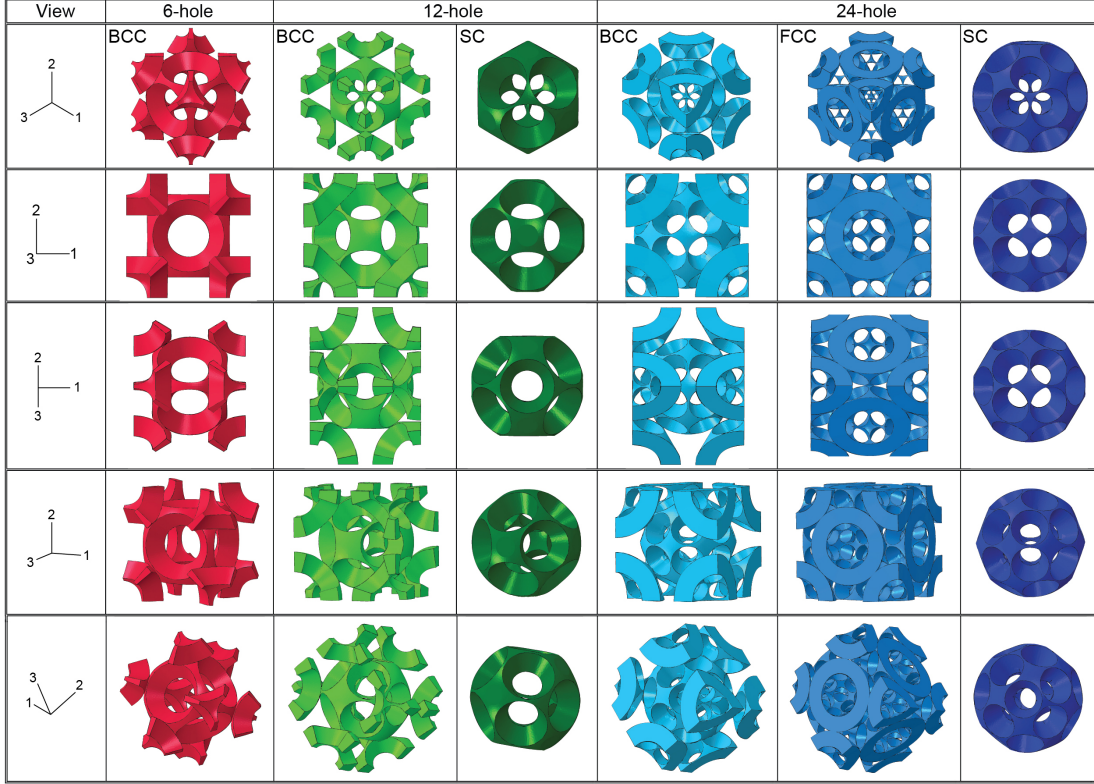


Figure A.2: Different views of the undeformed RVEs for all the proposed Bucklicrystals.

A.4 NUMERICAL SIMULATIONS OF STABILITY ANALYSIS FOR 3D PERIODIC STRUCTURES

We investigated the buckling of 3D periodic porous structures using non-linear finite element (FE) analyses. The FE calculations were conducted within the nonlinear code ABAQUS, version 6.8-2. In the numerical analyses, we investigated the stability of infinitely periodic structures comprising of an array of perfectly connected building blocks. For the sake of computational efficiency, the analyses were conducted on representative volume elements (RVEs) (see Figure A.2).

For infinite periodic structures, it is useful to make the distinction between *micro-*

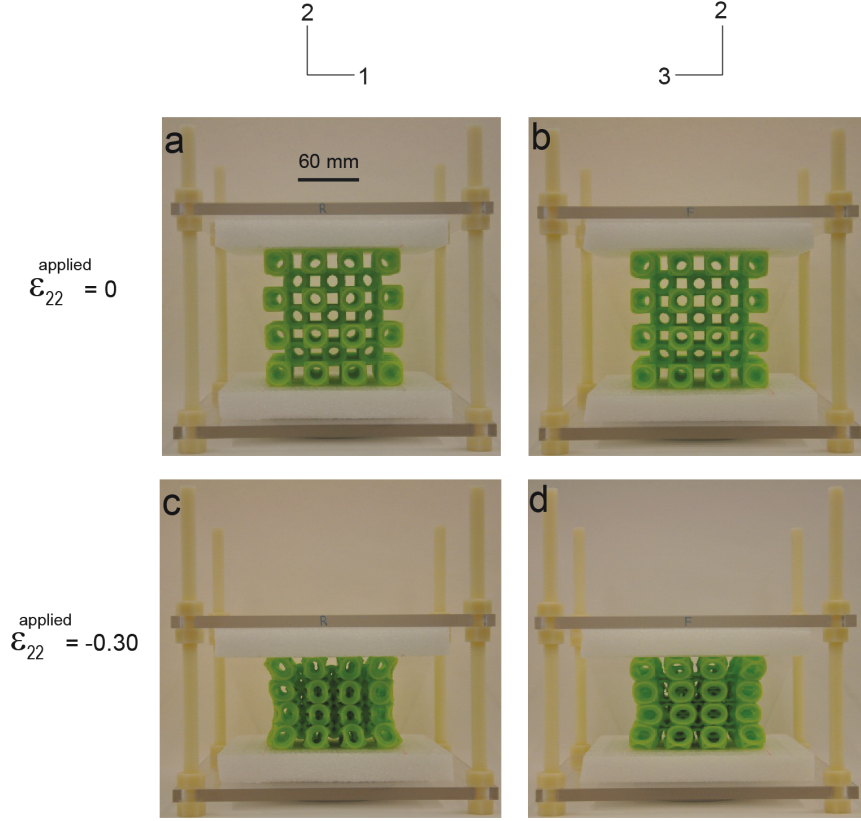


Figure A.3: Testing of the Bucklicrystal. a,b) Undeformed configuration. c,d) Deformed configuration at $\epsilon_{22}^{applied} = -0.3$. (scale bar: 60mm)

scopic instabilities (i.e. instabilities with wavelengths that are of the order of the size of the microstructure) and *macroscopic* instabilities (i.e. instabilities with much larger wavelengths in comparison to the size of the unit cell)^{43,144,16,102}.

MICROSCOPIC INSTABILITIES. Although microscopic (local) buckling modes may alter the initial periodicity of the solid, they can still be detected by studying the response of a single unit cell and investigating the propagation of small-amplitude waves with an arbitrary wave vector superimposed on the current state of deformation^{43,144,16}. While a real angular frequency ω corresponds to a propagating wave, a

complex ω identifies a perturbation exponentially growing with time. Therefore, the transition between stable and unstable configurations is detected when the frequency vanishes (i.e. $\omega = 0$) and the new periodicity of the solid introduced by instability can be easily obtained by the corresponding wave vector. Here, the finite-element method was used to perform the Bloch wave analysis¹⁶.

MACROSCOPIC INSTABILITIES. Following Geymonat et al.⁴³, we examined macroscopic instabilities by detecting the loss of strong ellipticity of the overall response of the periodic structure. Specifically, for the metamaterials considered in this study macroscopic instabilities may occur whenever the condition

$$\mathbb{L}_{ijkl}^H N_j N_l m_i m_k > 0 \quad \text{for} \quad \mathbf{m} \otimes \mathbf{N} \neq 0, \quad (\text{A.1})$$

is first violated along the loading path, \mathbb{L}^H being the macroscopic (homogenized) tangent modulus and \mathbf{N} and \mathbf{m} denoting unit vectors. Note that \mathbb{L}^H is evaluated numerically by subjecting the RVE to nine independent linear perturbations of the macroscopic deformation gradient¹⁶.

A.5 STABILITY ANALYSIS FOR 6-HOLE BUCKLICRYSTAL

We started by investigating the stability of the 6-hole Bucklicrystal. For the considered periodic structure, the onsets of both microscopic and macroscopic instabilities were detected by studying the response of the RVE depicted in Figure A.4-left. A microscopic instability was detected at $\epsilon_{22} = -0.03$, while the onset of macroscopic instability occurs at $\epsilon_{22} = -0.06$. Therefore, microscopic instabilities were always critical in compression, leading to a critical mode where all building blocks underwent the

same rotation (see Figs. A.4-right), without altering the structure's periodicity.

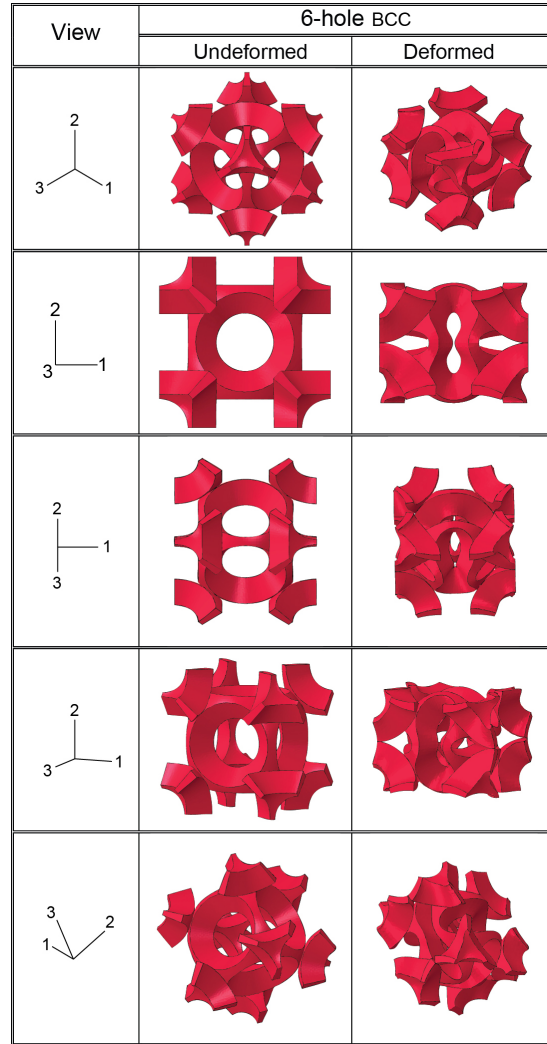


Figure A.4: Left: RVE for the undeformed 6-hole *bcc*. Right: Critical mode detected by the Bloch wave analysis. Note that the deformation of the RVE is slightly different in 1 and 3 directions.

A.6 STABILITY ANALYSIS FOR ALL BUCKLICRYSTALS

The onsets of both microscopic and macroscopic instabilities for each Bucklicrystal was detected by studying the response of the RVEs depicted in Figure A.2. In all Bucklicrystals, instabilities of short wavelength were found to be critical, leading to spherical collapse of all the building blocks. The values of critical strain obtained from the stability analysis are summarized in Table A.1 and the corresponding critical modes are shown in Figure A.5. Note that for *sc* configurations, buckling leads to an enlarged RVE comprising of 8 building blocks (RVE size = $2 \times 2 \times 2$ in 1, 2, and 3 directions). Moreover, it is worth noting that the non-linear deformation of the Bucklicrystals is dictated by the folding mechanism of the corresponding building blocks. Interestingly, in the Buckliball with 12 or 24 holes, all the junctions (*i.e.* the sites where adjacent building blocks can be attached to each other) rotate all in the same direction during folding (Figure A.6). As a result, in Bucklicrystals comprising arrays of building blocks with 12 or 24 holes, the folded units have two potentially different orientations (Figure A.7). In contrast, in the 6-hole Buckliball, half of the junctions rotate clockwise and half counterclockwise (Figure A.6). As a result, in the deformed configuration of the 6-hole *bcc* Bucklicrystal, all of the folded building blocks are oriented exactly in the same way (Figure A.8).

	ϵ_{22}^{micro}	ϵ_{22}^{macro}
6H-bcc	-0.030	-0.060
12H - bcc	-0.030	-0.140
12H- sc	-0.041	-0.265
24H-bcc	-0.020	-0.062
24H-sc	-0.026	-0.096
24H-fcc	-0.023	-0.050

Table A.1: Values of critical strain for microscopic (ϵ_{22}^{micro}) and macroscopic (ϵ_{22}^{macro}) instabilities.

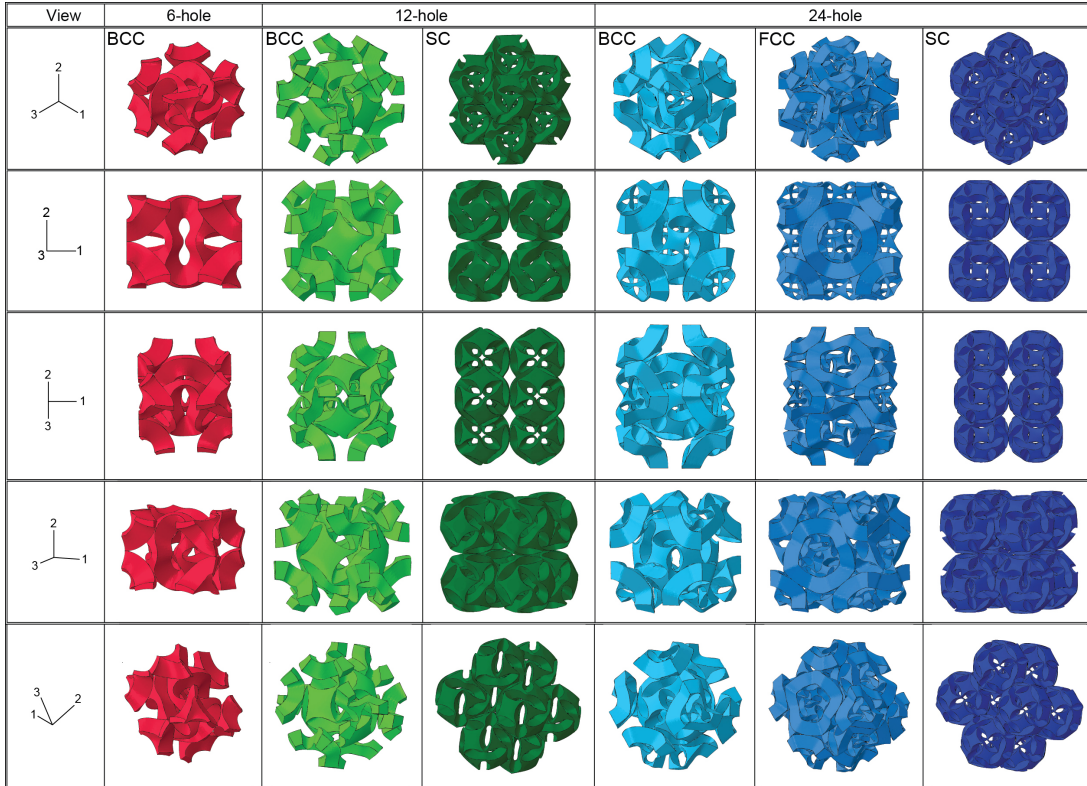


Figure A.5: Critical modes for all the Bucklicrystals under uniaxial compression. Upon applying a load in the 2- direction, all the ligaments undergo the first buckling mode and all the circular holes close uniformly. Note that for sc configurations, buckling leads to an enlarged RVE, which is comprised of 8 building blocks (RVE size = $2 \times 2 \times 2$ in 1, 2, and 3 directions).

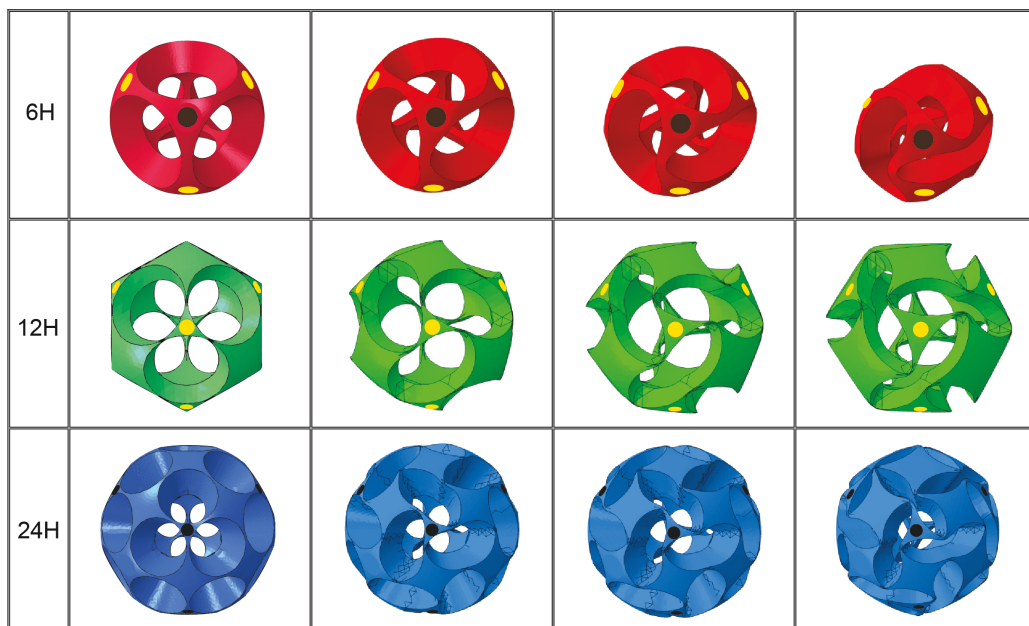


Figure A.6: Sequence of progressively deformed configurations of the building blocks. The circular markers are used to highlight the rotation of the junctions used to build *bcc* Bucklicrystals. Yellow markers indicate a counterclockwise rotation, while black markers correspond to a clockwise rotation. In the 6-hole building block, half of the junctions rotate clockwise and half counterclockwise, as indicated by the yellow and black markers. In contrast, for the building block with 12 or 24 holes, all identical junctions rotate in the same direction.

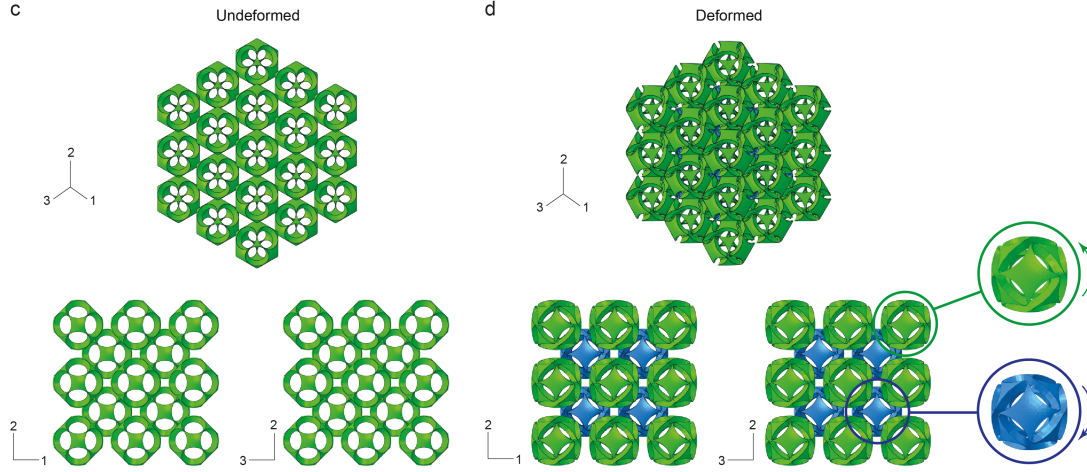


Figure A.7: Left: Enlarged RVE for the undeformed 12-hole *bcc* comprising of 35 building blocks. Right: Reconstruction of the critical mode detected for the enlarged RVE. Note that the folded building blocks have two different orientations, as indicated by the two colors (blue and green). As a result, each unit is oriented differently with respect to the surrounding connected units.

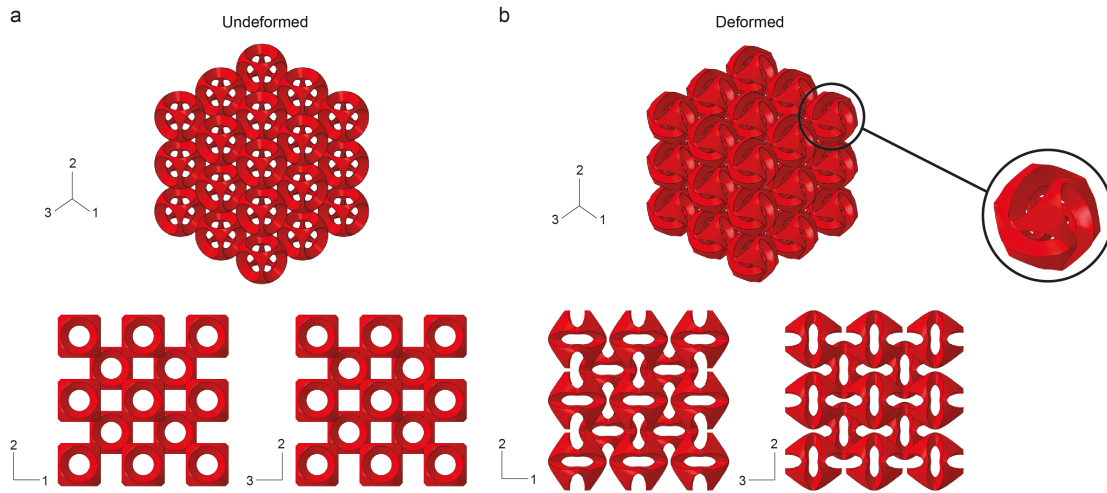


Figure A.8: Left: Enlarged RVE for the undeformed 6-hole *bcc* comprising of 35 building blocks. Right: Reconstruction of the critical mode detected for the enlarged RVE. Note that all folded building blocks have exactly the same orientation.

A.7 POROSITY OF BUCKLICRYSTALS

Each building block is fully characterized by two adimensional parameters: porosity, denoted by ψ , and thickness over inner radius ratio, denoted by t/r_i ¹²⁹. The porosity of a single building block is defined as a ratio of volume of the voids to volume of the intact shell¹²⁹

$$\psi = \frac{V_{voids}}{V_{intact\ shell}}, \quad (\text{A.2})$$

where

$$V_{intact\ shell} = \frac{4}{3}\pi(r_o^3 - r_i^3), \quad (\text{A.3})$$

r_i and r_o denoting the inner and outer radius of the spherical shell, respectively. The volume fraction of the structured shell is then simply defined as

$$V_{shell} = (1 - \psi)\frac{4}{3}\pi(r_o^3 - r_i^3). \quad (\text{A.4})$$

In this study all crystals are constructed using building blocks characterized by $\psi = 0.733$ and $(r_o - r_i)/r_i = 5/7$. It is important to note that the use of building blocks characterized by the same parameters ψ and t/r_i results in Bucklicrystals with different initial global porosities $\bar{\psi}$.

The global porosity for each packing configurations (*sc*, *bcc*, and *fcc*) is defined as

$$\bar{\psi} = 1 - \frac{N_{building\ block} V_{shell}}{V_{RVE}}, \quad (\text{A.5})$$

where $N_{building\ block}$ is the number of building blocks in the RVE and $V_{RVE} = L^3$ is the volume of the cubic RVE of length L . Note that each packing configuration is characterized by a unique pair $\langle N_{building\ block}, L \rangle$. More specifically, $\langle N_{building\ block}, L \rangle =$

$\langle 1, 2r_0 \rangle$, $\langle 2, \frac{4r_0}{\sqrt{3}} \rangle$, and $\langle 4, \frac{4r_0}{\sqrt{2}} \rangle$ for *sc*, *bcc*, and *fcc* packing configurations, respectively. Combining Eqs. (A.4) and (A.5), the global void volume fraction for Bucklicrystals characterized by $\psi = 0.733$ and $(r_o - r_i)/r_i = 5/7$ can be calculated as: $\bar{\psi}_{sc} = 0.888$, $\bar{\psi}_{bcc} = 0.854$ and $\bar{\psi}_{fcc} = 0.842$.

B

Supporting Information to Chapter 5

B.1 FABRICATION

A silicone-based rubber (commercial name: Elite Double 32, *Zhermack*) with material density $\rho = 965 \text{ kg/m}^3$ is used to cast the experimental specimen. The material properties are measured through tensile testing up to a true strain of 0.60 and no hysteresis is found during loading and unloading. The constitutive behavior is accurately captured by a nearly-incompressible (i.e., Poisson ratio $\nu_0 = 0.4999$) Yeoh hyperelastic model¹⁶¹, whose strain energy is given by

$$W = \sum_{i=1}^3 C_{i0} (\bar{I}_1 - 3)^i + \frac{(J - 1)^{2i}}{D_i}, \quad (\text{B.1})$$

where $C_{10} = 131 \text{ kPa}$, $C_{20} = 0 \text{ kPa}$, $C_{30} = 3.5 \text{ kPa}$, $D_1 = D_2 = D_3 = 1.54 \text{ GPa}^{-1}$. Moreover, $\bar{I}_1 = \text{tr} [\text{dev} (\mathbf{F}^T \mathbf{F})]$ and $J = \det \mathbf{F}$, where \mathbf{F} is the deformation gradient. Note that the initial shear modulus(G_0) and bulk modulus(K_0) at zero strain are related to two of the Yeoh model parameters as $G_0 = 2 C_{10} = 0.26 \text{ MPa}$, $K_0 = 2/D_1 = 1.3 \text{ GPa}$, so that the speed of propagating longitudinal waves through the undeformed homogeneous rubber is $c_L = 1160 \text{ m/s}$.

To manufacture the helices a molding approach is used. First, a mold is fabricated from Rigid Opaque Vero blue plastic material (product number RGD840, *Objet*) using a 3-D printer (Connex500, *Objet*) to cast a helix (see Figure B.1(a)). Before replication, a releasing agent (*SMOOTH-ON* universal mold release) is sprayed on to the mold to easily de-mold and separate the cured rubber helix from the plastic mold. The casted mixture is first placed in vacuum for degassing and is allowed to set at room temperature for curing. The single helices fabricated to study their static response (i.e., deformation) are comprised of 9.2 loops (both ends are cut flat - see

Figure B.1(b)) with rectangular cross-section of $13\text{ mm} \times 6.5\text{ mm}$, inner diameter $D_{0,in} = 15.6\text{ mm}$, outer diameter $D_0 = 28.6\text{ mm}$, and pitch $P_0 = 16.25\text{ mm}$.

To fabricate the acoustic metamaterial shown in Figure 1 of the main text, we manufacture 36 elastomeric helices and arrange them to form a 6×6 two-dimensional square lattice with center-to-center distance $A_0 = 32.5\text{ mm}$. Note that all helices are cut to comprise only 3 loops (so that their height in the undeformed configuration is $H_0 = 40\text{ mm}$) before building the specimen. The helices are then attached to two acrylic plates on the top and bottom using *Cyberbond* Apollo 2240 adhesive. We use four nylon bolts/nuts placed at the corners of the plates to immobilize the specimen at strain level of interest (Figure B.2(a)). The dimension of the specimen at $\epsilon = 0$ (i.e., undeformed configuration) is Height \times Width \times Depth = $40 \times 195 \times 195\text{ mm}$.

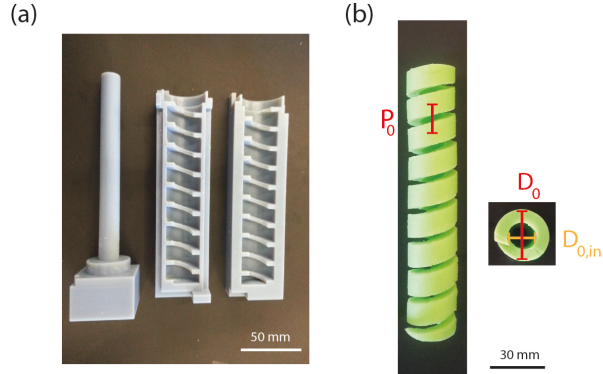


Figure B.1: Fabrication. (a) 3-D printed plastic mold, and (b) elastomeric helix manufactured using the mold and casting approach.

B.2 TESTING

We measure the propagation of sound waves through the metamaterial at two levels of applied deformation, $\epsilon = 0$ and $\epsilon = 0.9$. At the strain level of interest, we immobilize the specimen using the acrylic fixture and measure the transmission in

GX direction. In all the tests we also place a 2 inch-thick closed-cell foams all around the sample to properly close it regardless of its height (Figure B.2(c)). To excite the wave propagation through the air, we use an array of five identical loudspeakers (Vifa OT19NC00-04, 3/4 inch diameter)(Figure B.2(b)) placed along one of the faces of the sample. The loudspeakers provide a frequency sweep input signal (duration 1 second), whose frequency content is controlled with a MATLAB script (spanning from 500 Hz to 12 kHz). On the opposite face of the sample we then record the amplitude of the scattered pressure waves, $\phi(t)$, with a PCB microphone and pre-amplifier (model 378B02, PCB). Note that the transmission in air, $\phi_{air}(t)$, through the acrylic plates surrounded by foams without the helices, is also recorded. Finally, the normalized transmission spectra reported in Figure 3 in the main text are calculated as

$$T(f) = 20 \log_{10} \left(\left\| \frac{\hat{\phi}(f)}{\hat{\phi}_{air}(f)} \right\| \right)$$

where $\hat{\phi}(f)$ and $\hat{\phi}_{air}(f)$ are the Fourier transforms of the transmission through the sample and the transmission through air, respectively. Note that each curve shown in Figure 3 is based on the average of 20 measurements.

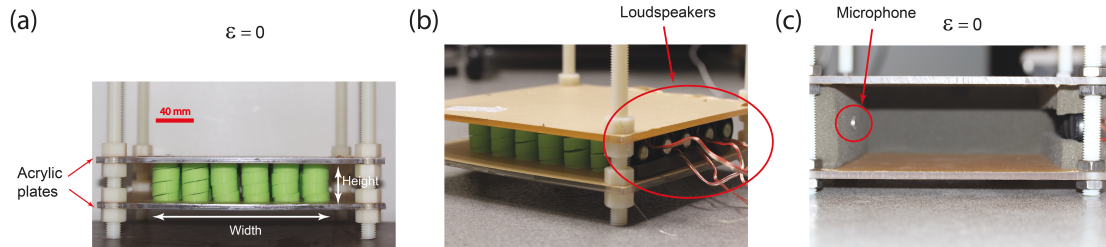


Figure B.2: Testing. (a) Front-view image of the fabricated metamaterial at $\epsilon = 0$. (b) Position of loudspeakers in the experimental set-up. (c) Experimental set-up without the metamaterial used to measure the transmission through air.

B.3 ANALYTICAL MODEL FOR DEFORMATION OF A HELIX

In this Section we present a simple analytical model to predict the effect of the applied strain, ϵ , on the morphology of a helix. In particular, we first investigate how ϵ affects its pitch P and outer diameter D , and then determine the effect of such deformation on the solid volume fraction ψ of the metamaterial.

We start by noting that the deformed configuration of the helix is described by the vector function

$$\mathbf{r}(\theta) = (x(\theta), y(\theta), z(\theta)) = \left(\frac{D}{2} \cos \theta, \frac{D}{2} \sin \theta, \frac{P}{2\pi} \theta \right). \quad (\text{B.2})$$

Assuming P_0 the pitch of an helix composed of N loops in the undeformed configuration (i.e., at $\epsilon = 0$), it is easy to see that at $\epsilon = 0$ the height of the helix is given by

$$H_0 = N P_0, \quad (\text{B.3})$$

while under an applied strain ϵ we have

$$H(\epsilon) = N P = (1 + \epsilon) H_0. \quad (\text{B.4})$$

Note that for the sake of simplicity, we have assumed that the pitch remains constant along the helix, a condition that is violated in the presence of gravity. Substitution of Eq. (B.3) into Eq. (B.4) yields the evolution of the pitch as a function of the applied strain

$$P = (1 + \epsilon) P_0. \quad (\text{B.5})$$

To obtain the diameter of the helix in the deformed configuration (D), we first cal-

culate the length of one loop of the helix both in the deformed configuration

$$L = \int_0^{2\pi} \sqrt{\left(\frac{dx}{d\theta}\right)^2 + \left(\frac{dy}{d\theta}\right)^2 + \left(\frac{dz}{d\theta}\right)^2} d\theta = \sqrt{\pi^2 D^2 + P^2}, \quad (\text{B.6})$$

and in the undeformed configuration

$$L_0 = \sqrt{\pi^2 D_0^2 + P_0^2}. \quad (\text{B.7})$$

Next, we assume that the helix is inextensible (i.e., $L = L_0$), so that

$$\sqrt{\pi^2 D_0^2 + P_0^2} = \sqrt{\pi^2 D^2 + P^2}, \quad (\text{B.8})$$

from which D is obtained as

$$D = D_0 \sqrt{1 - \left(\frac{P_0}{\pi D_0}\right)^2 \epsilon (\epsilon + 2)}. \quad (\text{B.9})$$

In particular, for the helix manufactured for this study (characterized by $P_0 = 13 \text{ mm}$ and $D_0 = 28.6 \text{ mm}$) we have

$$D = 28.6 \sqrt{1 - 0.021 \epsilon (\epsilon + 2)} \text{ mm}. \quad (\text{B.10})$$

Finally, we focus on the metamaterial and consider a square array of helices with center-to-center distance $A_0 = 32.5 \text{ mm}$. It is easy to see that the change in pitch induced by the applied strain significantly alters the solid volume fraction of the system. Since in this study we focus on pressure waves propagating in the air surrounding the helices, in the undeformed configuration each helix can be considered as a

solid cylinder and the solid volume fraction of the metamaterial can be obtained as

$$\psi_0 = \frac{V_{cylinder}}{V_{unit\ cell}} = \frac{\pi D_0^2}{4A_0^2}. \quad (\text{B.11})$$

However, as the applied deformation is increased, the cylinders transform into helices and the air originally inside their internal cavity connects to the surrounding fluid, reducing the solid volume fraction of the metamaterial. Therefore, for $\epsilon > 0$ the solid volume fraction can be calculated as

$$\psi = \frac{V_{helix}}{V_{unit\ cell}} = \frac{V_{helix}}{A_0^2 H_0 (1 + \epsilon)}. \quad (\text{B.12})$$

Since the helices are made of an incompressible material (rubber), their volume is preserved during deformation and can be easily calculated as

$$V_{helix} = \frac{\pi}{4} (D_0^2 - D_{0,in}^2) H_0, \quad (\text{B.13})$$

where $D_{0,in}$ is the inner diameter of the helix in the undeformed configuration (i.e., at $\epsilon = 0$). Thus, the solid volume fraction of the metamaterial under an applied strain ϵ is simply given by

$$\psi = \frac{\pi (D_0^2 - D_{0,in}^2)}{4A_0^2 (1 + \epsilon)}. \quad (\text{B.14})$$

B.4 NUMERICAL SIMULATIONS

All the numerical simulations are carried out using the commercial Finite Element package Abaqus/Standard (SIMULIA, Providence, RI). In particular we conduct two different types of simulations: (i) static analysis to investigate the effect of the ap-

plied deformation on the shape of the helix; *(ii)* Bloch wave analysis to investigate the propagation of small-amplitude acoustic waves in the metamaterial under different levels of deformation.

B.4.1 STATIC ANALYSIS

Static analyses are performed to capture the deformed configuration of the helices under an applied strain ϵ , accounting for the effect of gravity. The FE model of a single helix with the same geometric and material properties as the fabricated one is constructed using quadratic solid elements (Abaqus element type C3D10M with a mesh seed size of 1 *mm*). Moreover, the response of the material is captured using the Yeoh hyperelastic model described in Section C.1. In the simulations we apply a vertical displacement $u = \epsilon H_0$ to the top face of the helix, while constraining the motion of the bottom face. We then monitor the effect of the applied deformation on the pitch and outer diameter. Snapshots of the meshed undeformed and deformed (at $\epsilon = 0.9$) helix are shown in Figure B.3.

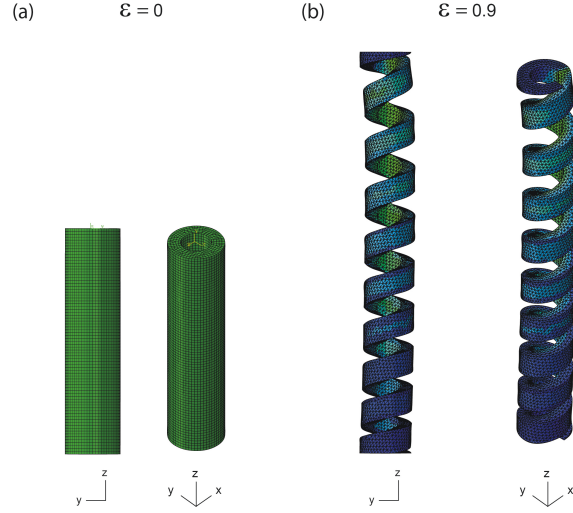


Figure B.3: Numerical images of a single helix. Front and isometric views of (a) the undeformed and (b) highly deformed (i.e., $\epsilon = 0.9$) configuration as obtained from the static analysis.

B.4.2 BLOCH WAVE ANALYSIS

The propagation of sound waves within the acoustic metamaterial is first investigated numerically by considering a square array of helices of infinite extent, characterized by a prismatic unit cell (i.e., minimum unit identified in the periodic structure which includes both the helix and the surrounding air) spanned by the lattice vectors $\mathbf{a}_1 = [A_0, 0, 0]$, $\mathbf{a}_2 = [0, A_0, 0]$, and $\mathbf{a}_3 = [0, 0, P]$, as shown in Figure B.4(b). Thus, any spatial function field, $\phi(\mathbf{x})$, in the infinite periodic structure satisfies the condition:

$$\phi(\mathbf{x} + \mathbf{T}) = \phi(\mathbf{x}), \quad (\text{B.15})$$

where

$$\mathbf{T} = t_1 \mathbf{a}_1 + t_2 \mathbf{a}_2 + t_3 \mathbf{a}_3, \quad (\text{B.16})$$

t_1 , t_2 , and t_3 being arbitrary integers.

The analysis to obtain the dispersion relation of the propagating waves in the periodic structure at different levels of applied deformation consists of two steps: (**Step 1**) we apply statically the desired level of deformation to the unit cell; (**Step 2**) we calculate the dispersion relation of the propagating waves for the deformed unit cell.

Step 1. We mesh the unit cell (comprising only one loop of the helix) using quadratic solid element (Abaqus element type C3D10M) and applied statically the desired level of deformation. To this end, we apply periodic boundary conditions along the axial direction, so that the displacements of each pair of nodes periodically located on the top and bottom faces of the unit cell are related as

$$u_x^t - u_x^b = 0, \quad u_y^t - u_y^b = 0, \quad u_z^t - u_z^b = \epsilon(Z^t - Z^b), \quad (\text{B.17})$$

where the superscripts t and b refer to quantities associated to nodes on the top and bottom surfaces and Z denotes the position in z -direction of a node in the undeformed configuration. Then, a non-linear static step is performed to deform the unit cell by applying the desired value of strain ϵ .

Step 2. We investigate the dynamic response of the metamaterial and conduct frequency domain wave propagation analysis on the deformed the unit cell at different levels of applied deformation, focusing on the propagation of waves in the xy -plane. In particular, we change the elements of the deformed unit cell obtained through Step 1 into acoustic elements (Abaqus element type AC3D10M), and mesh also the surrounding air in the unit cell using the same type of elements (for the air we assume density $\rho_{air} = 1.2 \text{ kg/m}^3$ and speed of sound $c_{L,air} = 343 \text{ m/s}$).

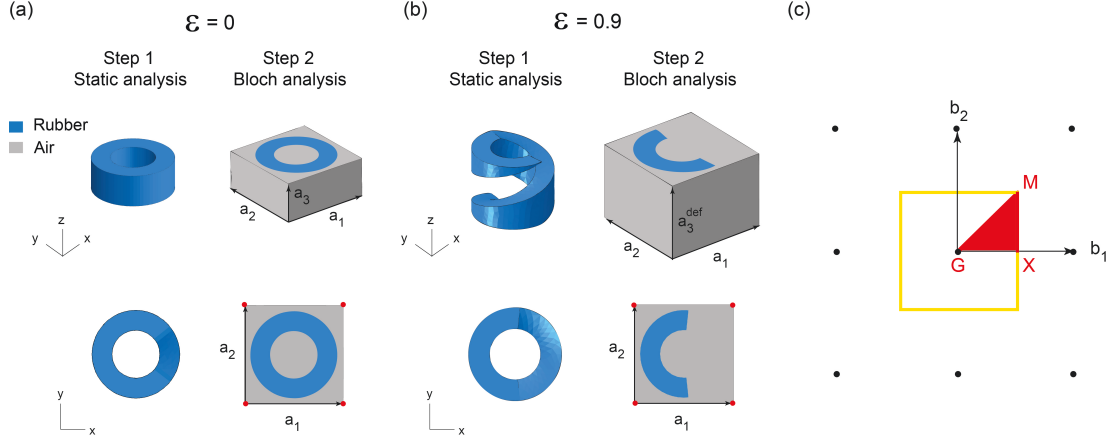


Figure B.4: Bloch wave analysis. (a) Undeformed configuration ($\epsilon = 0$): oblique and top views of the unit cell as obtained from Step 1 (static analysis) and of that used for Step 2 (Bloch analysis); (b) Deformed configuration ($\epsilon = 0.9$): oblique and top views of the unit cell as obtained from Step 1 (static analysis) and of that used for Step 2 (Bloch analysis); (c) corresponding point lattice in reciprocal space showing the *first Brillouin zone* (the area inside the yellow square) and the *irreducible Brillouin zone* (red GXM triangle) for square arrangement of helices. b_1 and b_2 are the reciprocal lattice vectors.

Next, we apply to the faces of the deformed unit cell Bloch-type boundary conditions of the form

$$p(\mathbf{x} + \mathbf{r}) = p(\mathbf{x}) \exp(i\mathbf{k} \cdot \mathbf{r}), \quad (\text{B.18})$$

where p is the acoustic pressure, \mathbf{x} is the position of a node in the deformed configuration and \mathbf{r} denotes the distance in the current configuration between a pair of nodes periodically located on the boundary. Moreover, \mathbf{k} is the Bloch-wave vector lying in the reciprocal space. Since most commercial finite element packages do not support the complex-valued pressure introduced by (B.18), following Aberg and Gudmundson³ we split any complex-valued spatial function $\phi(\mathbf{x})$ into a real and an imaginary part

$$\phi(\mathbf{x}) = \phi(\mathbf{x})^{re} + i\phi(\mathbf{x})^{im}. \quad (\text{B.19})$$

The problem is then solved using two identical finite element meshes for the unit cell, one for the real part and the other for the imaginary part, coupled by

$$\begin{aligned} p^{re}(\mathbf{x} + \mathbf{r}) &= p^{re}(\mathbf{x}) \cos(\mathbf{k} \cdot \mathbf{r}) - p^{im}(\mathbf{x}) \sin(\mathbf{k} \cdot \mathbf{r}), \\ p^{im}(\mathbf{x} + \mathbf{r}) &= p^{re}(\mathbf{x}) \sin(\mathbf{k} \cdot \mathbf{r}) + p^{im}(\mathbf{x}) \cos(\mathbf{k} \cdot \mathbf{r}). \end{aligned} \quad (\text{B.20})$$

Operationally, in our numerical simulations we use a user defined multiple point constraint (MPC) subroutine to implement Eqs. (B.20).

Finally, focusing on the propagation of small-amplitude waves, we solve the frequency-domain acoustic wave equation⁸⁵

$$\nabla \cdot \left(\frac{1}{\rho} \nabla p \right) = -\frac{1}{\rho c_L^2} (\omega(\mathbf{k}))^2 p, \quad (\text{B.21})$$

using a perturbation method to obtain the dispersion relations $\omega = \omega(\mathbf{k})$. Note that, since the reciprocal lattice is also periodic, we can restrict the wave vectors \mathbf{k} to a certain region of the reciprocal space called the *first Brillouin zone*²³ (indicated by the yellow square in Figure B.4(c)). In addition, we may further reduce the domain to the *irreducible Brillouin zone* (IBZ) (red triangle GXM in Figure B.4(c)) by taking advantage of reflectional and rotational symmetries⁸⁵. Operationally, the band gaps are identified by checking all the eigen-frequencies $\omega(\mathbf{k})$ for \mathbf{k} vectors on the perimeter of the IBZ. The band gaps, defined as frequencies range in which the propagation of the waves is forbidden, are obtained by the frequency ranges within no $\omega(\mathbf{k})$ exist. Numerically, a discrete set of \mathbf{k} vectors on the perimeter of the IBZ needs to be chosen for the band gap calculations. For the simulations presented in this paper, twenty uniformly-spaced points on each edge of the IBZ are considered.

Finally, we note that, given the large contrast in material properties between rubber and air, dispersion relations identical to those shown in the paper are obtained also for simplified models in which the elastomeric helix is modeled as a cavity and perfectly-reflecting boundary conditions are assumed at the interface (see Figure B.5).

B.5 ADDITIONAL RESULTS

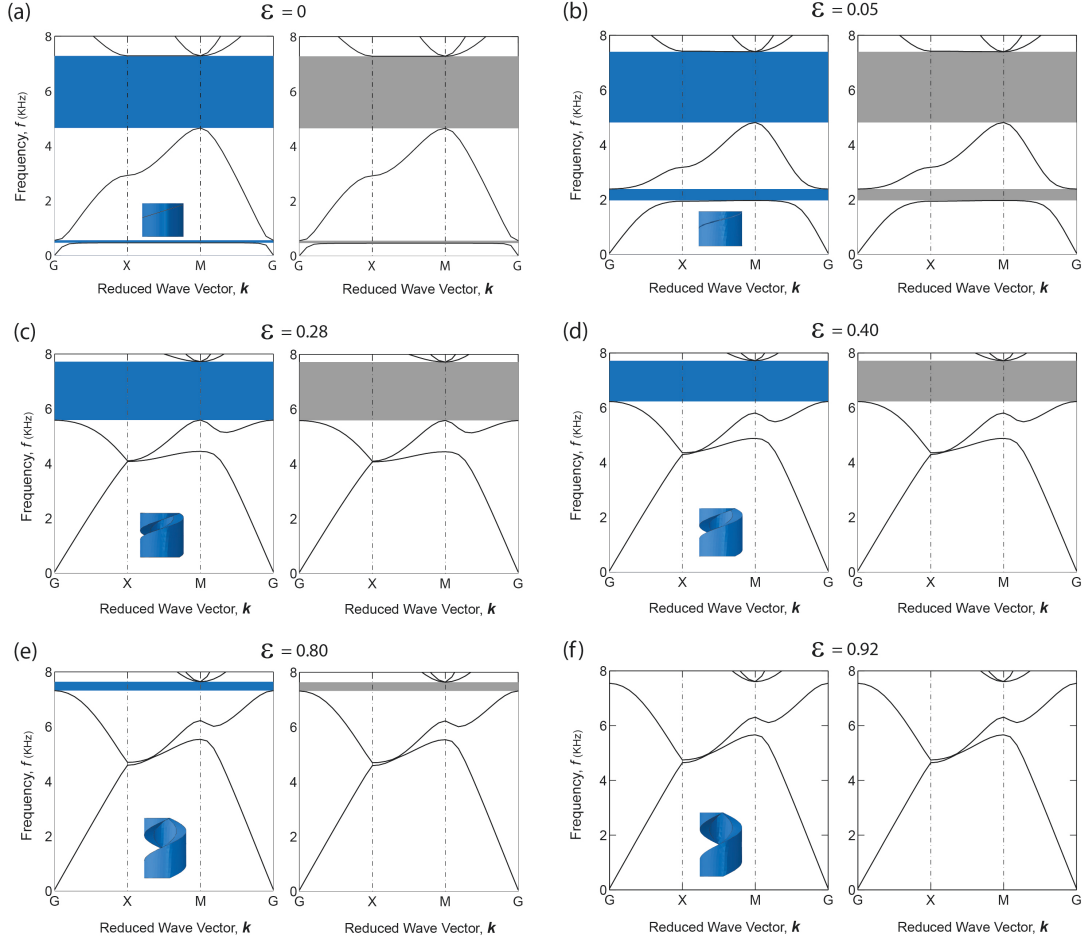


Figure B.5: Effect of the applied deformation on the dispersion relations for the fabricated structure. Dispersion relations calculated at different levels of applied deformation. At each level of deformation the dispersion plots on the left (in blue) are obtained from models that comprise both the elastomeric helix and the surrounding air, while the dispersion plots on the right (in grey) are obtained from simplified models in which the elastomeric helix is modeled as a cavity and perfectly-reflecting boundary conditions are assumed at the interface. The results are reported at different levels of strains (a) $\epsilon = 0$, (b) $\epsilon = 0.05$, (c) $\epsilon = 0.28$, (d) $\epsilon = 0.40$, (e) $\epsilon = 0.80$, and (f) $\epsilon = 0.92$ under uniaxial tension. The insets show the configuration of helices at the corresponding levels of applied strains. The metamaterial comprises a square array of helices with initial outer diameter $D_0 = 28.6 \text{ mm}$, pitch $P_0 = 13 \text{ mm}$, rectangular cross-section of $13 \times 6.5 \text{ mm}$, and lattice spacing $A_0 = 32.5 \text{ mm}$.

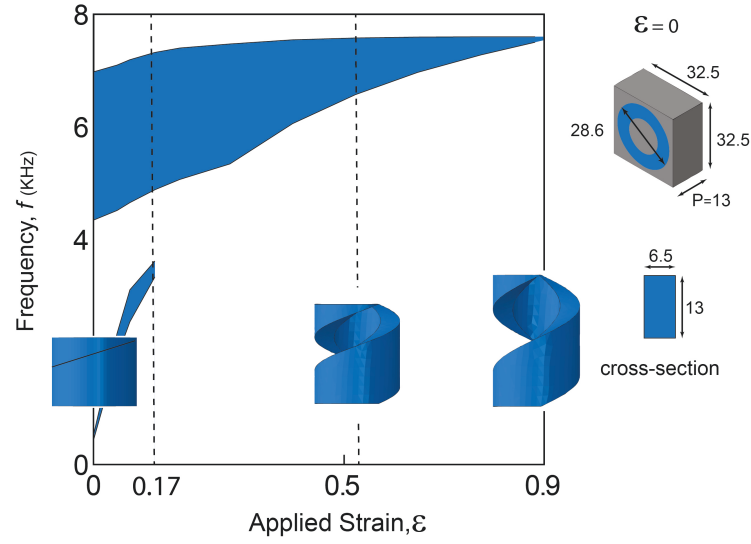


Figure B.6: Evolution of band gap frequency as a function of the applied deformation for the fabricated structure. The metamaterial comprises a square array of helices with initial outer diameter $D_0 = 28.6 \text{ mm}$, pitch $P_0 = 13 \text{ mm}$, rectangular cross-section of $13 \times 6.5 \text{ mm}$, and lattice spacing $A_0 = 32.5 \text{ mm}$.

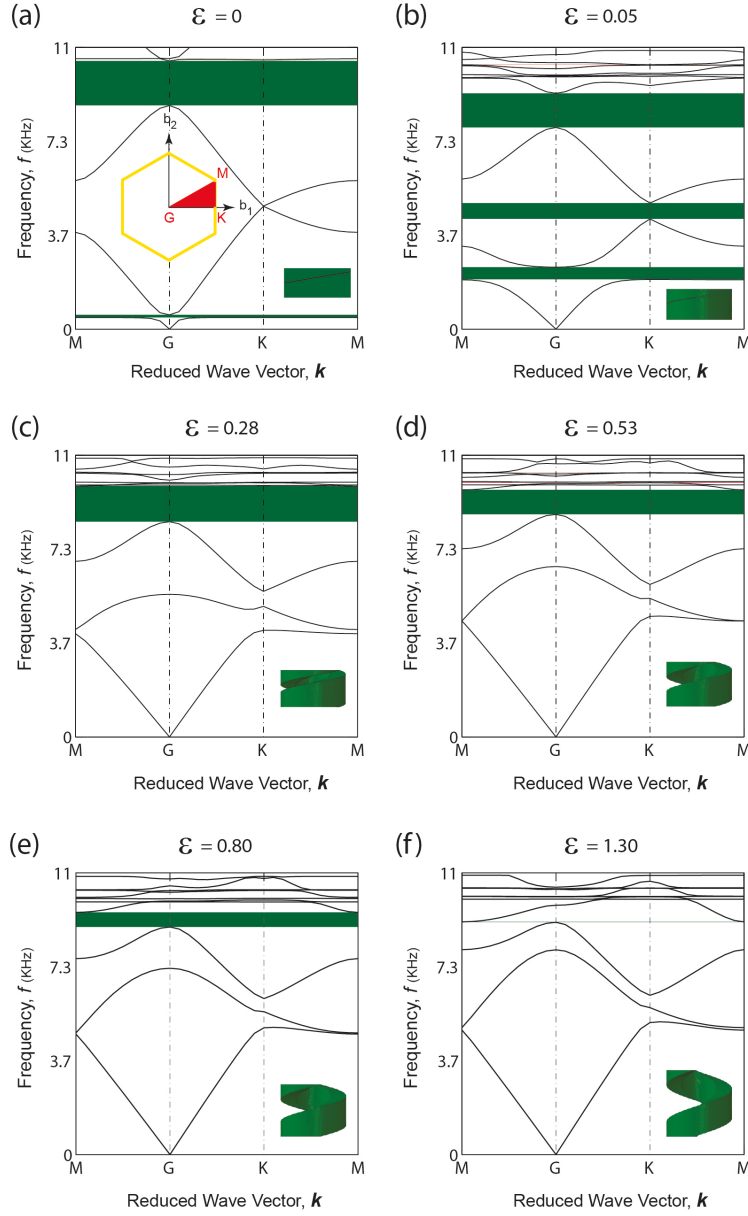


Figure B.7: Effect of the applied deformation on the dispersion relations of a triangular array of helices. Dispersion relations calculated at different levels of applied deformation. The results are reported at different levels of strains (a) $\epsilon = 0$, (b) $\epsilon = 0.05$, (c) $\epsilon = 0.28$, (d) $\epsilon = 0.53$, (e) $\epsilon = 0.80$, and (f) $\epsilon = 1.30$ under uniaxial tension. The insets show the configuration of helices at the corresponding levels of applied strains. The metamaterial comprises a triangular array of helices with initial outer diameter $D_0 = 28.6 \text{ mm}$, pitch $P_0 = 13 \text{ mm}$, rectangular cross-section of $13 \times 6.5 \text{ mm}$, and lattice spacing $A_0 = 32.5 \text{ mm}$.

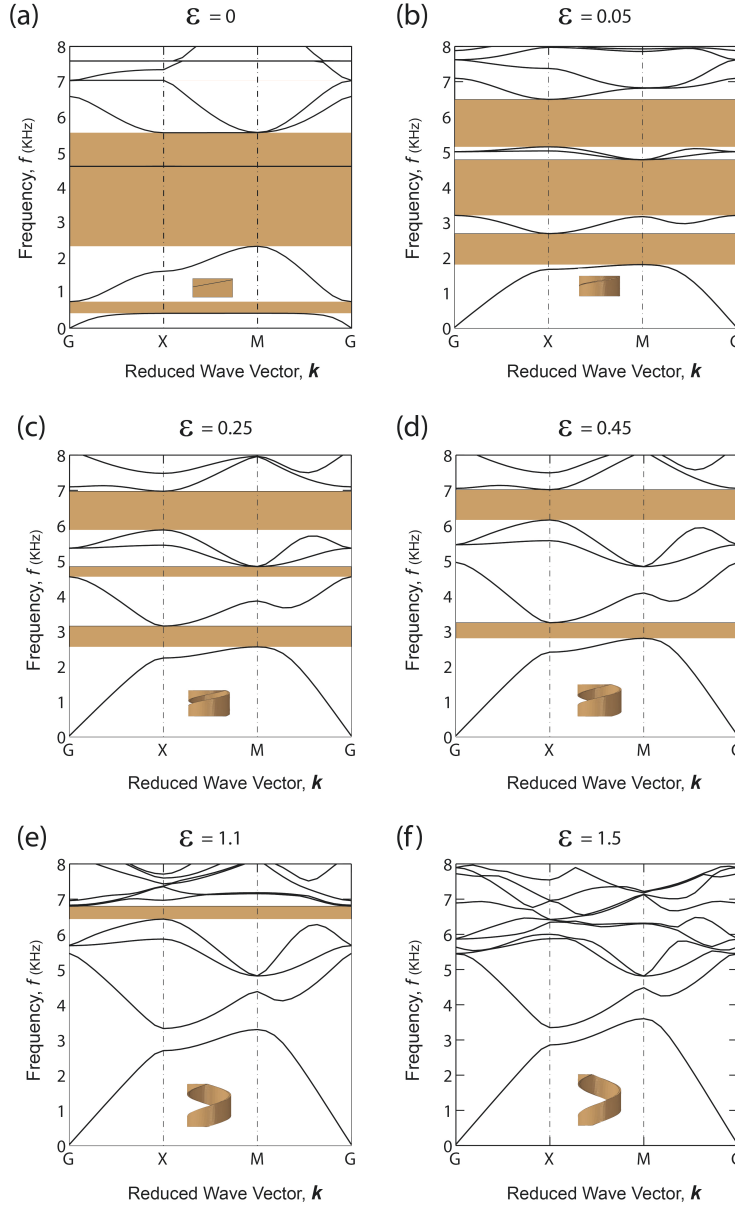


Figure B.8: Effect of the applied deformation on the dispersion relations of a square array of helices. Dispersion relations calculated at different levels of applied deformation. The results are reported at different levels of strains (a) $\epsilon = 0$, (b) $\epsilon = 0.05$, (c) $\epsilon = 0.25$, (d) $\epsilon = 0.45$, (e) $\epsilon = 1.1$, and (f) $\epsilon = 1.5$ under uniaxial tension. The insets show the configuration of helices at the corresponding levels of applied strains. The metamaterial comprises a square array of helices with initial outer diameter $D_0 = 48 \text{ mm}$, pitch $P_0 = 24 \text{ mm}$, rectangular cross-section of $24 \times 2 \text{ mm}$, and lattice spacing $A_0 = 50 \text{ mm}$.



Supporting Information to Chapter 6

C.1 RECONFIGURABLE METAMATERIAL BASED ON EXTRUDED CUBES

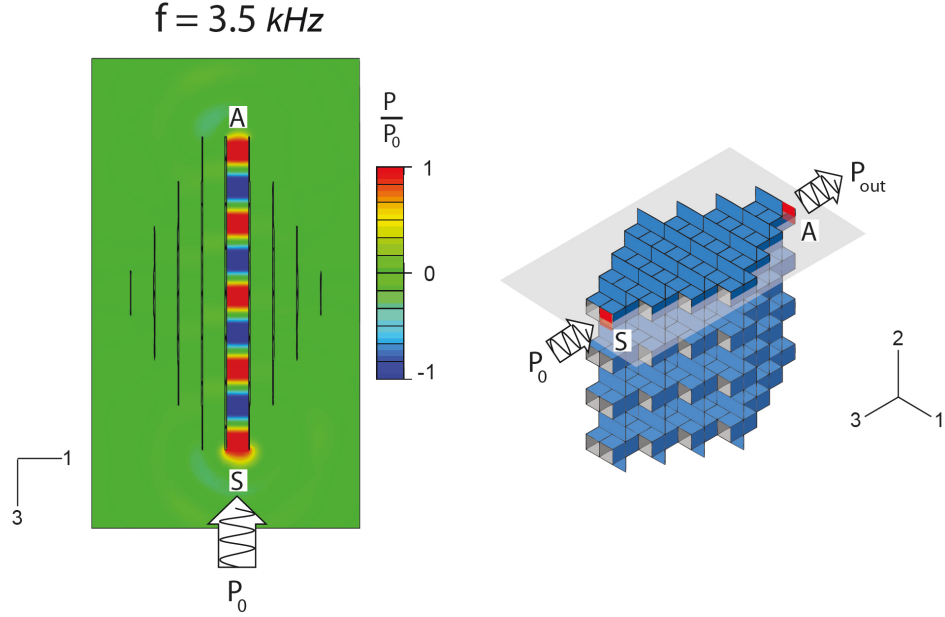


Figure C.1: Propagation of sound waves for $(\alpha_1, \alpha_2, \alpha_3) = (\pi/2, \pi/2, 0)$. Top cross-sectional view of the pressure field distribution at $f = 3.5 \text{ kHz}$. The cutting plane is shown on the right and the color indicates the pressure amplitude normalized by the input signal amplitude (p_0). Differently from Figure 6.3B in the main text, the color bar is chosen to be $-1 < p/p_0 < 1$ so that the plane modes (i.e., high and low pressure zones) are more evident. Note that the weak radiation outside of the structure is not clearly visible for this choice of color bar.

C.2 RECONFIGURABLE METAMATERIAL BASED ON EXTRUDED TRUNCATED OCTAHEDRA

To demonstrate that the proposed strategy to design reconfigurable acoustic waveguides is not restricted to the origami-inspired structure consisting of a cubic array of extruded cube, here we consider a reconfigurable metamaterial based on extruded truncated octahedra. The building block of this metamaterial is an extruded truncated octahedron with a single degree of freedom, denoted by θ in Figure C.2. This building block is constructed by extruding the 8 green hexagonal faces (highlighted in green in Figure C.2) of the truncated octahedra, removing 4 of its square faces (highlighted in yellow in Figure C.2) and making the two remaining ones rigid (highlighted in blue in Figure C.2). This results in a 3D geometry composed of 50 identical rigid faces that can be folded along the 132 edges of length a (see Figure C.2-left). To form the metamaterial, we then connect the building blocks through the extruded edges. As for the case of the metamaterial based on the extruded cubes, by changing θ between 0 and $\pi/2$ the architecture of the system can be transformed to different configurations as shown in Figure C.3.

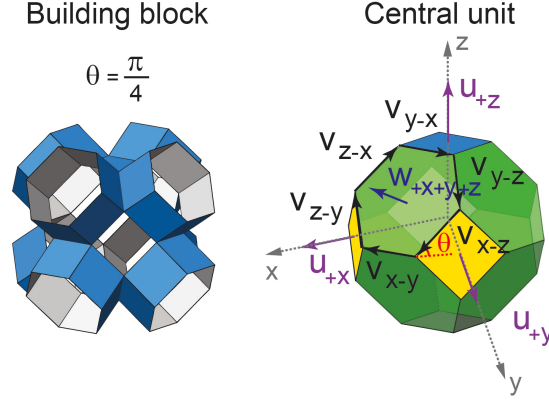


Figure C.2: Building block and central unit of the metamaterial based on extruded truncated octahedra.

To describe all the possible folding shapes of the structure, we need to describe the position of all the faces and edges of the central unit as function of θ . We start by noting that the unit normal vector in outward direction to the 8 hexagonal faces are given by

$$\mathbf{w}_{\pm x \pm y \pm z} = \frac{\langle \pm \sin \theta, \pm \sin \theta, \pm \cos \theta \rangle}{\sqrt{2 \sin^2 \theta + \cos^2 \theta}}, \quad (\text{C.1})$$

while the normals to the six square faces are

$$\begin{aligned} \mathbf{u}_{\pm z} &= \langle 0, 0, \pm 1 \rangle (\sin \theta + \sin \theta), \\ \mathbf{u}_{\pm x} &= \langle \pm 1, 0, 0 \rangle (\cos \theta + \sin \frac{\pi}{4}), \\ \mathbf{u}_{\pm y} &= \langle 0, \pm 1, 0 \rangle (\cos \theta + \sin \frac{\pi}{4}). \end{aligned} \quad (\text{C.2})$$

We also define the 36 edge tangents

$$\begin{aligned}
\mathbf{v}_{\pm y \pm z} &= \langle 0, \pm \cos \theta, \pm \sin \theta \rangle, \\
\mathbf{v}_{\pm z \pm x} &= \langle \pm \cos \theta, 0, \pm \sin \theta \rangle, \\
\mathbf{v}_{\pm x \pm y} &= \langle \pm \sin \pi/4, \pm \sin \pi/4, 0 \rangle,
\end{aligned} \tag{C.3}$$

where $\mathbf{v}_{\pm s \pm t}$ are the edge tangent vectors connecting the faces with normal vector $\mathbf{u}_{\pm s}$ to $\mathbf{u}_{\pm t}$ (with $s = x, y, z$ and $t = x, y, z$). The unit normal vectors \mathbf{w}_{+x+y+z} , \mathbf{u}_{+x} , \mathbf{u}_{+y} , \mathbf{u}_{+z} , and edge vectors \mathbf{v}_{z-x} , \mathbf{v}_{x-z} , \mathbf{v}_{x-y} , \mathbf{v}_{y-x} , \mathbf{v}_{y-z} , \mathbf{v}_{z-y} are shown in Figure C.2-right.

Having known all those vectors, one can fully describe the shape of the structure for given θ . Interestingly, we find that $0 < \theta < \pi/2$ the metamaterial does not act as an acoustic waveguide, since it does not comprise a network of interconnected tubes. Only for $\theta = 0$ and $\theta = \pi/2$ the plates defining the structures form interconnected channels that can be used to guide acoustic waves in one and two directions, respectively.

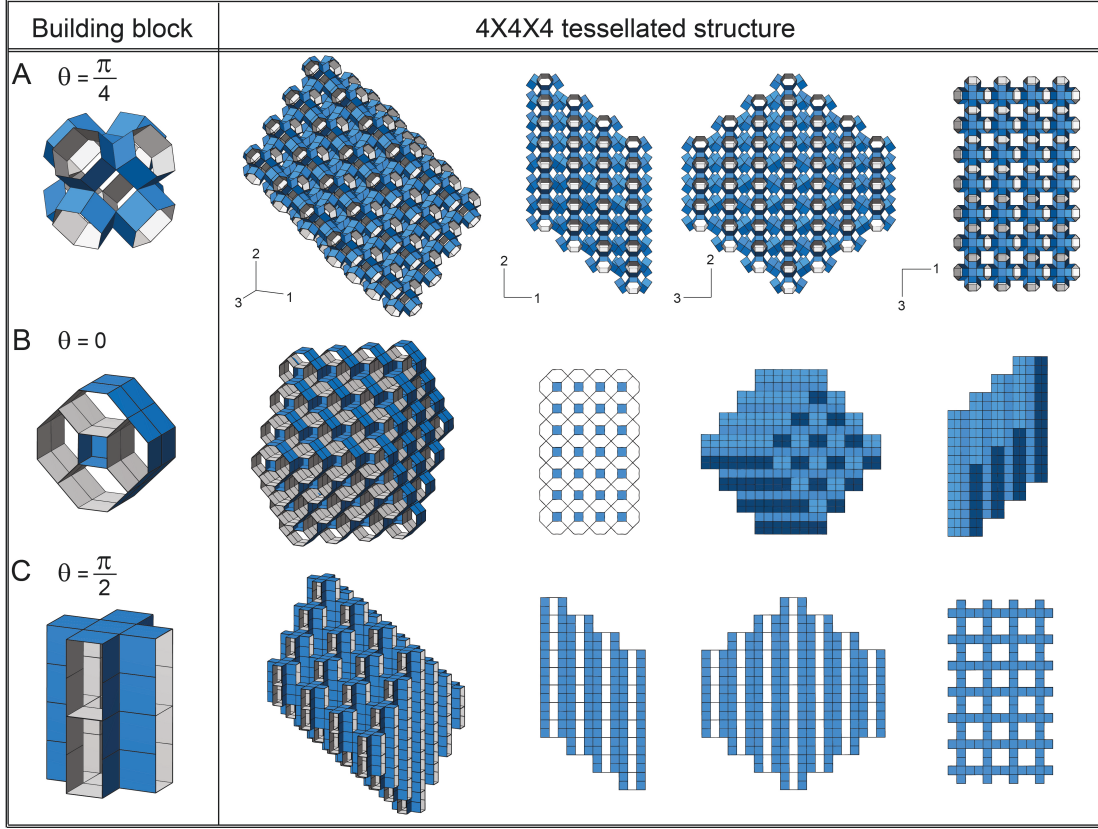


Figure C.3: Reconfigurable metamaterial based on a tessellation of truncated octahedra. Numerical images of the the building block and the corresponding $4 \times 4 \times 4$ reconfigurable acoustic metamaterial deformed into three different configurations: (A) $\theta = \pi/4$; (B) $\theta = 0$; (C) $\theta = \pi/2$.

C.3 RECONFIGURABLE METAMATERIAL BASED ON EXTRUDED HEXAGONAL PRISMS

As part of this study we also investigated the reconfigurability of a metamaterial based on extruded hexagonal prisms. Figure C.4 shows the central unit and corresponding building block of this metamaterial. The building block of this structure is an hexagonal prism with all its faces extruded except for two square faces that are kept rigid (highlighted in blue in Figure C.4). The resulting extruded unit consists of 30 rigid faces that can fold along 74 edges, and can be connected through the extruded edges to form a highly deformable structure characterized by three degrees of freedom, denoted by α , β and γ in Figure C.4. As for the other geometries considered in this study, the structure can be transformed into different shapes by changing α , β and γ . However, it is important to note that only for $\beta = 0$ the plates form a network of tubes. As such, here we consider $\beta = 0$, so that all the possible configurations of the metamaterial are defined by the 4 vectors

$$\begin{aligned}
\mathbf{A} &= \langle -\sqrt{(1 - \sin 2\alpha)/4}, \sqrt{(1 + \sin 2\alpha)/2}, \sqrt{(1 - \sin 2\alpha)/4} \rangle, \\
\mathbf{B} &= \langle 1/\sqrt{2}, 0, 1/\sqrt{2} \rangle, \\
\mathbf{C} &= \langle \sqrt{(1 - \sin 2\gamma)/4}, \sqrt{(1 + \sin 2\gamma)/2}, -\sqrt{(1 - \sin 2\gamma)/4} \rangle, \\
\mathbf{D} &= \langle 0, -1, 0 \rangle.
\end{aligned} \tag{C.4}$$

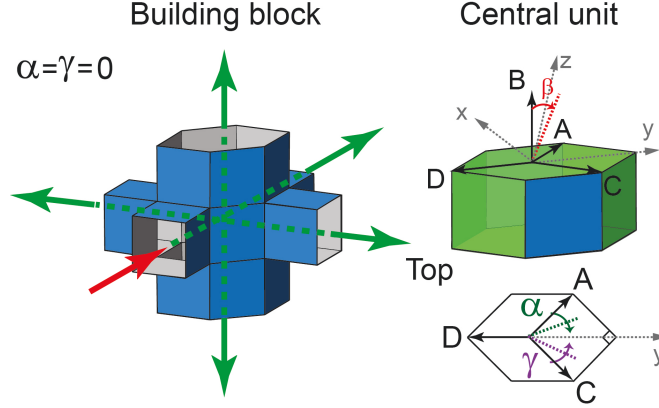


Figure C.4: Building block and central unit of the extruded truncated octahedron metamaterial. The angels α and γ used to describe the shape of the geometry are demonstrated on the right which defined as angular deviation from vectors \mathbf{A} , \mathbf{C} (β is always assumed to be zero). In the buiding block on the left, the red arrows and shaded areas indicate the excited waves, while the green arrows and shaded areas highlight the points from which the structure radiates.

As shown in Figure C.5 A-D, the network of tubes defined by this metamaterial can be transformed into multiple highly distinct shapes by varying α , and γ . For $(\alpha, \gamma) = (0, 0)$ (Figure C.5A) the structure acts as a three-dimensional waveguide as the excited wave can propagate along three different directions. However, through the application of external deformation, the structure can be reconfigured either into another 3D waveguide with mutually perpendicular channels (for $(\alpha, \gamma) = (\pi/4, -\pi/4)$ - see Figure C.5B), or a 2D waveguide (for $(\alpha, \gamma) = (-\pi/4, -\pi/4)$ - see Figure C.5C) or a 1D waveguide (for $(\alpha, \gamma) = (\pi/4, \pi/4)$ - Figure C.5D).

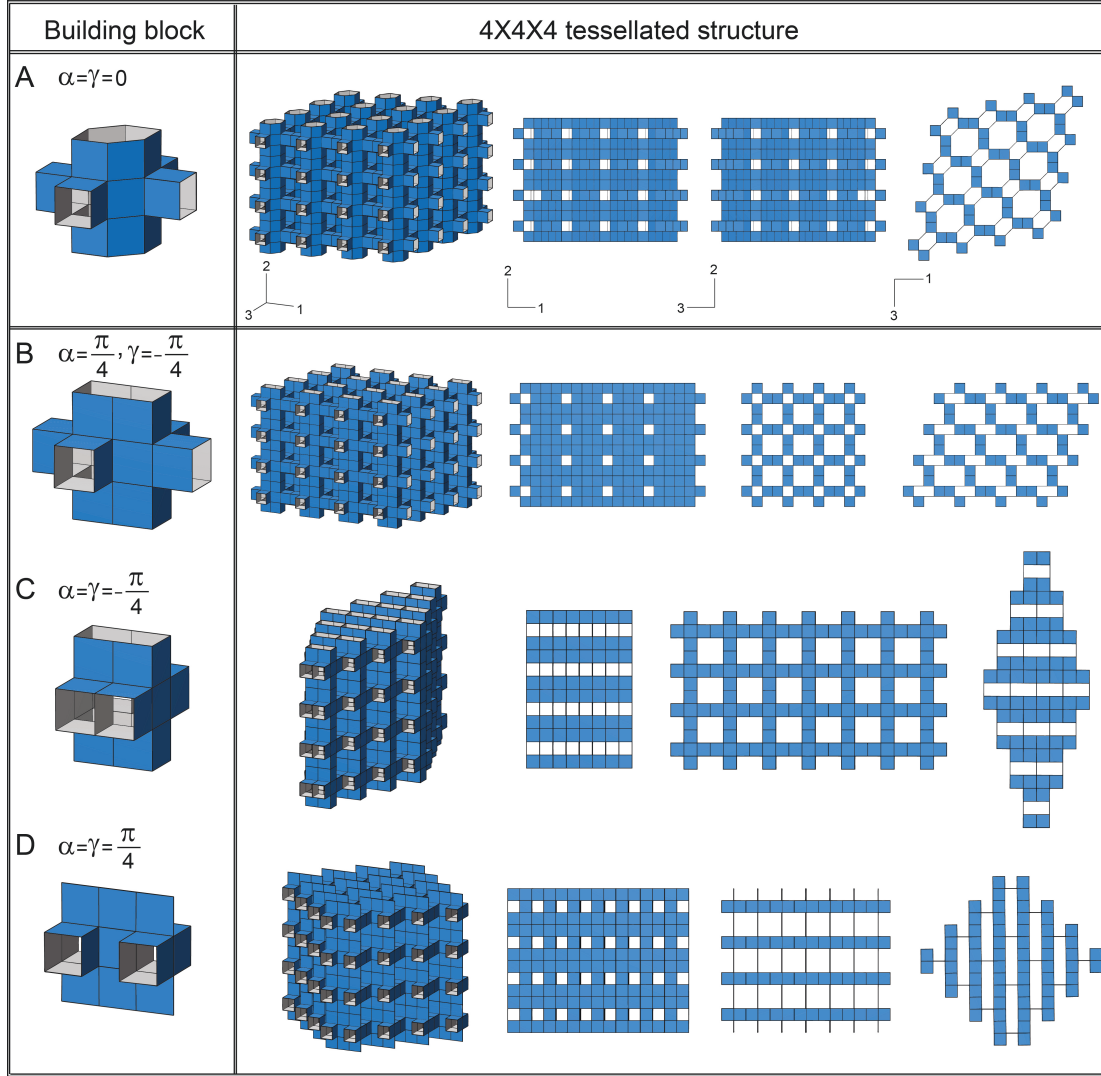


Figure C.5: Reconfigurable metamaterial based on hexagonal prisms. Numerical images of the the building block and the corresponding $4 \times 4 \times 4$ reconfigurable acoustic metamaterial deformed into three different configurations: (A) $(\alpha, \gamma) = (0, 0)$; (B) $(\alpha, \gamma) = (\pi/4, -\pi/4)$; (C) $(\alpha, \gamma) = (-\pi/4, -\pi/4)$; (D) $(\alpha, \gamma) = (\pi/4, \pi/4)$.

Bibliography

- [1] (<https://worksthatwork.com>).
- [2] Abaqus Analysis User's Manual, ver 6.11 (2012). Dassault systemes Simulia Corp., Providence, RI.
- [3] Aberg, M. & Gudmundson, P. (1997). *J. Acoust. Soc. Am.*, 102, 2007.
- [4] Adams, V. & Askenazi, A. (1999). *Building Better Products With Finite Element Analysis*. OnWord Press, Santa Fe, N.M., 1st edition edition.
- [5] Airoidi, L. & Ruzzene, M. (2011). Design of tunable acoustic metamaterials through periodic arrays of resonant shunted piezos. *New Journal of Physics*, 13(11), 113010.
- [6] Attard, D. & Grima, J. N. (2012). A three-dimensional rotating rigid units network exhibiting negative Poisson's ratios. *Physica Status Solidi (B)*, 249(7), 1330–1338.
- [7] Babaei, S., Jahromi, B. H., Ajdari, A., Nayeb-Hashemi, H., & Vaziri, A. (2012). Mechanical properties of open-cell rhombic dodecahedron cellular structures. *Acta Materialia*, 60(67), 2873 – 2885.
- [8] Babaei, S., Overvelde, J. T. B., Chen, E. R., Tournat, V., & Bertoldi, K. (2016a). Reconfigurable origami-inspired acoustic waveguides. *Submitted*.
- [9] Babaei, S., Shahsavari, A. S., Wang, P., Picu, R. C., & Bertoldi, K. (2015a). Wave propagation in cross-linked random fiber networks. *Applied Physics Letters*, 107(21).
- [10] Babaei, S., Shim, J., Weaver, J. C., Chen, E. R., Patel, N., & Bertoldi, K. (2013). 3D soft metamaterials with negative Poisson's ratio. *Advanced Materials*, 25(36), 5044–9.

- [11] Babaei, S., Viard, N., Wang, P., Fang, N. X., & Bertoldi, K. (2016b). Harnessing deformation to switch on and off the propagation of sound. *Advanced Materials*, 28(8), 1631–1635.
- [12] Babaei, S., Wang, P., & Bertoldi, K. (2015b). Three-dimensional adaptive soft phononic crystals. *Journal of Applied Physics*, 117(24), 244903.
- [13] Badreddine Assouar, M., Senesi, M., Oudich, M., Ruzzene, M., & Hou, Z. (2012). Broadband plate-type acoustic metamaterial for low-frequency sound attenuation. *Applied Physics Letters*, 101(17), 173505.
- [14] Baughman, R. H., Shacklette, J. M., Zakhidov, A. A., & Stafstro, S. (1998). Negative Poisson’s ratios as a common feature of cubic metals. *Nature*, 392, 362–365.
- [15] Bergamini, A., Delpero, T., Simoni, L. D., Lillo, L. D., Ruzzene, M., & Ermanni, P. (2014). Phononic crystal with adaptive connectivity. *Advanced Materials*, 26(9), 1343–1347.
- [16] Bertoldi, K., Boyce, M., Deschanel, S., Prange, S., & Mullin, T. (2008a). Mechanics of deformation-triggered pattern transformations and superelastic behavior in periodic elastomeric structures. *Journal of the Mechanics and Physics of Solids*, 56(8), 2642–2668.
- [17] Bertoldi, K., Boyce, M., Deschanel, S., Prange, S., & Mullin, T. (2008b). Mechanics of deformation-triggered pattern transformations and superelastic behavior in periodic elastomeric structures. *Journal of the Mechanics and Physics of Solids*, 56(8), 2642–2668.
- [18] Bertoldi, K., Reis, P. M., Willshaw, S., & Mullin, T. (2010). Negative Poisson’s ratio behavior induced by an elastic instability. *Advanced materials (Deerfield Beach, Fla.)*, 22(3), 361–6.
- [19] Bloch, F. (1929). ber die quantenmechanik der elektronen in kristallgittern. *Zeitschrift fr Physik*, 52(7-8), 555–600.
- [20] Boechler, N., Yang, J., Theocharis, G., Kevrekidis, P. G., & Daraio, C. (2011). Tunable vibrational band gaps in one-dimensional diatomic granular crystals with three-particle unit cells. *Journal of Applied Physics*, 109(7), 074906.

- [21] Bradley C.E. (1994). Time harmonic acoustic bloch wave propagation in periodic waveguides. part i. theory. *J. Acoust. Soc. Am.*, 96(3), 1844–1853.
- [22] Bretagne, A., Venzac, B., Leroy, V., & Tourin, A. (2012). Bragg and hybridization gaps in bubble phononic crystals. *AIP Conference Proceedings*, 1433(1).
- [23] Brillouin, L. (1946). *Wave Propagation in Periodic Structures*. McGraw-Hill.
- [24] Bruneau, M. & Scelo, T. (2006). *Fundamentals of Acoustics*. ISTE, UK and USA.
- [25] Bückmann, T., Stenger, N., Kadic, M., Kaschke, J., Frölich, A., Kennerknecht, T., Eberl, C., Thiel, M., & Wegener, M. (2012). Tailored 3D mechanical metamaterials made by dip-in direct-laser-writing optical lithography. *Advanced materials (Deerfield Beach, Fla.)*, 24(20), 2710–4.
- [26] Casadei, F., Beck, B., Cunefare, K. A., & Ruzzene, M. (2012). Vibration control of plates through hybrid configurations of periodic piezoelectric shunts. *Int. J. Solids Struc.*, 23, 1169.
- [27] Caughey, T. K. & OKelly, M. E. J. (1965). Classical Normal Modes in Damped Linear Dynamic Systems. *Journal of Applied Mechanics*, 32(3), 583–588.
- [28] Chen, B. G.-g., Liu, B., Evans, A. A., Paulose, J., Cohen, I., Vitelli, V., & Santangelo, C. D. (2016). Topological mechanics of origami and kirigami. *Phys. Rev. Lett.*, 116, 135501.
- [29] Climente, A., Torrent, D., & Sánchez-Dehesa, J. (2010). Sound focusing by gradient index sonic lenses. *Applied Physics Letters*, 97(10), 104103.
- [30] Climente, A., Torrent, D., & Sánchez-Dehesa, J. (2012). Omnidirectional broadband acoustic absorber based on metamaterials. *Applied Physics Letters*, 100(14).
- [31] Connolly, F., Polygerinos, P., Walsh, C. J., & Bertoldi, K. (2015). Mechanical programming of soft actuators by varying fiber angle. *Soft Robotics*, 2, 26–32.
- [32] Daraio, C. (2006). *Design of materials Configurations for enhanced phononic and electronic properties*. PhD thesis, UC San Diego.

- [33] Depollier, C., Kergomard, J., & Lesueur J.C. (1990). Propagation of low frequency acoustic waves in periodic 2D-lattices of tubes. *J. of Sound Vib.*, 142(1), 153–170.
- [34] Deymier, P. A., Ed. (2013). *Acoustic Metamaterials and Phononic Crystals*. Springer.
- [35] Eidini, M. & Paulino, G. H. (2015). Unraveling metamaterial properties in zigzag-base folded sheets. *Science Advances*, 1(8).
- [36] Evans, K. E. & Alderson, a. (2000). Auxetic Materials: Functional Materials and Structures from Lateral Thinking. *Advanced Materials*, 12(9), 617–628.
- [37] Ewins, D. J. (2000). *Modal Testing: Theory, Practice and Application*. Research Studies Press Ltd, Baldock, Hertfordshire, UK, 2nd edition edition.
- [38] Fang, N., Xi, D., Xu, J., Ambati, M., Srituravanich, W., Sun, C., & Zhang, X. (2006). Ultrasonic metamaterials with negative modulus. *Nature materials*, 5(6), 452–6.
- [39] Felton, S., Tolley, M., Demaine, E., Rus, D., & Wood, R. (2014). A method for building self-folding machines. *Science*, 345(6197), 644–646.
- [40] Florijn, B., Coulais, C., & van Hecke, M. (2014). Programmable mechanical metamaterials. *Phys. Rev. Lett.*, 113, 175503.
- [41] Gei, M. & Roccabianca, S. (2011). Controlling Bandgap in Electroactive Polymer-Based Structures. *IEEE*, 16(1), 102–107.
- [42] Geryak, R. & Tsukruk, V. V. (2014). Reconfigurable and actuating structures from soft materials. *Soft Matter*, 10, 1246–1263.
- [43] Geymonat, G., Muller, S., & Triantafyllidis, N. (1993). Homogenization of Non-linearly Elastic Materials , Microscopic Bifurcation and Macroscopic Loss of Rank-One Convexity. *Arch. Rational Mech. Anal.*, 122, 231–290.
- [44] Gibson, L. J. & Ashby, M. F. (1999). *Cellular solids: structure and properties*. Cambridge university press.

- [45] Goffaux, C. & Vigneron, J. (2001). Theoretical study of a tunable phononic band gap system. *Physical Review B*, 64(7), 075118.
- [46] Goldman, F. (2011). Using the snapology technique to teach convex polyhedra. *Fifth International Meeting of Origami Science, Mathematics, and Education*, (pp. 99–110).
- [47] Greaves, G. N., Greer, A., Lakes, R., & Rouxel, T. (2011). Poisson’s ratio and modern materials. *Nature materials*, 10(October), 823–838.
- [48] Groby, J., Huang, W., Lardeau, A., & Aurégan, Y. (2015). The use of slow waves to design simple sound absorbing materials. *J. Appl. Phys.*, 117, 124903.
- [49] Hanna, B. H., Lund, J. M., Lang, R. J., Magleby, S. P., & Howell, L. L. (2014). Waterbomb base: a symmetric single-vertex bistable origami mechanism. *Smart Materials and Structures*, 23(9), 094009.
- [50] Huang, Y., Chen, W. Q., Wang, Y. S., & Yang, W. (2015). Multiple refraction switches realized by stretching elastomeric scatterers in sonic crystals. *AIP Advances*, 5(2), 027138.
- [51] Hughes, T., Marmier, a., & Evans, K. (2010). Auxetic frameworks inspired by cubic crystals. *International Journal of Solids and Structures*, 47(11-12), 1469–1476.
- [52] Hussein, M. I. (2009a). Reduced Bloch mode expansion for periodic media band structure calculations. *Proceedings of the Royal Society A: Mathematical, Physical and Engineering Sciences*, 465(2109), 2825–2848.
- [53] Hussein, M. I. (2009b). Theory of damped Bloch waves in elastic media. *Physical Review B*, 80(21), 212301.
- [54] Hussein, M. I. & Frazier, M. J. (2010). Band structure of phononic crystals with general damping. *Journal of Applied Physics*, 108(9), 093506.
- [55] Hussein, M. I., Leamy, M. J., & Ruzzene, M. (2014). Dynamics of Phononic Materials and Structures: Historical Origins, Recent Progress, and Future Outlook. *Applied Mechanics Reviews*, 66(4), 040802.

- [56] Ilievski, F., Mazzeo, A. D., Shepherd, R. F., Chen, X., & Whitesides, G. M. (2011). Soft robotics for chemists. *Angewandte Chemie*, 123(8), 1930–1935.
- [57] Jang, J., Ullal, C. K., Gorishnyy, T., Tsukruk, V. V., & Thomas, E. L. (2006). Mechanically Tunable Three-Dimensional Elastomeric Network / Air Structures via Interference Lithography. *Nano letters*, 6(4), 740–743.
- [58] Kafesaki, M., Sigalas, M., & Economou, E. (1995). Elastic wave band gaps in 3-d periodic polymer matrix composites. *Solid State Communications*, 96(5), 285 – 289.
- [59] Kinra, V. K. & ker, E. L. (1983). An experimental investigation of pass bands and stop bands in two periodic particulate composites. *International Journal of Solids and Structures*, 19(5), 393 – 410.
- [60] Koblar, D. & Boltz, M. (2013). Evaluation of the frequency-dependent young’s modulus and damping factor of rubber from experiment and their implementation in a finite-element analysis. *Experimental Techniques*.
- [61] Kushwaha, M., Halevi, P., Dobrzynski, L., & Djafari-Rouhani, B. (1993). Acoustic Band Structure of Periodic Elastic Composites. *Physical Review Letters*, 71(13), 2022–2025.
- [62] Kushwaha MS, Akjouj, A., Djafari-Rouhani, B., Dobrzynski, L., & Vasseur JO (1998). Acoustic spectral gaps and discrete transmission in slender tubes. *Solid State Comm.*, 106(10), 659–663.
- [63] Kuttruff, H. (2014). *Acoustics : an introduction*. Taylor and Francis.
- [64] Kuzyk, A., Schreiber, R., Zhang, H., Govorov, A. O., Liedl, T., & Liu, N. (2014). Reconfigurable 3d plasmonic metamolecules. *Nat Mater*, 13(9), 1476–1122.
- [65] Lakes, R. (1987). Foam Structures with a Negative Poisson’s Ratio. *Science (New York, N.Y.)*, 235, 1038–1040.
- [66] Lakes, R. (1993). Advances in negative Poisson’s ratio materials. *Advanced Materials*, 5(4), 293–296.

- [67] Lang, R. J. (1989). Origami: Complexity increasing. *engineering and science. Science*, 52(2), 16–23.
- [68] Lee, J. H., Koh, C. Y., Singer, J. P., Jeon, S. J., Maldovan, M., Stein, O., & Thomas, E. L. (2014). 25th anniversary article: Ordered polymer structures for the engineering of photons and phonons. *Advanced Materials*, 26(4), 532–569.
- [69] Lee, J.-H., Singer, J. P., & Thomas, E. L. (2012a). Micro-/nanostructured mechanical metamaterials. *Advanced materials (Deerfield Beach, Fla.)*, 24(36), 4782–810.
- [70] Lee, J.-H., Singer, J. P., & Thomas, E. L. (2012b). Micro-/nanostructured mechanical metamaterials. *Advanced Materials*, 24, 4782.
- [71] Li, X.-F., Ni, X., Feng, L., Lu, M.-H., He, C., & Chen, Y.-F. (2011). Tunable Unidirectional Sound Propagation through a Sonic-Crystal-Based Acoustic Diode. *Physical Review Letters*, 106(8), 084301.
- [72] Liang, B., Guo, X. S., Tu, J., Zhang, D., & Cheng, J. C. (2010). An acoustic rectifier. *Nature materials*, 9(October), 989–992.
- [73] Liang, Z. & Li, J. (2012). *Phys. Rev. Lett.*, 108, 114301.
- [74] Lin, S.-C. S. & Huang, T. J. (2011). Tunable phononic crystals with anisotropic inclusions. *Physical Review B*, 83(17), 174303.
- [75] Liu, Y. & Hu, H. (2010). A review on auxetic structures and polymeric materials. *Scientific Research and Essays*, 5(10), 1052–1063.
- [76] Liu, Z., Chan, C., & Sheng, P. (2002). Three-component elastic wave band-gap material. *Physical Review B*, 65(16), 165116.
- [77] Liu, Z., Zhang, X., Mao, Y., Zhu, Y., Yang, Z., Chan, C., & Sheng, P. (2000). Locally Resonant Sonic Materials. *Science*, 289(5485), 1734–1736.
- [78] Liu, Z. Y., Chan, C. T., & Sheng, P. (2005). *Phys. Rev. B*, 71, 014103.
- [79] Lu, M.-H., Feng, L., & Chen, Y.-F. (2009). Phononic crystals and acoustic metamaterials. *Materials Today*, 12(12), 34–42.

- [80] Lu, M.-H., Zhang, C., Feng, L., Zhao, J., Chen, Y.-F., Mao, Y.-W., Zi, J., Zhu, Y.-Y., Zhu, S.-N., & Ming, N.-B. (2007). Negative birefraction of acoustic waves in a sonic crystal. *Nature materials*, 6(10), 744–8.
- [81] Ma, G., Yang, M., Xiao, S., Yang, Z., & Sheng, P. (2014). Acoustic metasurface with hybrid resonances. *Nature materials*, 13(9), 873–878.
- [82] Maldovan, M. (2013a). Narrow low-frequency spectrum and heat management by thermocrystals. *Phys. Rev. Lett.*, 110, 025902.
- [83] Maldovan, M. (2013b). Sound and heat revolutions in phononics. *Nature*, 503(7475), 209–17.
- [84] Maldovan, M. & Thomas, E. (2009a). *Periodic Materials and Interference Lithography for Photonics, Phononics and Mechanics*. Wiley-VCH.
- [85] Maldovan, M. & Thomas, E. L. (2009b). *Periodic Materials and Interference Lithography: for Photonics, Phononics and Mechanics*. Wiley-VCH Verlag GmbH & Co. KGaA.
- [86] Mao, X., Lin, S.-C. S., Lapsley, M. I., Shi, J., Juluri, B. K., & Huang, T. J. (2009). Tunable Liquid Gradient Refractive Index (L-GRIN) lens with two degrees of freedom. *Lab on a chip*, 9(14), 2050–8.
- [87] Martinez, R. V., Branch, J. L., Fish, C. R., Jin, L., Shepherd, R. F., Nunes, R. M. D., Suo, Z., & Whitesides, G. M. (2013). Robotic tentacles with three-dimensional mobility based on flexible elastomers. *Advanced Materials*, 25(2), 205–212.
- [88] Martinez, R. V., Fish, C. R., Chen, X., & Whitesides, G. M. (2012). Elastomeric origami: Programmable paper-elastomer composites as pneumatic actuators. *Advanced Functional Materials*, 22(7), 1376–1384.
- [89] Martínez-Sala, R., Sancho, J., Sánchez, J. V., Gómez, V., & Llinares, J. (1995). Sound attenuation by sculpture. *Nature*, 378, 241.
- [90] Matar, O. B., Vasseur, J., & Deymier, P. A. (2013). *Acoustic Metamaterials and Phononic Crystals*, volume 173 of *Springer Series in Solid-State Sciences*. Berlin, Heidelberg: Springer Berlin Heidelberg.

- [91] Mei, J., Ma, G., Yang, M., Yang, Z., Wen, W., & Sheng, P. (2012). Dark acoustic metamaterials as super absorbers for low-frequency sound. *Nature Communications*, 3, 756.
- [92] Molerón, M., Félix, S., Pagneux, V., & Richoux, O. (2012). Sound propagation in periodic urban areas. *J. Appl. Phys.*, 111, 114906.
- [93] Morse, P. M. & Ingard, K. U. (1987). *Theoretical acoustics*. New York, McGraw-Hill.
- [94] Mott, M. & Evans, J. (1999). Zirconia/alumina functionally graded material made by ceramic ink jet printing. *Materials Science and Engineering: A*, 271(12), 344 – 352.
- [95] Mousanezhad, D., Babaei, S., Ebrahimi, H., Ghosh, R., Hamouda, A. S., Bertoldi, K., & Vaziri, A. (2015a). Hierarchical honeycomb auxetic metamaterials. *Scientific Reports*, (pp. 2045–2322).
- [96] Mousanezhad, D., Babaei, S., Ghosh, R., Mahdi, E., Bertoldi, K., & Vaziri, A. (2015b). Honeycomb phononic crystals with self-similar hierarchy. *Phys. Rev. B*, 92, 104304.
- [97] Munday J.N., Brad Bennett, C., & Robertson W.M. (2002). Band gaps and defect modes in periodically structured waveguides. *J. Acoust. Soc. Am.*, 112(4), 1353–1358.
- [98] Ogden, R. W. (1997). *Non-Linear Elastic Deformations*. Dover.
- [99] Overvelde, J. T., de Jong, T. A., Shevchenko, Y., Becerra, S. A., Whitesides, G. M., Weaver, J. C., Hoberman, C., & Bertoldi, K. (2016a). A three-dimensional actuated origami-inspired transformable metamaterial with multiple degrees of freedom. *Nat Commun*, (7), 10929.
- [100] Overvelde, J. T., Weaver, J. C., Hoberman, C., & Bertoldi, K. (2016b). *Submitted for publication*.
- [101] Overvelde, J. T. B., Kloek, T., Dhaen, J. J. A., & Bertoldi, K. (2015). Amplifying the response of soft actuators by harnessing snap-through instabilities. *Proceedings of the National Academy of Sciences*, 112(35), 10863–10868.

- [102] Overvelde JTB, Shan S, B. K. (2012). Compaction through buckling in 2d periodic, soft and porous structures: Effect of pore shape. *Advanced Materials*, 24, 2337.
- [103] Page, J., Yang, S., Cowan, M., Liu, Z., Chan, C., & Sheng, P. (2003). 3d phononic crystals. In B. van Tiggelen & S. Skipetrov (Eds.), *Wave Scattering in Complex Media: From Theory to Applications*, volume 107 of *NATO Science Series* (pp. 282–307). Springer Netherlands.
- [104] Pendry, J., a.J. Holden, Robbins, D., & Stewart, W. (1999). Magnetism from conductors and enhanced nonlinear phenomena. *IEEE Transactions on Microwave Theory and Techniques*, 47(11), 2075–2084.
- [105] Pikhitsa, P. V., Choi, M., Kim, H.-J., & Ahn, S.-H. (2009). Auxetic lattice of multipods. *Physica Status Solidi (B)*, 246(9), 2098–2101.
- [106] Poirier, B., Maury, C., & Ville J.-M. (2011). The use of Herschel-Quincke tubes to improve the efficiency of lined ducts. *Applied Acoustics*, 72(2-3), 78–88.
- [107] Polygerinos, P., Wang, Z., Overvelde, J. T. B., Galloway, K. C., Wood, R. J., Bertoldi, K., & Walsh, C. J. (2015). Modeling of soft fiber-reinforced bending actuators. *IEEE Transactions on Robotics*, 31(3), 778 – 789.
- [108] Psarobas, I., Modinos, A., Sainidou, R., & Stefanou, N. (2002). Acoustic properties of colloidal crystals. *Phys. Rev. B*, 65, 064307.
- [109] Rafsanjani, A., Akbarzadeh, A., & Pasini, D. (2015). Snapping mechanical metamaterials under tension. *Advanced Materials*, 27(39), 5931–5935.
- [110] Raney, J. R. & Lewis, J. A. (2015). Printing mesoscale architectures. *MRS Bulletin*, 40, 943–950.
- [111] Rayleigh, J. W. (1894). *The Theory of Sound, Volume 1*. London: Macmillan and co. and New York, 2nd editio edition.
- [112] Richoux, O., Tournat, V., & Le Van Suu, T. (2007). Acoustic wave dispersion in a one-dimensional lattice of nonlinear resonant scatterers. *Phys. Rev. E*, 75, 026615.

- [113] Romero-García, V., Lagarrigue, C., Groby, J.-P., Richoux, O., & Tournat, V. (2013). Tunable acoustic waveguides in periodic arrays made of rigid square-rod scatterers: theory and experimental realization. *Journal of Physics D: Applied Physics*, 46(30), 305108.
- [114] Rudykh, S. & Boyce, M. C. (2014). Transforming Wave Propagation in Layered Media via Instability-Induced Interfacial Wrinkling. *Physical Review Letters*, 112(3), 034301.
- [115] Sachs, E., Cima, M., Williams, P., Brancazio, D., & Cornie, J. (1992). Three dimensional printing: Rapid tooling and prototypes directly from a cad model. *Journal of Engineering for Industry*, 114(4), 481–488.
- [116] Sainidou, R., Djafari-Rouhani, B., Pennec, Y., & Vasseur, J. O. (2006). Locally resonant phononic crystals made of hollow spheres or cylinders. *Phys. Rev. B*, 73, 024302.
- [117] Sánchez-Dehesa, J., Garcia-Chocano, V. M., Torrent, D., Cervera, F., Cabrera, S., & Simon, F. (2011). Noise control by sonic crystal barriers made of recycled materials. *The Journal of the Acoustical Society of America*, 129(3), 1173–1183.
- [118] Sánchez-Pérez, J. V., Caballero, D., Sánchez-Dehesa, J., Martínez-Sala, R., Rubio, C., Meseguer, F., Llinares, J., & Gálvez, F. (1998). Sound Attenuation by a Two-Dimensional Array of Rigid Cylinders. *Physical Review Letters*, 80, 5325–5328.
- [119] Sanchis, L., García-Chocano, V. M., Llopis-Pontiveros, R., Climente, a., Martínez-Pastor, J., Cervera, F., & Sánchez-Dehesa, J. (2013). Three-Dimensional Axisymmetric Cloak Based on the Cancellation of Acoustic Scattering from a Sphere. *Physical Review Letters*, 110(12), 124301.
- [120] Schaedler, T., Jacobsen, A., Torrents, A., Sorensen, A., Lian, J., Greer, J., Valdevit, L., & Carter, W. (2011a). Ultralight Metallic Microlattices. *Science*, 334, 962–965.
- [121] Schaedler, T. A., Jacobsen, A. J., Torrents, A., Sorensen, A. E., Lian, J., Greer, J. R., Valdevit, L., & Carter, W. B. (2011b). Ultralight metallic microlattices. *Science*, 334(6058), 962–965.

- [122] Seerden, K. A. M., Reis, N., Evans, J. R. G., Grant, P. S., Halloran, J. W., & Derby, B. (2001). Ink-jet printing of wax-based alumina suspensions. *Journal of the American Ceramic Society*, 84(11), 2514–2520.
- [123] Selamet, A., Dickey NS, & Novak JM (1994). The Herschel-Quincke tube: a theoretical, computational, and experimental investigation. *J. Acoust. Soc. Am.*, 96(5), 3177–3185.
- [124] Shan, S., Kang, S. H., Raney, J. R., Wang, P., Fang, L., Candido, F., Lewis, J. A., & Bertoldi, K. (2015a). Multistable architected materials for trapping elastic strain energy. *Advanced Materials*, 27(29), 4296–4301.
- [125] Shan, S., Kang, S. H., Raney, J. R., Wang, P., Fang, L., Candido, F., Lewis, J. A., & Bertoldi, K. (2015b). Multistable architected materials for trapping elastic strain energy. *Advanced Materials*, 27(29), 4296–4301.
- [126] Shan, S., Kang, S. H., Wang, P., Qu, C., Shian, S., Chen, E. R., & Bertoldi, K. (2014a). Harnessing multiple folding mechanisms in soft periodic structures for tunable control of elastic waves. *Advanced Functional Materials*, 24(31), 4935.
- [127] Shan, S., Kang, S. H., Wang, P., Qu, C., Shian, S., Chen, E. R., & Bertoldi, K. (2014b). Harnessing multiple folding mechanisms in soft periodic structures for tunable control of elastic waves. *Advanced Functional Materials*, 24(31), 4935–4942.
- [128] Shi, J., Ahmed, D., Mao, X., Lin, S.-C. S., Lawit, A., & Huang, T. J. (2009). Acoustic tweezers: patterning cells and microparticles using standing surface acoustic waves (SSAW). *Lab on a chip*, 9(20), 2890–5.
- [129] Shim, J., Perdigou, C., Chen, E. R., Bertoldi, K., & Reis, P. M. (2012). Buckling-induced encapsulation of structured elastic shells under pressure. *Proceedings of the National Academy of Sciences of the United States of America*, 109(16), 5978–83.
- [130] Shim, J., Shan, S., Košmrlj, A., Kang, S. H., Chen, E. R., Weaver, J. C., & Bertoldi, K. (2013). Harnessing instabilities for design of soft reconfigurable auxetic/chiral materials. *Soft Matter*, 9(34), 8198–8202.

- [131] Sidorenko, A., Krupenkin, T., Taylor, A., Fratzl, P., & Aizenberg, J. (2007). Reversible Switching of. *Science (New York, N.Y.)*, 315(January), 487–490.
- [132] Sigalas, M. & Economou, E. N. (1993). Band structure of elastic waves in two dimensional systems. *Solid State Communications*, 86(3), 141–143.
- [133] Silverberg, J. L., Evans, A. A., McLeod, L., Hayward, R. C., Hull, T., Santangelo, C. D., & Cohen, I. (2014). Using origami design principles to fold reprogrammable mechanical metamaterials. *Science*, 345(6197), 647–650.
- [134] Silverberg, J. L., Na, J.-H., Evans, A. A., Liu, B., Hull, T. C., Santangelo, C., Lang, R. J., Hayward, R. C., & Cohen, I. (2015). Origami structures with a critical transition to bistability arising from hidden degrees of freedom. *Nat Mater*, 14, 389–393.
- [135] Song, J. H., Edirisinghe, M. J., & Evans, J. R. G. (1999). Formulation and multilayer jet printing of ceramic inks. *Journal of the American Ceramic Society*, 82(12), 3374–3380.
- [136] Soukoulis, C. M. & Wegener, M. (2011). Past achievements and future challenges in the development of three-dimensional photonic metamaterials. *Nature Photonics*, 5(SEPTEMBER).
- [137] Still, T., Cheng, W., Retsch, M., Sainidou, R., Wang, J., Jonas, U., Stefanou, N., & Fytas, G. (2008). Simultaneous occurrence of structure-directed and particle-resonance-induced phononic gaps in colloidal films. *Phys. Rev. Lett.*, 100, 194301.
- [138] Strobl, H. (2010). *Special Snapology, A simple and cheap method to make convex polyhedra models*.
- [139] Sugimoto, N., Masuda, M., Ohno, J., & Motoi, D. (1999). Experimental demonstration of generation and propagation of acoustic solitary waves in an air-filled tube. *Phys. Rev. Lett.*, 83(20), 4053–4057.
- [140] Sui, N., Yan, X., Huang, T.-Y., Xu, J., Yuan, F.-G., & Jing, Y. (2015). A lightweight yet sound-proof honeycomb acoustic metamaterial. *Applied Physics Letters*, 106(17), 171905.

- [141] Theocharis, G., Richoux, O., Romero-García, V., Merkel, A., & Tournat, V. (2014). Limits of slow sound propagation and transparency in lossy, locally resonant periodic structures. *New J. Phys.*, 16, 093017.
- [142] Thomason, W. & Dahleh, M. (1998). *Theory of Vibration With Applications*. prentice Hall, 5th edition edition.
- [143] Treloar, L. (1944). Stress-strain data for vulcanized rubber under various types of deformation. *Trans. Faraday Soc.*, 40, 59.
- [144] Triantafyllidis, N., Nestorovic, M. D., & Schraad, M. W. (2006). Failure surfaces for finitely strained two-phase periodic solids under general in-plane loading. *Journal of Applied Mechanics*, 73(3), 505.
- [145] Waitukaitis, S., Menaut, R., Chen, B. G.-g., & van Hecke, M. (2015). Origami multistability: From single vertices to metasheets. *Phys. Rev. Lett.*, 114, 055503.
- [146] Walker, E., Reyes, D., Rojas, M. M., Krokhin, A., Wang, Z., & Neogi, A. (2014). Tunable ultrasonic phononic crystal controlled by infrared radiation. *Applied Physics Letters*, 105(14), 143503.
- [147] Wang, L. & Bertoldi, K. (2012). Mechanically tunable phononic band gaps in three-dimensional periodic elastomeric structures. *International Journal of Solids and Structures*, 49(19-20), 2881–2885.
- [148] Wang, P., Casadei, F., Shan, S., Weaver, J. C., & Bertoldi, K. (2014). Harnessing buckling to design tunable locally resonant acoustic metamaterials. *Phys. Rev. Lett.*, 113, 014301.
- [149] Wang, P., Shim, J., & Bertoldi, K. (2013). Effects of geometric and material nonlinearities on tunable band gaps and low-frequency directionality of phononic crystals. *Physical Review B*, 88(1), 014304.
- [150] Wang, Y., Li, F., Wang, Y., Kishimoto, K., & Huang, W. (2009). Tuning of band gaps for a two-dimensional piezoelectric phononic crystal with a rectangular lattice. *Acta Mechanica Sinica/Lixue Xuebao*, 25(1), 65–71.
- [151] Wei, Z. Y., Guo, Z. V., Dudte, L., Liang, H. Y., & Mahadevan, L. (2013). Geometric mechanics of periodic pleated origami. *Phys. Rev. Lett.*, 110, 215501.

- [152] Wu, F., Liu, Z., & Liu, Y. (2002). Acoustic band gaps created by rotating square rods in a two-dimensional lattice. *Physical Review E*, 66(4), 046628.
- [153] Xu, S., Yan, Z., Jang, K.-I., Huang, W., Fu, H., Kim, J., Wei, Z., Flavin, M., McCracken, J., Wang, R., Badea, A., Liu, Y., Xiao, D., Zhou, G., Lee, J., Chung, H. U., Cheng, H., Ren, W., Banks, A., Li, X., Paik, U., Nuzzo, R. G., Huang, Y., Zhang, Y., & Rogers, J. A. (2015). Assembly of micro/nanomaterials into complex, three-dimensional architectures by compressive buckling. *Science*, 347(6218), 154–159.
- [154] Yan, Z., Zhang, F., Wang, J., Liu, F., Guo, X., Nan, K., Lin, Q., Gao, M., Xiao, D., Shi, Y., Qiu, Y., Luan, H., Kim, J. H., Wang, Y., Luo, H., Han, M., Huang, Y., Zhang, Y., & Rogers, J. A. (2016). Controlled mechanical buckling for origami-inspired construction of 3d microstructures in advanced materials. *Advanced Functional Materials*, 26(16), 2629–2639.
- [155] Yang, D., Jin, L., Martinez, R. V., Bertoldi, K., Whitesides, G. M., & Suo, Z. (2016). Phase-transforming and switchable metamaterials. *Extreme Mechanics Letters*, 6, 1–9.
- [156] Yang, D., Mosadegh, B., Ainla, A., Lee, B., Khashai, F., Suo, Z., Bertoldi, K., & Whitesides, G. M. (2015). Buckling of elastomeric beams enables actuation of soft machines. *Advanced Materials*, 27(41), 6323–6327.
- [157] Yang, S., Page, J., Liu, Z., Cowan, M., Chan, C., & Sheng, P. (2004). Focusing of Sound in a 3D Phononic Crystal. *Physical Review Letters*, 93(2), 024301.
- [158] Yang, Z., Dai, H. M., Chan, N. H., Ma, G. C., & Sheng, P. (2010). Acoustic metamaterial panels for sound attenuation in the 50-1000 hz regime. *Applied Physics Letters*, 96(4), 041906.
- [159] Yasuda, H., Chen, Z., & Yang, J. (2016). Multitransformable leaf-out origami with bistable behavior. *Journal of Mechanisms and Robotics*, 8(3), 031013.
- [160] Yasuda, H. & Yang, J. (2015). Reentrant origami-based metamaterials with negative poisson’s ratio and bistability. *Phys. Rev. Lett.*, 114, 185502.
- [161] Yeoh, O. (1993). Some forms of the strain energy function for rubber. *Rubber Chem. Technol.*, 66, 754–771.

- [162] Zárate, Y., Babaei, S., Kang, S. H., Neshev, D. N., Shadrivov, I. V., Bertoldi, K., & Powell, D. A. (2016). Elastic metamaterials for tuning circular polarization of electromagnetic waves. *Scientific Reports*, 6, 28273.
- [163] Zhang, X., Liu, Z., Liu, Y., & Wu, F. (2003). Elastic wave band gaps for three-dimensional phononic crystals with two structural units. *Physics Letters A*, 313(56), 455 – 460.
- [164] Zheng, X., Lee, H., Weisgraber, T. H., Shusteff, M., DeOtte, J., Duoss, E. B., Kuntz, J. D., Biener, M. M., Ge, Q., Jackson, J. A., Kucheyev, S. O., Fang, N. X., & Spadaccini, C. M. (2014). Ultralight, ultrastiff mechanical metamaterials. *Science*, 344, 1373–1377.
- [165] Zigoneanu, L., Popa, B.-i., & Cummer, S. A. (2014). Three-dimensional broadband omnidirectional acoustic ground cloak. *Nature materials*, 13(April), 1–4.

HIS THESIS WAS TYPESET using
L^AT_EX, originally developed by Leslie
Lamport and based on Donald Knuth's
T_EX. The body text is set in 11 point
Egenolff-Berner Garamond, a revival of
Claude Garamont's humanist typeface.
The above illustration, *Science Exper-*
iment 02, was created by Ben Schlitter
and released under CC BY-NC-ND 3.0. A
template that can be used to format a
PhD dissertation with this look & feel
has been released under the permissive
AGPL license, and can be found online at
github.com/asm-products/Dissertate or
from its lead author, Jordan Suchow, at
suchow@post.harvard.edu.